Achieving highest proton intensities with a laser-based ion beamline

Der Weg zu höchsten Protonenintensitäten mit einer laserbasierten Ionenstrahlführung
Zur Erlangung des Grades eines Doktors der Naturwissenschaften (Dr. rer. nat.)
genehmigte Dissertation von Diana Jahn aus Hanau am Main
Tag der Einreichung: 8. April 2019, Tag der Prüfung: 17. Juni 2019
Darmstadt — D 17

1. Gutachten: Prof. Dr. Markus Roth
2. Gutachten: Prof. Dr. Oliver Boine-Frankenheim

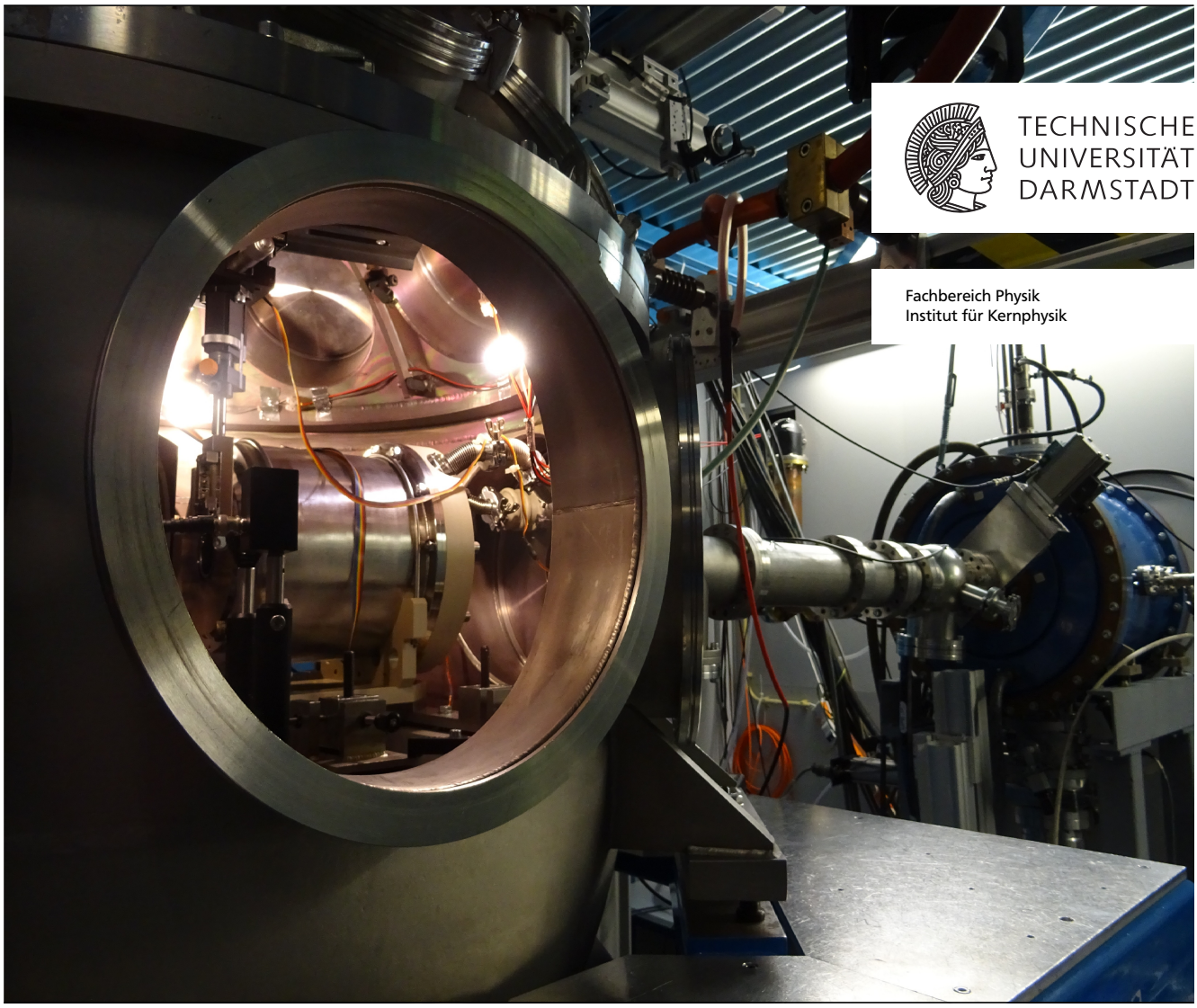

TECHNISCHE UNIVERSITÄT DARMSTADT

Fachbereich Physik
Institut für Kernphysik

Achieving highest proton intensities with a laser-based ion beamline
Der Weg zu höchsten Protonenintensitäten mit einer laserbasierten Ionenstrahlführung

Genehmigte Dissertation von Diana Jahn aus Hanau am Main

1. Gutachten: Prof. Dr. Markus Roth
2. Gutachten: Prof. Dr. Oliver Boine-Frankenheim

Tag der Einreichung: 8. April 2019
Tag der Prüfung: 17. Juni 2019

Darmstadt — D 17

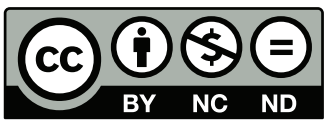

Abstract

The discovery of intense, laser-generated ion beams established a new research field. Laser-driven proton beams deliver a broad, exponentially decaying energy spectrum up to nearly one hundred MeV. Compared to ion beams produced by conventional accelerators, they have excellent properties. They possess a small source size ($\sim 5\,\mu$m), a short pulse duration at the source (~ 1 ps), a low emittance (< 1 mm mrad) and they achieve accelerating field gradients of the order of MeV/μm. Unfortunately, they have a high divergence, embedded in a strong background radiation environment (electromagnetic pulse, X-rays, electrons). To be able to shape the beam for future applications, it is essential to control its divergence from the beginning. Most applications favor a well-defined, collimated beam with a narrow energy spread and highest peak intensities.

In this context, a test beamline was realized at GSI Helmholtzzentrum für Schwerionenforschung GmbH with the central goal to combine laser-driven ion sources and conventional accelerator elements. The beamline consists of two target chambers, which are connected by a transport line. The beamline setup and gained experimental data are briefly summarized in the following.
The Petawatt High-Energy Laser for Heavy Ion EXperiments (PHELIX) was focused on a 10 μm thin gold foil with an intensity of $10^{19}\,\mathrm{W/cm^2}$. The laser drove a Target Normal Sheath Acceleration (TNSA) source which delivered an exponentially decaying proton spectrum up to ≈ 21.5 MeV. In the next step, the proton beam was collimated by a pulsed high-field solenoid, which selected a specific energy range. For this, magnetic field strengths up to 15 T were available. Through this setting, the central energy was defined, which was transported through the whole beamline. In this thesis, the aim was a central energy value of $E_0 = 8$ MeV. Hence, the solenoid was operated at 6.5 T. Proton numbers of the order of 10^9 were measured in an energy interval of (8.5 ± 0.25) MeV. The TNSA source and the collimating solenoid were positioned in the first target chamber.
The collimated proton bunch propagated 2 m through a transport pipe and entered a radio-frequency (rf) cavity, which was operated at 108.4 MHz. Inside this element, the longitudinal beam dynamics were influenced. The particle bunch was injected at the synchronous phase of $-90°$ and was rotated in longitudinal phase space around its central energy by a certain angle. The rotation angle depended on the applied rf power. At an normalized rf cavity power of 4.10 V, an energy compression of the bunch was achieved with a spread of $\approx 3\%$. By increasing the rf power to 6.26 V, the proton bunch was temporally refocused to a bunch duration of (458 ± 40) ps at full width at half maximum (FWHM) in 6 m distance from the source. The measurement was performed with a specially developed diamond membrane detector, which had a time resolution of (113 ± 11) ps (FWHM). Behind the cavity, a 2.8 m long transport line led the beam to a second target chamber, in which diagnostics for the temporal focus were positioned. In addition, a second pulsed high-field solenoid was built-in as a final focusing system. In consequence, the beam was focused down to a focal spot size of 1.1 mm x 1.2 mm at FWHM. While the first solenoid collimated an energy interval of (8 ± 2) MeV, the rf cavity was not operated and the second solenoid focused an energy interval of (9.55 ± 0.25) MeV (due to its setting).

Using this final focusing stage, a particle intensity of 5.8×10^{19} protons/(s·cm^2) was measured within this energy interval.

After the demonstration of the final beam parameters at the interaction point in the second target chamber, a special interest was given to the use of these particle beams in future applications. This thesis concentrated on a proton imaging study. For that, it was necessary to provide a homogeneous beam. Hence, the beam homogeneity was characterized and significantly improved by using a newly developed solenoid design. As still irregularities in the transverse beam profile were visible, a mylar straggling foil was positioned in the beam path to smooth beam filamentation. For the performed application, the energy-compressed, homogeneous proton beam was used to image a solid object of different thicknesses. The image analysis showed the expected energy loss behind the different layers.

The thesis at hand deals with the optimization of the complete beamline setup including its focusing capabilities at the application point. The final beam parameters, which were reproducibly achievable at the application point, will be presented and discussed for the planning of future applications. In this context, a study of proton imaging was carried out in this work. The presented highest peak intensities will open up a new field for a variety of applications in future, e.g. stopping power measurements in a plasma, the injection into a conventional synchrotron, and the study of beam induced effects, such as pressure waves and luminescence.

Kurzfassung

Die Entdeckung der Erzeugung laserbasierter, intensiver Ionenstrahlen eröffnete ein neues Forschungsfeld. Lasererzeugte Protonenstrahlen liefern ein breites exponentiell abfallendes Energiespektrum bis nahezu Einhundert MeV. Diese Strahlen bieten gegenüber bisherigen Teilchenstrahlen exzellente Strahleigenschaften. Sie haben eine kleine Quellgröße ($\sim$ 5 µm), eine kurzen Entstehungszeit ($\sim$ 1 ps), eine geringen Emittanz ($<$ 1 mm mrad) und sie erreichen Beschleunigungsgradienten in der Größenordnung von MeV/µm. Allerdings besitzen sie eine hohe Divergenz und werden von einem starken Strahlungshintergrund (elektromagnetische Pulse, Röntgenstrahlung, Elektronen) begleitet. Es ist notwendig, die Divergenz von Anfang an zu kontrollieren, um den Teilchenstrahl zu formen. Durch die Stahlformung kann der laserbasierte Protonenstrahl für Anwendungen eingesetzt werden. Die meisten Anwendungen bevorzugen einen wohl-definierten, kollimierten Strahl mit einer geringen Energiebreite und mit einer hohen Spitzenintensität an Teilchenzahlen.

In diesem Zusammenhang wurde der Teststand einer Strahlführung am GSI Helmholtzzentrum für Schwerionenforschung GmbH realisiert mit dem zentralen Ziel, laserbasierte Teilchenquellen mit konventionellen Beschleunigerelementen zu kombinieren. Die Strahlführung besteht aus zwei Targetkammern, die durch eine Transportstrecke verbunden sind. Der Aufbau der Strahlführung und die gewonnenen experimentellen Daten werden im Folgenden kurz zusammengefasst.
Der Petawatt Hoch-Energie Laser für SchwerIoneneXperimente (PHELIX) wurde mit einer Intensität von 10^{19} W/cm^2 auf eine 10 µm dünne Goldfolie fokussiert. Der Laser erzeugte mithilfe des *Target Normal Sheath Acceleration (TNSA)*-Mechanismus ein exponentiell abfallendes Protonenspektrum. In diesem Experiment besaßen die Protonen Energien bis zu ca. 21.5 MeV. Im nächsten Schritt wurde der Strahl mithilfe eines gepulsten Hochfeldsolenoiden kollimiert. Dabei wurde eine spezifische Energiebreite ausgewählt, indem die magnetischen Feldstärke bis zu 15 T eingestellt werden konnte. Durch diese Einstellung wurde die zentrale Energie definiert, die durch die Strahlführung transportiert wurde. In diesem Experiment wurde eine zentrale Energie von $E_0 = 8$ MeV angestrebt. Deswegen wurde eine Magnetfeldstärke von 6.5 T für den Solenoiden ausgewählt. Innerhalb eines Energieintervalls von (8.5 ± 0.25) MeV wurden $\approx 10^9$ Protonen gemessen. Die TNSA Quelle und der Solenoid befinden sich in der ersten Targetkammer.
Nach einer Flugstrecke von 2 m trat das Teilchenpaket in die Hochfrequenz-Kavität ein, die auf einer Frequenz von 108.4 MHz betrieben wurde. In diesem Element wurde die longitudinale Strahldynamik beeinflusst. Das Teilchenpaket wurde bei einer synchronen Phase von -90° injiziert, so dass es um einen bestimmten Winkel um seine zentrale Energie gedreht wurde. Der Drehwinkel war abhängig von der Spannung der Kavität. Bei einer normalisierten Hochspannung von 4.10 V wurde eine Energiekompression mit einer Energiebreite von ca. 3 % erreicht. Durch die weitere Erhöhung der Hochspannung auf 6.26 V konnte der Protonenstrahl zeitlich auf eine Pulslänge von (458 ± 40) ps Halbwertsbreite (*engl.* FWHM) im Abstand von 6 m zur Quelle fokussiert werden. Die Messung wurde mit einem speziell dafür entwickelten Diamantmembrandetektor durchgeführt, der eine Zeitauflösung von (113 ± 11) ps (FWHM) aufwies.

Nach der Kavität wurde der Strahl über eine 2.8 m lange Transportstrecke in die zweite Targetkammer transportiert. In dieser Kammer stand ein zweiter gepulster Hochfeldsolenoid als letztes Fokussierungselement, mit dem eine Fokusgröße von 1.1 mm x 1.2 mm Halbwertsbreite erzielt wurde. Während der erste Solenoid bei der zentralen Energie von 8 MeV kollimierte, wurde bei diesem Schuss die Kavität nicht eingesetzt und der zweite Solenoid fokussierte das Energieintervall von (9.55 ± 0.25) MeV (aufgrund der Einstellung des Solenoiden). Mithilfe des letzten Fokussierelements wurde eine Protonenintensität von $5.8 \,\mathrm{x}\, 10^{19}$ Protonen/$(\mathrm{s{\cdot}cm^2})$ in dem Energieintervall erreicht.

Nach der Vorstellung der finalen Strahlparameter am Wechselwirkungspunkt in der zweiten Targetkammer, wurde der Fokus auf den Einsatz dieser Teilchenstrahlen in zukünftigen Anwendungen gelegt. Diese Arbeit konzentrierte sich auf die Protonenradiographie. Daher wurde die Strahlhomogenität charakterisiert und signifikant verbessert durch die Verwendung eines neu entwickelten Solenoidesigns. Da weiterhin Unregelmäßigkeiten im transversalen Strahlprofil sichtbar waren, wurde eine Streufolie aus Mylar in den Strahlengang positioniert, um die Filamentierung des Strahls zu vermeiden. Anschließend wurde mit einem energiekomprimierten Strahl die Radiographie von einem festen Objekt, das aus verschiedenen Dicken bestand, durchgeführt.

Der Kern dieser Arbeit ist die Optimierung der vollständigen Strahlführung mit ihren fokussierenden Eigenschaften am Anwendungspunkt und die Durchführung der Protonenradiographie. Die finalen Strahlparameter, die reproduzierbar am Interaktionspunkt erreicht wurden, sind wichtig für die Planung zukünftiger Anwendungen. Dabei eröffnen diese hohen Teilchenintensitäten ein Feld mit einer Vielzahl von Anwendungen wie z.B. Energieverlustmessungen im Plasma, der Injektion in ein konventionelles Synchrotron oder die Untersuchung der Materialantwort auf strahlinduzierte Effekte wie Druckwellen oder Lumineszenz.

Contents

1 Introduction

This chapter introduces the research field of this thesis. Afterwards, a closer description of the collaboration, in which the work is performed, is given and finally the thesis outline is presented.

1.1 Laser ion acceleration

The discovery of the first working ruby laser by Maiman in 1960 [Maiman, 1960] established new research fields in the whole world. Due to technological advances like Q-switching [J. McClung and Hellwarth, 1962] and mode-locking [Hargrove et al., 1964] laser pulses in the ns- and fs-regime became available. Subsequently, the key development of chirped pulse amplification (CPA) [Strickland and Mourou, 1985] enabled the access to peak powers in the terrawatt (TW) to petawatt (PW) region. If laser pulses with such intensities are focused down to several micrometers, relativistic intensities above $10^{18}\,\mathrm{W/cm^2}$ are achieved. These intensities opened up the field of relativistic laser-matter interaction and led to the discovery of a new scheme of indirect laser-based particle acceleration. Direct laser ion acceleration is not possible as laser intensities above $> 5 \cdot 10^{24}\,\mathrm{W/cm^2}$ are necessary. At present, current laser systems cannot reach these intensities yet, but such a laser system is planned at the Extreme Light Infrastructure (ELI) [Mourou et al., 2011].

One kind of the discovered indirect acceleration mechanisms is the so called Target Normal Sheath Acceleration (TNSA) [Snavely et al., 2000, Hatchett et al., 2000, Clark et al., 2000a]. When a high-power laser is focused down on a µm thin foil, the motion of electrons becomes relativistic and they are directly accelerated to energies beyond several MeV in the laser field. Electric field gradients in the order of MV/µm appear due to the charge separation and accelerate the ions in the next step. While conventional accelerators can reach only field gradients up to several MV/m at the moment due to the breakdown of the electric field [Hinterberger, 2008], plasma-based accelerators do not possess this limit because of intrinsic plasma properties [Seryi, 2015].

As a result of this discovery, laser-accelerated ion beams and their applications are now studied worldwide. Compared to conventional ion sources, they offer small source sizes ($\sim 5\,\mu\mathrm{m}$), short durations at the source ($\sim 1\,\mathrm{ps}$), a low emittance ($< 1\,\mathrm{mm\ mrad}$), huge accelerating field gradients ($\sim$ MV/µm) and high particle numbers ($\sim 10^{12}$-10^{13} protons per shot) [Roth and Schollmeier, 2016]. The drawbacks of using these sources are the broad exponentially decaying spectrum up to several tens of MeV, a large angular diver-

gence (up to 30° half envelope divergence angle) and a large background radiation environment (electromagnetic pulse (EMP), X-rays, electrons). Nevertheless, this promising field is discussed for diverse applications due to the outstanding beam properties: isochoric heating [Patel et al., 2003, Pelka et al., 2010], neutron generation [Roth et al., 2016, Kar et al., 2015], space radiation studies [Hidding et al., 2011], medical applications [Hofmann et al., 2011, Nemoto et al., 2012], time-resolved imaging of fast-transient phenomena [Mackinnon et al., 2006], or as a diagnostic tool [Mackinnon et al., 2004]. More details on applications can be found in the review by [Daido et al., 2012].

While laser-based ion sources are further optimized and intensively studied, another approach is to use one of these existing sources and control its divergence and shape with conventional technology. In this context, collaborative efforts have been undertaken to realize a tunable beamline delivering collimated, multi-MeV ion beams with a narrow energy spread. Therefore, the **L**aser **I**on **G**eneration **H**andling and **T**ransport (LIGHT) collaboration was founded to combine the TNSA mechanism with conventional accelerator structures [Busold et al., 2014a]. In the frame of this research project, a fully operational beamline was built at the GSI Helmholtzzentrum für Schwerionenforschung GmbH (GSI). The collaboration and the research project will be introduced in the following section. This thesis at hand was performed within this collaboration.

Similar projects have been done or are planned by other organisations: Nishiuchi *et al.* [Nishiuchi et al., 2019] have demonstrated the injection of a laser-based ion beam into a synchronous radio-frequency electric field and presented the concept for hadron therapy [Sakaki et al., 2019]. ELI reports on their design of a transport system consisting of a solenoid, two quadrupole triplets and an energy selector based on permanent magnets. Their goal is the demonstration of clinical applicability of laser-driven ion beams for hadron therapy as part of the ELIMED (MEDical application at ELI-Beamlines) programme [Cirrone et al., 2013, Mourou et al., 2011]. At the actual time, a beamline for Laser-driven Light Ions Acceleration (L3IA) is planned in Italy and the first commissioning experiment of the laser-driven ion source was carried out in 2017 [Gizzi et al., 2018]. At the Berkeley Lab Laser Accelerator (BELLA) Center, laser-ion sources are also studied and beamline designs are discussed. In future, laser-based accelerators are considered as a competitive alternative to huge and complex conventional accelerators, as they could be less expensive, smaller in size and offer beneficial, unique beam properties. Especially, the development of high-repetitive laser systems drives the progress in this field.

In the context of this promising research field, the LIGHT collaboration with its research project will be introduced in the following section.

1.2 LIGHT collaboration

The LIGHT collaboration was founded based on common interests to combine laser-generated ion beams with conventional accelerator technology and explore their future applications [Busold et al., 2014a]. The central goal is to examine the possibilities of beam shaping based on simulations and experiments: collimation, transport, bunching and post-acceleration of the generated proton beam.

Several German universities (Goethe-Universität Frankfurt, Friedrich-Schiller-Universität Jena, Technische Universität Darmstadt, Technische Universität Dresden) and Helmholtz institutes (GSI Helmholtzzentrum für Schwerionenforschung, Helmholtz-Institut Jena, Helmholtz-Zentrum Dresden-Rossendorf) joined the collaboration. The multidisciplinary team covers the necessary knowledge on target fabrication, laser-driven ion acceleration, high-intensity laser systems, accelerator technology, and pulsed magnetic field design. In 2018, two more partners have joined the collaboration and planned the following future projects: complementary measurements between the diamond detector and an ultrasonic method of single bunches (called: Ion-Bunch Energy Acoustic Tracing (I-BEAT)) [Haffa et al., 2018], which was developed by Technische Universität München, are intended. The Lawrence Berkeley Laboratory will support with their knowledge on simulations using the developed particle-in-cell code WARP [Vay et al., 2012].

The GSI is an ideal location for this research project, as it combines two high power laser systems as well as the necessary rf infrastructure. With the availability of a petawatt-class laser system and a large complete conventional accelerator, GSI is worldwide unique and offers many possibilities. Moreover, the LIGHT collaboration benefits from the accelerator expertise at the institute. The test beamline was realized at the Z6 experimental area, where experiments to investigate the beam shaping are performed. Figure 1.1 shows the beamline setup. The present test beamline consists of four key elements. The local **P**etawatt **H**igh-**E**nergy **L**aser for **H**eavy **I**on **EX**periments (PHELIX) hits a solid target and drives the TNSA mechanism. A selected part of the ion beam is collimated by a pulsed high-field solenoid and enters a radio-frequency (rf) cavity, in which it is rotated in longitudinal phase space. Then the proton beam travels through a transport line and is finally focused with a second pulsed high-field solenoid.

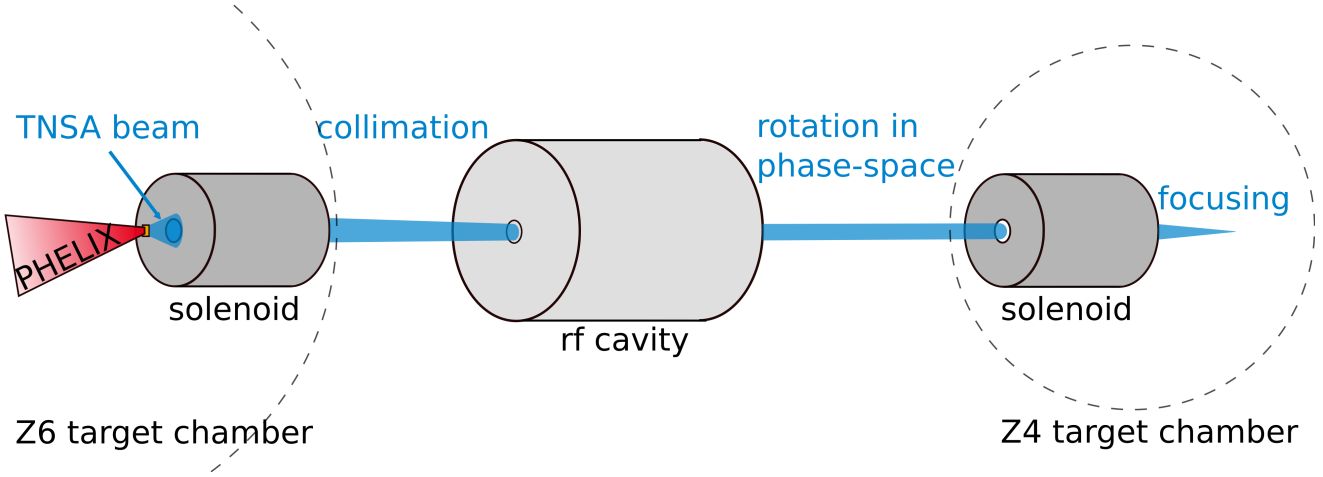

Figure 1.1: Overview of the LIGHT beamline: the PHELIX laser generates protons with MeV energies. The proton beam is collimated by a pulsed high-field solenoid and travels through a short transport line to the rf cavity. Afterwards, the beam is transported to the Z4 target chamber where a second solenoid is located for final focusing.

In future, the collaborative effort aims to provide the necessarily shaped beam for possible applications and provide next-generation accelerator technologies. Since the founding of the collaboration, the following proposed applications are discussed in this context:

- the study of a laser-driven multi-MeV ion beamline
- the use of the ion beamline as a diagnostic tool for ultra-short, time-resolved proton imaging
- providing an additional compact ion beamline for plasma physics at FAIR [HEDgeHOB collaboration, 2005]
- the exploration of warm dense matter (WDM) via isochoric heating through the high particle numbers in the MeV region in short time scales
- the investigation of energy loss measurements within a plasma based on a precise time resolution in the subnanosecond regime
- the injection of a laser-driven multi-MeV ion beam in a conventional accelerator.

1.3 Thesis outline

The goal of this work is the beam shaping of laser-accelerated protons using conventional accelerator technology components. Thereby, the achievement of highest peak intensities is desired. To evaluate these achievements the final beam parameters at the interaction point for application studies will be characterized.

The thesis at hand starts in **chapter 2** with a brief theoretical introduction on laser matter interaction and considers mainly laser pulses above $10^{18}\,\mathrm{W/cm^2}$. In the first part, the behaviour of a single electron in a laser field will be depicted, followed by the laser plasma interaction. Afterwards, different schemes of electron heating using the absorption of laser energy are described. Finally, this section will focus on the TNSA mechanism.

In **chapter 3**, particle behaviour inside a conventional accelerator is considered. Transverse and longitudinal beam dynamics are explained and the concept of emittance is introduced. The focus is centered on the working principle of a solenoid and a radio-frequency cavity, as these are two key elements of the beamline.

Chapter 4 combines the two topics about laser proton acceleration and conventional accelerator technology in the realized beamline setup at GSI Helmholtzzentrum für Schwerionenforschung GmbH. The working principle and parameters of each beamline component are described. Simulations with predictions about the beam shaping support the expectations.

In the following **chapter 5**, conducted experiments with the PHELIX laser are presented. The measured experimental data are shown and analyzed. The essential diagnostics to detect laser-driven ion beams are introduced at the appropriate stages.

Chapter 6 deals with the homogeneity of the beam. Therefore, two parameters are defined to characterize the beam uniformity. The improved beam uniformity enables proton imaging as an application.

A summary with conclusions of the experimental results is given in **chapter 7**. Finally, this thesis ends with an outlook about future upcoming projects in **chapter 8**.

2 Laser matter interaction

In the last two decades, the generation of intense ion beams based on laser-driven sources has become an extensively investigated field worldwide. These particle beams proved to possess excellent beam properties [Cowan et al., 2004,Roth et al., 2005]. Thereby, the TNSA mechanism proved to be very robust and has become the standard laser-driven source of the LIGHT research project.

This chapter gives a general theoretical description of laser matter interaction and is dedicated to the introduction of the laser-driven ion sources, focusing on the TNSA mechanism. It is based on the specialized books and PhD theses written by [Bauer and Mulser, 2007,Gibbon, 2005,Macchi, 2013, Schollmeier, 2008, Hoffmeister, 2014]. Formulas are taken from these books.

2.1 Laser electron interaction

The laser pulse is described with the form of an infinite, linear, transverse polarized electromagnetic wave that moves in z-direction:

$$\mathbf{E}(x,y,z,t) = E_0(t)\, e^{-i(\omega_L t - \mathbf{kz})}\, \mathbf{e_x} \tag{2.1}$$

$$\mathbf{B}(x,y,z,t) = B_0(t)\, e^{-i(\omega_L t - \mathbf{kz})}\, \mathbf{e_y} \tag{2.2}$$

with the electric field $\mathbf{E}$, the magnetic field $\mathbf{B}$, the time-dependent amplitudes E_0 and $B_0 = E_0/c$, the speed of light c, the laser angular frequency ω_L, and the laser wave vector $\mathbf{k}$. In this case, the relation between the electric and magnetic field is given by the third and fourth Maxwell equation: $\nabla \times \mathbf{E} = -\partial \mathbf{B}/\partial\, t$ and $\nabla \times \mathbf{B} = 1/\mathrm{c}^2\, \partial \mathbf{E}/\partial t$.

The laser intensity I_0 is routinely measured in experiments and is directly related to the electrical field amplitude by

$$E_0 = \sqrt{\frac{2I_0}{\epsilon_0 c}} \tag{2.3}$$

with the electric permittivity ϵ_0. To distinguish between the non- and the relativistic regime, it is convenient to use the dimensionless electric field amplitude a_0 which is defined as the relation between the parallel and the transverse component of the Lorentz force and can be expressed using the laser intensity and the laser wavelength λ_L:

$$a_0 := \frac{eE_0}{m_e \omega_L c} = \sqrt{\frac{I_0[W/cm^2]\ \lambda_L^2[\mu m^2]}{1.37 \cdot 10^{18}\ W/cm^2}} \tag{2.4}$$

with the electron mass m_e and the elementary charge e. For a laser pulse with an electric field amplitude $E_0 > 2.7 \cdot 10^{12}$ V/m, the laser exceeds an intensity of 10^{18} W/cm^2 according to equation 2.3. In this case, $a_0 \geq 1$ holds and the electron motion becomes relativistic. For the laser pulses used in experiments in the framework of this thesis, a_0 is between 4.9 and 6.4 and the oscillation velocity is near the speed of light.

A free electron in an electromagnetic field, such as the field of an ideal laser pulse, experiences the Lorentz force:

$$\frac{d\mathbf{p}}{dt} = -e\ (\mathbf{E} + \mathbf{v} \times \mathbf{B}) \tag{2.5}$$

with the relativistic momentum vector $\mathbf{p} = \gamma m_e \mathbf{v}$ and the relativistic factor $\gamma = (1 - v^2/c^2)^{-1/2}$, and the velocity vector $\mathbf{v}$. For a plane wave, the electric field is related to the magnetic field by $|\mathbf{E}| = |\mathbf{B}|$c. This relation implies that in approximation the second term of equation (2.5) can be neglected for non-relativistic particles. For relativistic velocities, this term becomes relevant. In the following, the non-relativistic and relativistic cases are described.

In the non-relativistic case ($v \ll c$), which corresponds to the lowest order of linear approximation of (2.5), the magnetic field $\mathbf{B}$ can be neglected and the electron oscillates transversely perpendicular in forward direction with an oscillation frequency $\mathbf{v_{osc}}$ in the x-direction

$$\mathbf{v_{osc}} = \frac{eE_0}{m_e \omega_L} \mathbf{e_x}. \tag{2.6}$$

The electron is in its initial rest position after the laser has passed this position and hence there is no energy transfer.
For $v_{osc} \simeq c$, the electric field amplitude a_0 becomes $\geq$1 and the magnetic field component $\mathbf{v} \times \mathbf{B}$ has to be taken into account and leads to an additional drift along the laser propagation direction: the electron performs a harmonic oscillation with a drift velocity

$$\mathbf{v_{drift}} = \frac{a_0^2}{4 + a_0^2}\ c\ \mathbf{e_z} \tag{2.7}$$

and the position

$$\mathbf{r}(t) = \frac{e}{m_e \omega_L^2} \mathbf{E}(\mathbf{r}, t). \tag{2.8}$$

The electron changes its position because of the drift motion and rests after this interaction resulting in no energy gain (Lawson-Woodward theorem) [Esarey et al., 1995].

2.2 Ponderomotive force

The equations in the previous section have been derived under a plane, linearly polarized wave approximation with a uniform magnitude in transversal space, which is slowly varying in time, and the field amplitudes are spatially constant. In reality, high-intensity laser pulses are strongly focussed and own a pulse duration of several hundreds of femtoseconds leading to strong radial intensity gradients in all directions. In this case, the spatial electric field distribution can be approximated by a Gaussian shape, so the intensity is highest in the center and decreases radially. Therefore, the constants E_0 and B_0 have to be changed to time- and position-dependent amplitudes $\mathbf{E}(z,t)$ and $\mathbf{B}(z,t)$. The electron is accelerated out of the intensity center to a lower intensity zone in the first half-cycle of the laser. In the second half-cycle, it experiences a reduced restoring force and does not return to its initial position. The next laser cycle effects the same behaviour of the electron leading to further displacement. Consequently, the electron is pushed out of the high-intensity zone perpendicular to the laser propagation direction. The responsible force is called ponderomotive force $\mathbf{F_p}$ and is derived from the first order of perturbation theory of the Lorentz equation (2.5) around the oscillation center. The electric field amplitude is expanded by a Taylor series to

$$\mathbf{E}(\mathbf{r},t) = \mathbf{E}(\mathbf{r}=\mathbf{r_0},t) + (\mathbf{r}-\mathbf{r_0})\,\nabla\mathbf{E}(\mathbf{r_0},t) + O((\mathbf{r}-\mathbf{r_0})^2). \tag{2.9}$$

Combined with the Lorentz equation, the non-relativistic electron equation of motion is described by

$$\frac{\partial \mathbf{v}^{(2)}}{\partial t} = -\frac{e^2}{m_e\omega_L^2}\mathbf{E}(\mathbf{r},t)\nabla\mathbf{E}(\mathbf{r},t) = -\frac{e^2}{2m_e\omega_L^2}\nabla\mathbf{E^2}(\mathbf{r},t) \propto \nabla I. \tag{2.10}$$

The multiplication with m_e and taking the cycle-average results in the ponderomotive force F_p:

$$\mathbf{F_p} = -\frac{e^2}{4m_e\omega_L^2}\cdot\nabla\left(\mathbf{E}\cdot\mathbf{E}^*\right). \tag{2.11}$$

For the relativistic case, Mulser and Bauer [Mulser and Bauer, 2010] calculated the following expression for the ponderomotive force in direction of the laser intensity gradient:

$$\mathbf{F_p} = -m_e c^2\nabla\overline{\gamma} \tag{2.12}$$

with the cycle-averaged relativistic factor for linear polarized light $\overline{\gamma} = \sqrt{1 + a_0^2/2}$. Due to the ponderomotive potential the electron gains the energy:

$$W_{pond} = (\overline{\gamma} - 1) m_e c^2. \tag{2.13}$$

Figure 2.1 illustrates the electron motion in such a relativistic laser field. Due to the momentum conservation, which is conserved in laser propagation direction, a proportional amount of momentum $p_z = W_{pond}/c = (\overline{\gamma} - 1) m_e c$ is transferred from the laser to the electron. So the electron is pushed out of the region with higher laser intensity because of the ponderomotive force and accelerated in laser propagation direction. Based on the energy relation $E^2 = m_e^2 c^4 + c^2 (p_x^2 + p_y^2)$, the angular spread of the electron trajectory is:

$$tan\ \theta = \frac{p_x}{p_z} = \sqrt{\frac{2}{\overline{\gamma} - 1}} \tag{2.14}$$

with the angle θ. The relation shows that the electron acceleration in forward direction dominates for $v_z > v_x$, which is achieved at laser intensities with $a_0 > 4$.

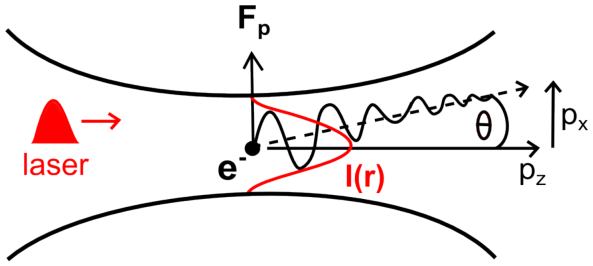

Figure 2.1: Motion of an electron in a Gaussian laser field with the intensity profile $I(r)$ [Hoffmeister, 2014]: The electron is pushed to the lower intensity zone (p_x) and at the same time the relativistic drift pushes it into laser propagation direction (p_z).

2.3 Laser plasma interaction

The achievement of laser pulse intensities above 10^{18} W/cm^2 depends on the pulse duration of the laser, its focal spot size, and its energy. Typically, the laser delivers temporal pulse profiles, which are not Gaussian. Amplified spontaneous emission (ASE) [Keppler et al., 2016] and pre-pulses propagate in front of the main pulse. The intensity ratio between the peak intensity at an arbitrary moment and the ASE level is called the laser contrast. The main pulse itself is forerunned by its slowly rising edge.

Such a high-power laser is focused on a solid target foil. The pre-pulses, the ASE level and

the increasing edge of the temporal pulse profile above I $\approx 10^9$ W/cm^2 already ionize the target generating a plasma state. Thereby, a plasma is defined as a quasineutral gas consisting of charged and neutral particles exhibiting a collective behaviour. The created plasma at the point of the laser target interaction starts to expand leading to a density gradient.

After the plasma generation, the main laser pulse interacts with the plasma, the electrons are pushed from their equilibrium position and start to oscillate collectively with the electron plasma frequency

$$\omega_p = \sqrt{\frac{e^2 n_e}{\epsilon_0 \gamma m_e}}, \tag{2.15}$$

where n_e represents the electron density. In contrast to the electron motion, the ions rest on their position because of their heavier mass. In this context of the laser-matter interaction, the refractive index η of a plasma is specified

$$\eta = \sqrt{1 - \frac{\omega_p^2}{\omega_L^2}}. \tag{2.16}$$

In the case $\omega_p < \omega_L$ (underdense plasma), the refractive index is real and the laser propagates through the plasma. For $\omega_p > \omega_L$ (overdense plasma), the refractive index becomes imaginary. In that case, the laser pulse cannot propagate further and is reflected at the so called critical density n_c. The described transition ($\omega_p = \omega_L$) between these two regions is expressed as:

$$n_c = \frac{\epsilon_0 m_e \omega_L^2}{e^2} = \frac{1.1 \cdot 10^{21} cm^{-3}}{(\lambda_L / 1\mu m)^2}. \tag{2.17}$$

Assuming a laser wavelength $\lambda_L = 1\mu$m, which is typical for the experiments at the PHELIX facility, the dimension of this characteristic parameter is of the order of $n_c \approx 10^{21}$ cm^{-3}.
For the incidence of the laser pulse at an angle $\theta \neq 0$, the laser pulse is not reflected at the density $n_e = n_c$, but it is deflected at the modified electron density n':

$$n' = cos^2(\theta)\, n_c. \tag{2.18}$$

2.4 Absorption of laser energy by electrons

During the interaction process of intense lasers with matter, a plasma is generated and the laser energy is transferred to the electrons by different absorption mechanisms. The collisionless

regime is reached for short pulse lasers above a laser intensity of 10^{15} W/cm^2 [Kiefer, 2014] and several heating processes are specified. These depend on the laser polarization and the plasma density gradient. The generation of *hot* electrons is significant for laser ion acceleration. In the following, most common absorption mechanisms are explained.

The so called resonance absorption [Kruer, 1988] occurs, when a p-polarized laser pulse (the electric field vector of the laser oscillates in the plane of incidence) hits the target with a flat density gradient at an angle $\theta \neq 0$. The laser pulse is reflected at the electron density $n' < n_c$ according to equation 2.18 and the laser component parallel to the density gradient tunnels as an evanescent wave through to the critical density n_c. At this point, the parallel part of the laser pulse excites a resonant electron plasma wave, as the plasma and the critical frequency are matched. Thereby, energy is exchanged between the laser and the plasma. The scaling for the temperature of the hot electrons T_e was found empirically [Beg et al., 1997] to be

$$T_e \propto (I\lambda_L^2)^{1/3}. \tag{2.19}$$

According to this formula, a laser pulse with a longer wavelength leads a to a more efficient resonance absorption than a pulse with a shorter wavelength.

On condition that the density gradient is very steep and the laser pulse is still p-polarized at a certain incident angle $\theta \neq 0$, the field amplitude of the resonant plasma wave will have the same order of magnitude as the electric field of the laser E_0. This mechanism is called brunel heating [Brunel, 1987, Mulser et al., 2012]. The electric field oscillates parallel to the target normal at the reflexion point. There, the field amplitude component reaches its maximal amplitude in target normal direction. During the first half-cycle, the electrons are pushed away from the plasma region into the vacuum. In the second half-cycle, the field polarity is reversed and they are accelerated behind the critical density into the target due to the steep density gradient. In the next half-cycle, the electrons are inside the target and experience only a reduced resetting force as the laser propagates only evanescently through the target. The accelerated electrons continue their propagation to the target rear side and and lose a certain amount of their energy because of collisions.

In case of s-polarisation of the laser pulse and an incident angle of 0 degree, the electric field does not possess a component parallel to the target normal and both described mechanisms can not occur. Nevertheless, in the described scenario massive electron heating is observed in experiments [Wharton et al., 1998]. This observation can be explained by the $\mathbf{j} \times \mathbf{B}$ heating [Kruer, 1988], which appears in case of relativistic laser intensities due to the magnetic field contri-

bution of the Lorentz force. The $\mathbf{j} \times \mathbf{B}$ term acts along the laser target propagation direction, while the electrons oscillate in the electric field along the target surface creating a current. The current and magnetic field are perpendicular leading to the maximal force $\mathbf{j} \times \mathbf{B}$.
Comparable to brunel heating, the electrons are accelerated first into vacuum and then inside the target again, followed by the description of brunel heating. Thereby, the electrons gain a temperature, which scales with the relativistic ponderomotive potential:

$$\overline{\Phi_p} = m_e c^2(\overline{\gamma} - 1) = 0.511[MeV]\left(\sqrt{1 + \frac{I_L \lambda_L^2}{1.37 \cdot 10^{18}[W/cm^2 \mu m^2]}} - 1\right) \cong k_B T_e \qquad (2.20)$$

with the Boltzmann constant k_B and the electron temperature T_e and the electrons propagate close to the laser propagation axis [I. K. Santala et al., 2000].

2.5 Target normal sheath acceleration (TNSA)

The previous sections explained the basics for the TNSA mechanism, which is a two-step-process. First, the electrons act as laser energy transmitters via the described absorption mechanisms. In the second step, the energy is transferred to the plasma ions.

The first laser-accelerated proton beams with multi-MeV energies were observed in three independent experiments [Snavely et al., 2000, Clark et al., 2000b, Maksimchuk et al., 2000]. They were emitted from the rear side of thin solid targets. This observation caused a worldwide interest and effort in the field of laser-driven ion acceleration. The most investigated and routinely used acceleration mechanism is the **T**arget **N**ormal **S**heath **A**cceleration (TNSA) which will be described in the following. A schematic description of the TNSA mechanism is presented in figure 2.2.
For this process, lasers are necessary which achieve peak powers between 10 TW to 1 PW and pulse durations between 10 fs to several hundreds fs. These lasers are focused down to a µm focus, so that intensities between 10^{18} and 10^{21} W/cm^2 are reached.
The laser pulse is focused on a solid target on its front side. In the case of the LIGHT research project, the target is typically made out of metal (e.g. gold, titanium) and has a thickness in the range of several tens of µm. A pre-plasma is generated on the front side of the target through the pre-pulses or the increasing flank of the main pulse, as the ionization threshold of the target is of the order of 10^9 W/cm^2. The laser main pulse interacts with the created pre-plasma: it propagates into the underdense plasma up to the critical density, where the laser pulse is reflected.

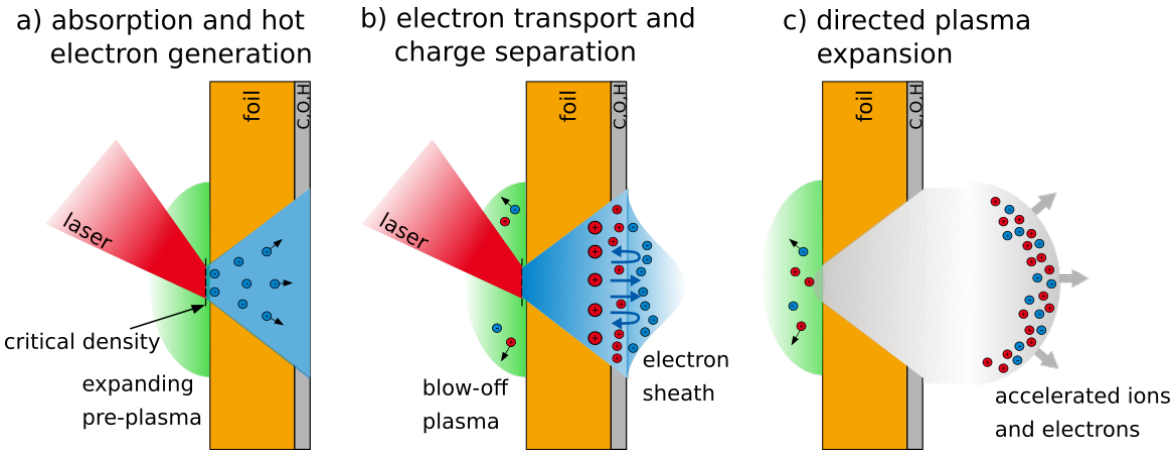

Figure 2.2: Scheme of the TNSA mechanism: a) A high-intensity laser pulse is focused on a thin metal target foil. The increasing flank or pre-pulses create a pre-plasma before the arrival of the main pulse. The main pulse propagates up to the critical density of the plasma. b) During the laser plasma interaction, electrons are accelerated to the target rear side and enter the vacuum. Here, they form an electron sheath. c) The charge separation leads to a field gradient of the order of MV/µm. Through this field, the atoms field are ionized in the contamination layer at the rear side and predominantly protons are accelerated in target normal direction resulting in a directed plasma expansion from the rear surface.

The laser energy is transferred to the plasma electrons by the described electron heating mechanisms (see section 2.4). While the *hot* electrons propagate too fast due to their high energy and are accelerated to few tens of MeVs, the *energetic* electrons are relevant for the TNSA process. They propagate to the rear side of the target (see figure 2.2 a). There, they enter the vacuum and are accumulated forming an electron sheath with an average extension of one Debye length

$$\lambda_D = \sqrt{\frac{\epsilon_0 \, k_B \, T_{e,hot}}{e \, n_{e,o}}}. \tag{2.21}$$

Because of the charge separation, the target is positively charged and an electric field with a gradient of MV/µm is generated. The formed Debye sheath on the target rear side and the potential difference U caused by this sheath is given by the electron temperature T_e multiplied by the Boltzman constant: $U \approx k_B T_e$. The electric field is strong enough to ionize the ions on the target rear side (see figure 2.2 b). During the process, the rapid electron motion is shielded by a return current of *cold* electrons.

The target rear-surface contamination layer consists of hydrocarbons and water vapour. As protons possess the lowest ionization potential and the highest charge-to-mass ratio, they are accelerated most efficiently. Moreover, the accelerated protons compensate the charge separa-

tion and thereby reduce the amplitude of the electrostatic field for heavier ions. Due to the strong field gradient, the protons obtain kinetic energies to several tens of MeVs. They expand together with comoving electrons in a charge-neutral plasma cloud (see figure 2.2c). As long as the laser pulse lasts, the energy transfer to the electrons and the ion acceleration process is sustained.

The TNSA mechanism provides protons with an exponentially decaying energy spectrum up to nearly one hundred MeV and up to 10^{13} protons per shot. The spectrum has a high-energy edge, which is called *cut-off energy*.For this mechanism, the laser-to-proton energy conversion efficiency is typically larger than 10% [Snavely et al., 2000]. As the electron temperature depends on the laser intensity I and wavelength λ: $T_e \propto \sqrt{I\lambda^2}$, the maximum proton energy is given by [Fuchs et al., 2006]

$$E_{max} \approx k_B T_e \propto \sqrt{I\lambda^2}. \tag{2.22}$$

Latest published experimental investigations of the TNSA mechanism using the PHELIX laser system report generated proton beams with a maximum energy above 85 MeV [Wagner et al., 2016]. For this experiment, the laser was focused on polymer targets with an intensity about $10^{20}\,\mathrm{W/cm^2}$.

The typical pulse duration of a TNSA source is in the picosecond regime [Roth and Schollmeier, 2016]. The accelerated proton beam has a large divergence up to 60° with a µm beam size and a very low emittance (down to $\sim 10^{-3}$ mm mrad [Cowan et al., 2004, Nürnberg et al., 2009]). In the beginning, the protons are accompanied by comoving electrons ensuring charge neutralization and preventing the proton bunch to explode due to electrostatic repulsion.

3 Beam dynamics in an accelerator

This chapter is dedicated to the beam behaviour in an accelerator. The previous chapter contained a description of the laser-driven proton source. As already pointed out, in this work these laser-generated proton beams are combined with conventional accelerator elements, which are described in the following chapter. They are used to form the beam trajectory. The construction of an accelerator determines the reference path of an ideal particle. In the case of a linear accelerator, this path is simply a straight line. As the particles possess different positions and momentums, it is necessary to push the particles back on their reference path, otherwise they will hit the beamline wall and will be lost.

In the following chapter, the relevant key technologies are explained to understand the working principle of each component in the beamline setup. This chapter starts with a introduction of the commonly used parameters to describe the motion of charged particle beams. It splits into the transverse and longitudinal beam dynamics. All motions perpendicular to the beam direction are *transverse*, while motions parallel to the beam direction are *longitudinal*. A special focus is laid on solenoids and radio-frequency cavities, which are cylindrical resonators, as these components are part of the LIGHT beamline. More details can be found in [Wille, 1996, Hinterberger, 2008, Hillert, 2015].

3.1 Transverse beam dynamics

For the complete dynamic description of a particle for at any time and at every position in an accelerator, it is necessary to know all forces in this situation. To keep particles on their transverse reference path, electromagnetic fields are utilized. Therefore, the motion of a charged particle in an electric field $\mathbf{E}$ and in a magnetic field $\mathbf{B}$ is given by the equation 2.5 for the Lorentz force, which is generalized for an ion: $\mathbf{F_L} = \frac{d\mathbf{p}}{dt} = q\,(\mathbf{E} + \mathbf{v} \times \mathbf{B})$ with the ion momentum $\mathbf{p} = m_0 \gamma \mathbf{v}$.

In an accelerator, the bending and focusing forces are produced by magnetic fields. The equivalent focusing strength of $B_0 = 1\,\mathrm{T}$ is an electric field of 300 MV/m, which is not accessible at present time [Boine-Frankenheim, 2015]. Therefore, only the force $\mathbf{F_B} = q\,(\mathbf{v} \times \mathbf{B})$ is sufficient for transverse beam dynamics considering high energies (in the MeV region).

For the description of the particle motion, a coordinate system $K(x, z, s)$ is defined whose origin goes along the reference path. The beam direction axis is named s, while the horizontal axis is called x and the vertical axis z. It is assumed that the particles move parallel to

the s direction with the coordinates $\mathbf{v} = (0,0,v_s)$. The transverse magnetic field (B_x,B_z,0) is orthogonal to the particle velocity. A force balance exists between the Lorentz force and the centrifugal force $F_Z = -m_0 v_s^2/R$ with the bending radius R. From this balance, the so called magnetic rigidity $B\rho$ is derived:

$$\mathbf{B} \perp \mathbf{v}: \qquad \frac{mv^2}{\rho} = q \cdot v \cdot B \tag{3.1}$$

$$B\rho = \frac{p}{q}. \tag{3.2}$$

The bending radius **R** is a vector dependent on the coordinates (x,z,s). Due to the force balance, the following relation is derived for the absolute value of the bending radius:

$$\frac{1}{R(x,z,s)} = \frac{e}{p} B_z(x,z,s). \tag{3.3}$$

The ideal particle moves exactly along the reference path and has the designed energy. Any other particle has a different path with small transverse deviations. For real particles, a comoving reference frame, which moves along the reference path, is chosen and their position is described in this frame. Figure 3.1 depicts the reference path of the ideal particle and the comoving reference frame.

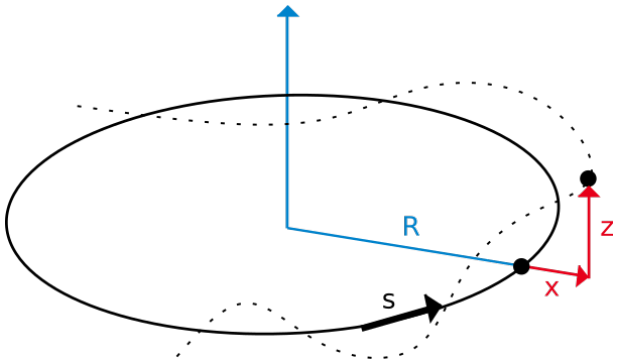

Figure 3.1: The ideal particle moves on the reference path (black), while another particle moves on a different trajectory (black, dashed). The comoving reference moves along this designed orbit. In this orbit, the position of a real particle is described (red). Adapted from [Holzer, 2016].

In the following, it is assumed that all particles have only a small position offset and a small momentum offset to the ideal particle compared to the bending radius of the accelerator. Then

the force can be approximated by a linearization around the reference point. The magnetic field is developed in a Taylor series:

$$B_z(x) = B_{z0} + \frac{dB_z}{dx}x + \frac{1}{2!}\frac{d^2B_z}{dx^2}x^2 + \frac{1}{3!}\frac{d^3B_z}{dx^3}x^3 + \ldots \quad . \tag{3.4}$$

In the same way, the expansion can be performed in the vertical direction. The multiplication with e/p leads to the multipole expansion:

$$\frac{e}{p}B_z(x) = \frac{e}{p}B_{z0} + \frac{e}{p}\frac{dB_z}{dx}x + \frac{1}{2!}\frac{e}{p}\frac{d^2B_z}{dx^2}x^2 + \frac{1}{3!}\frac{e}{p}\frac{d^3B_z}{dx^3} + \ldots \tag{3.5}$$

$$\cong \frac{1}{R} + kx + \frac{1}{2!}mx^2 + \frac{1}{3!}ox^3 + \ldots \tag{3.6}$$

$$= \text{dipole} + \text{quadrupole} + \text{sextupole} + \text{octupole} + \ldots \quad . \tag{3.7}$$

The first two multipoles are called *linear forces* and characterize the deflection of the particle. The first term $1/R$ describes an ideal dipole field with its constant force. The second term represents the linear force of the quadrupole, which produces beam focusing or defocusing with the quadrupole strength k. Higher multipoles (sextupoles, octupoles) lead typically to unwanted field errors or are used for field corrections.

The transverse beam dimension is in general very small in comparison to the dimensions of an accelerator. Therefore, it is convenient tu consider the single particle motion in the vicinity of the orbit, which is a comoving reference frame in relation to the orbit. According to several textbooks [Wille, 1996,Hinterberger, 2008], the general equations of motion of the particles are derived in the comoving reference frame. Hence, the particle transit through the magnets in an accelerator is given by:

$$x''(s) + \left(\frac{1}{R^2} - k(s)\right)x(s) = \frac{1}{R(s)}\frac{\Delta p}{p} \tag{3.8}$$

$$y''(s) + k(s)y(s) = 0. \tag{3.9}$$

These equations found the basis for linear beam optics calculations.

To determine approximately the effects of different magnetic components in the beamline, it is assumed that the magnetic field has a rectangular form with hard edges and all particles have the desired energy ($\Delta p/p = 0$). Based on these assumptions, the above equations are solved

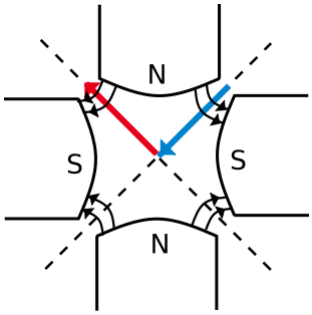

Figure 3.2: Forces inside a quadrupole: in one plane the beam is focused (blue), in the other plane a defocusing force is exerted (red).

piecewisely for the transit inside a magnet and for the field-free drift outside. This allows to rewrite the particle trajectories in matrix format:

$$\begin{pmatrix} x(s) \\ x'(s) \end{pmatrix} = \mathbf{M} \begin{pmatrix} x_0 \\ x'_0 \end{pmatrix}. \tag{3.10}$$

As an example, quadrupoles are typically used as focusing elements in an accelerator. A quadrupole focuses the beam in one plane and defocuses it in the other plane. Figure 3.2 sketches the existing forces inside this element.

Hence, the solved beam matrix for a quadrupole is given by:

$$\mathbf{M}_{\mathbf{quad}} = \begin{cases} \begin{pmatrix} cos(\sqrt{k}s) & \frac{1}{\sqrt{k}sin(\sqrt{k}s)} \\ -\sqrt{k}sin(\sqrt{k}s) & cos(\sqrt{k}s) \end{pmatrix} & \text{for k<0 (focusing)} \\ \begin{pmatrix} 1 & s \\ 0 & 1 \end{pmatrix} & \text{for k=0 (drift)} \\ \begin{pmatrix} cosh(\sqrt{k}s) & \frac{1}{\sqrt{k}}sinh(\sqrt{k}s) \\ \sqrt{k}sinh(\sqrt{k}s) & cosh(\sqrt{k}s) \end{pmatrix} & \text{for k>0 (defocusing).} \end{cases} \tag{3.11}$$

Due to their properties, quadrupoles are often combined to a doublet: the first quadrupole focuses in x-direction and defocuses in y-direction. The second quadrupole is positioned directly behind the first one and rotated by 90°. It focuses now in the y-direction and defocuses in x-direction.

Similarly, other accelerator components can be described by their individual beam matrix, hence the particle trajectory can be described as the product of several matrices. For exam-

ple, a particle travels through a beamline consisting of a solenoid (M_{sol}), a drift space (M_{drift}), a focusing (M_{foc}) quadrupole and defocusing quadrupole (M_{defoc}):

$$\begin{pmatrix} x(s) \\ x'(s) \end{pmatrix} = \mathbf{M_{sol}}\ \mathbf{M_{drift}}\ \mathbf{M_{foc}}\ \mathbf{M_{defoc}} \begin{pmatrix} x_0 \\ x_0' \end{pmatrix}. \tag{3.12}$$

For the simultaneous description of the x- and y-direction, the matrices can be combined to 4×4-matrices.

3.1.1 Pulsed high-field solenoids

While quadrupoles are used in most conventional accelerators, an alternative option are solenoids. A solenoid is a coil of wire wrapped around a piston. An electromagnetic field is created, when an electric current passes through the wire and the beam can be either focused or collimated. A descriptive and intuitive approach for the particle behaviour inside a solenoid is used by Kumar [Kumar, 2009] and sketched in the following subsection, otherwise formal derivations are found in textbooks [Busch, 1926, Reiser, 2008].

First, it is assumed that the beam is parallel cylindrical with a uniform particle distribution. All particles possess an initial velocity v_z along the z-axis. For simplicity, space-charge effects and the Coloumb repulsion between charged particles are not taken into account. Later it will be shown that for this work space-charge effects are negligible. The symmetry of the solenoid's magnetic field allows a description in cylindrical coordinates based on a radial component B_r(r,z) and an axial component B_z(r,z). The axisymmetric field of the solenoid is given by

$$B_z(r,z) = B(z) - \frac{r^2}{4}B''(z) + \cdots \tag{3.13}$$

$$B_r(r,z) = -\frac{r}{2}B'(z) + \frac{r^3}{16}B'''(z) + \cdots \tag{3.14}$$

with the distance along its axis z, the radial distance from its central axis r, and the derivatives by z. Using paraxial approximation, only terms up to the first order are considered. Furthermore, the magnetic field has the value B(z)=B_0 for 0 < z < L with the solenoid length L and B(z)=0 in all other cases. This simplifies the equation of the magnetic field to:

$$B_z(r,z) = B_0\,[H(z) - H(z-L)] \tag{3.15}$$

$$B_r(r,z) = -\frac{r}{2}B_0\,[\delta(z) - \delta(z-L)], \tag{3.16}$$

with the Heaviside step function H(z)=1 for z > 0 and otherwise H(z) = 0 and the Dirac delta function $\delta(z)$.
The particles move in a straight line in the field-free regions before and behind the solenoid. When a proton enters the solenoid, it experiences a kick in azimuthal direction resulting in a transverse velocity:

$$v_\perp = r_0 \frac{eB_0}{2\gamma m_p}. \tag{3.17}$$

Inside the solenoid (0 < z < L), the particles move on a helical trajectory with the radius $r_c = \gamma m v_\perp / e\, B_0 = r_0/2$, which is half of the initial distance to the central axis. The particles rotate with the cyclotron frequency $\omega_c = eB_0\gamma m_p$ around the center of their individual trajectories, but rotate with the Lamor frequency $\omega_L = eB_0/2\gamma m_p$ around the axis of the solenoid, resulting in a periodic focusing in the uniform magnetic field region. In conclusion, the particles move on a trajectory with the following coordinates and velocities inside the solenoid:

$$r = r_0 cos\left(\frac{\omega_L z}{v_z}\right) \tag{3.18}$$

$$\theta = \theta_0 + \frac{\omega_L z}{v_z} \tag{3.19}$$

$$v_r = -r\omega_L tan\left(\frac{\omega_L z}{v_z}\right) \tag{3.20}$$

$$v_\theta = r\omega_L. \tag{3.21}$$

When the particle leaves the solenoid, it again experiences an azimuthal kick but this time in the opposite direction. Consequently, the radial force is only remaining leading to the focusing effect. This explanation is illustrated in figure 3.3 displaying the tracjectories of two test protons.

The solenoid can be approximated as a thin lens ($L << v_z/\omega_L$) using small angle approximation ($\tan(\omega_L L v_z^{-1}) \rightarrow \omega_L L v_z^{-1}$) simplyfing equation 3.21 to:

$$v_r = -r\frac{e^2}{4\gamma^2 m_p^2 v_z} B_0^2 L. \tag{3.22}$$

Considering the derivation dr/dz, this leads to the focal length f of

$$\frac{1}{f} = \frac{e^2}{4\gamma^2 m_p^2 v_z^2} B^2 L. \tag{3.23}$$

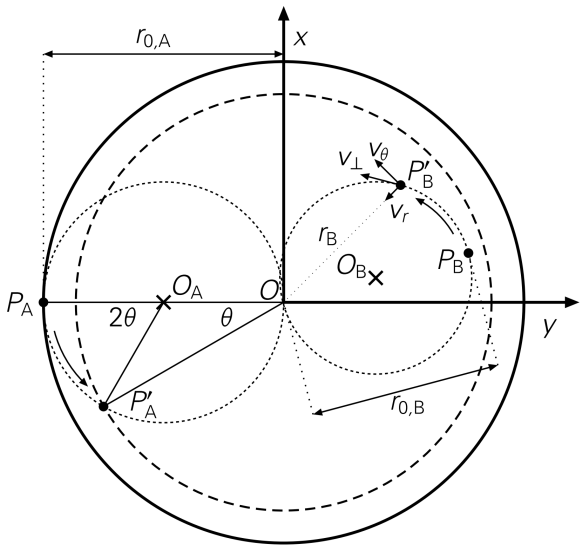

Figure 3.3: The movement of two test protons inside the solenoid (B-field shows into the drawing plane) [Kroll, 2018]: The solid line shows the border of the incoming particle distribution. The particle A enters the solenoid at the point P_A and has a distance of $r_{0,A}$ to the center O. Due to the solenoid's field, this particle moves to the position P'_A and the transverse beam size is reduced (dashed line). The motion is sketched for a second particle named B with $r_{0,B} < r_{0,A}$ with its radial (v_r) and azimuthal (v_θ) component.

In the literature, the more general expression:

$$\frac{1}{f} = \frac{e^2}{4\gamma^2 m_p^2 v_z^2} \int B^2 dz \tag{3.24}$$

is found. This formula shows that the focal length depends on the particle energy v_z and the magnetic field strength.

3.1.2 Beam emittance

In the previous sections the movement of an ideal particle in an accelerator was described. In reality, the beam is a statistical set of particles in phase space. Each particle is described by its space and momentum coordinates. As it is difficult to measure the momentums in accelerator physics, the angles x' and y', which are between the particle trajectory and the beam axis, are measured instead. Therefore, every particle is characterized by its coordinates x and x' as a point in phase space of the x dimension. In the same way, the y and y' are plotted in the phase space of the y dimension. The whole distribution in phase space usually shows an elliptical shape. The area, which is filled by the particle beam in phase space, mathematically describes the emittance $\epsilon = A/\pi$ of the beam. In experiments, the measured data is typically fitted with one standard deviation around the center is performed, so that the ellipse covers $\approx 63\%$ of the

particles (root mean square (rms) emittance).
The physical approach to the concept of emittance is to consider emittance as a measure of temperature: the particles have a random thermal motion and the beam has to be confined against thermal expansion during the transport. Without the confinement, the particles drift apart, as they start their motion with a certain momentum described by a temperature. In the case of laser-driven ion sources, the source is cold resulting in low emittance values.
In the following, the mathematical approach will be considered and the ellipse equation will be explained.

Considering the last section, the general solution of the motion equations in 3.8 can be transformed into the ellipse equation:

$$\gamma(s)x^2(s) + 2\alpha(s)x(s)x'(s) + \beta(s)x'^2(s) = \epsilon = const. \tag{3.25}$$

This equation describes the form of an ellipse in the $x - x'$ plane. It is illustrated in figure 3.4. The covered area by the ellipse is the numerical emittance $\epsilon = A/\pi$. The ellipse is normalized by the equation $\beta\gamma - \alpha^2 = 1$. α, β, and γ describe the orientation and shape of the ellipse and are called Twiss parameters. Here, α is dimensionless and describes the correlation between x and x'. α has a negative value for divergent beams and positive for convergent beams.

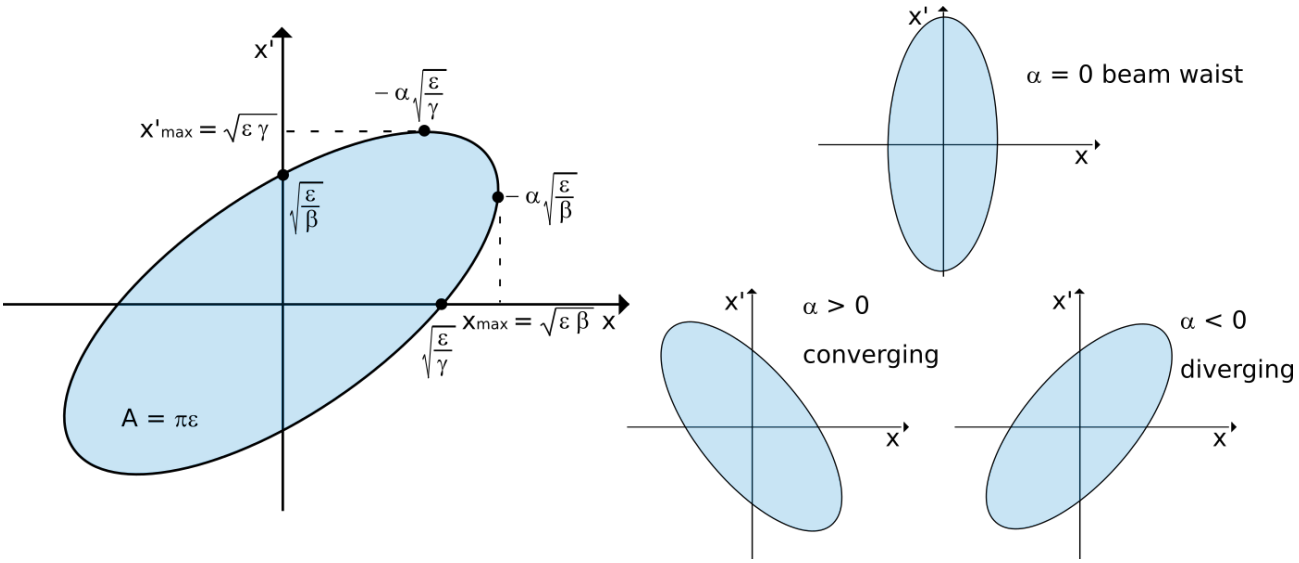

Figure 3.4: The emittance ellipse enables the calculation of the emittance value ϵ. The maximum position x_{max} and maximum angle x'_{max} determine the Twiss parameters β and γ. $\sqrt{\beta}$ represents the rms beam envelope per unit emittance and $\sqrt{\gamma}$ the corresponding beam rms divergence. α is the constant of proportionalty of the correlation between x and x'. At $\alpha = 0$ the beam has its waist. If $\alpha > 0$, then the beam converges, otherwise it diverges. The normalization of the ellipse is given by $\beta\gamma - \alpha^2 = 1$. Modified from [Hillert, 2015].

The source parameters at the beginning predefine the emittance, at which the accelerated particles leave the source, for the complete accelerator. From this point, all forces are linear and the beam is a conservative system. Inside this system, Liouville's theorem is applied, which says that every volume element of the phase space is temporally constant [Liouville, 1838]. This means that the area of the ellipse and hence the emittance are invariant, hence the integral stays constant, but its elliptical form can change along the beamline. Therefore, the emittance is used as a measure of beam quality. The smaller the emittance value, the better is the bundling of single particle trajectories to the reference path. Beams with a small emittance possess small spatial and angular deviations. They can be easily transported and enable a good spatial and angular resolution in applications. On the opposite, a large value of ϵ leads to a large beam envelope during acceleration stages. This large value results in a large angular spread during focusing. Hence, the size of the focal spot size is limited by the beam emittance.

3.2 Longitudinal beam dynamics

A particle beam typically consists of particles which differ in their energy leading to different velocities along the beam trajectory. This longitudinal displacement is expressed via the bunch duration and the energy spread along the beamline. These two parameters are crucial for several applications, which require a narrow energy spread or short bunch durations. The main control instrument for longitudinal beam dynamics are radiofrequency (rf) cavities which will be explained in the following.

3.2.1 Radiofrequency cavities

A radiofrequency (rf) cavity is used to accelerate particles using electric fields. It is a specially designed closed hollow metal structure (hohlraum), in which an electromagnetic wave with a high frequency is generated. The form and frequency of the electromagnetic wave are adapted in this way, that the wave bounces back and forth between the cavity walls. A standing wave is generated and resonance occurs. The easiest rf cavity is a cylindrical hohlraum resonator, which is sketched in figure 3.5.

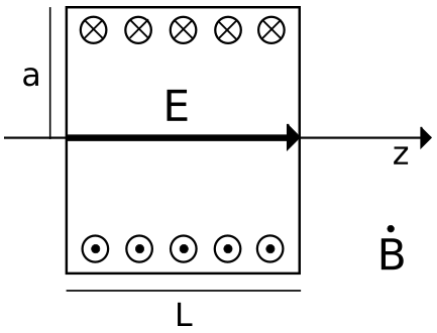

Figure 3.5: Transverse profile of a cylindrical hohlraum resonator with the electric and magnetic fields **E** and $\dot{\mathbf{B}}$. Adapted from [Hinterberger, 2008].

The geometrical design of such an rf cavity is specified for a certain particle type and particle energy. Each rf cavity can be electrically described as a parallel LCR circuit with the resonance at $\omega_L = 1/(\omega\, C)$ and the parameters capacity C, resistance R and inductance L. The maximum voltage U_{peak} depends on R and and its rf power P_{rf}:

$$U_{peak} = \sqrt{2P_{rf}R}. \tag{3.26}$$

An important characterization parameter is the cavity Q factor given by

$$Q = \frac{\omega E_{rf}}{P_{rf}} \tag{3.27}$$

where E_{rf} is the stored energy described by

$$E_{rf} = \frac{1}{2}\mu_0 \int |H|^2 dV. \tag{3.28}$$

The Q factor determines the maximum energy, which can be stored for a given input power.

So far, the principal setup of an rf cavity was described. In the following, its effect on the ion beam will be considered. The generated time-varying electric field by the cavity causes an electric force on the particles which is parallel to their direction of motion:

$$\mathbf{F_{el}} = q\mathbf{E}. \tag{3.29}$$

Most rf structures, including the used cavity of this work, produce an electric field with the form of a cosine:

$$\mathbf{E} = \mathbf{E_0}\, cos(\omega_{rf} t) = \mathbf{E_0}\, cos(\Phi_s). \tag{3.30}$$

ω_{rf} is the rf frequency and the rf amplitude determines the maximum possible amplitude $\mathbf{E_0}$ of the electric field. The synchronous phase Φ_s describes the position of the particle on the standing wave, which depends on the temporal relation between the ion beam and the rf cavity. For The last two parameters are important for the description of the working principle of the rf cavity. When a particle enters at a phase $\Phi_s = -90°$, the particle does not experience an electric force. At a phase $-90° < \Phi_s \leq 0°$, an accelerating force acts on the particle. The maximal acceleration occurs at $\Phi_s = 0°$. On the opposite, the particle is decelerated at an input rf phase

$-180° < \Phi_s < -90°$.

The time-variation of the electric field enables the fulfillment of four different functions: acceleration, de-bunching, deceleration, and bunching. Its current function depends on the temporal field behaviour during the transit of the ion. Each cavity can perform all four functions during a periodic time $\Delta\, T = 2\pi/\omega_{rf}$. In the following, a closer look is taken on its bunching capability.

Within an ion bunch, the particles have different energies, so they enter the rf structure at different rf phases. The synchronous particle enters the rf cavity at the synchronous phase Φ_s, while slower particles arrive at an rf phase larger than $> \Phi_s$ and faster particles at $< \Phi_s$. Hence, the synchronous particle experiences the electric force $e\ E_0\ cos(\Phi_s)$. The other particles have a certain energy deviation towards the ideal particle resulting in a phase deviation $\Delta\Phi = \Phi - \Phi_s$. Therefore, they are affected by the electric force $e\ E_0\ cos(\Phi - \Phi_s)$.

Figure 3.6 depicts an ion bunch, which enters the cavity with the central energy E_0 of the synchronous particle at $\Phi_s = -90°$, so that the synchronous particle is affected by zero electric field. As pointed out, particles, which are faster than the ideal particle, enter at a phase $\Phi < -90°$ and are decelerated. Slower particles enter at $\Phi > -90°$ and are accelerated.
As a result, the bunch is rotated in longitudinal phase space around this point. This motion can be described by the longitudinal phase space, which is given via the rf phase offset $\Delta\Phi$ and the resulting energy offset ΔE. In this context, the longitudinal emittance is defined as the area of the longitudinal phase space.

This rotation depends on the two parameters rf phase and rf amplitude. The later determines the rotation angle. Through this procedure, the proton bunches can be compressed in energy (small energy spread) or in time (short bunch duration). As a result, the beam is longitudinally compressed, so the cavity operates as a buncher.

The *energy-compression* of the ion bunch is achieved at a certain rf amplitude. By the increase of the rotation angle, an 'over-rotation' around the central energy of the proton bunch in phase space is accomplished. The particle bunch is rearranged dependent on the particle energy: slower particles are accelerated and propagate at the beginning of the ion bunch. The faster particles are even more decelerated and move at the tail end of the ion bunch along the trajectory outside of the rf cavity. The more energetic reference particles will catch up with the slower particles at the front. Similarly, the faster particles will reach them at a certain distance. At this point, the ion bunch has a *temporal focus* (phase focusing). Figure 3.7 illustrates the ion bunch in longitudinal phase space and its rotation.

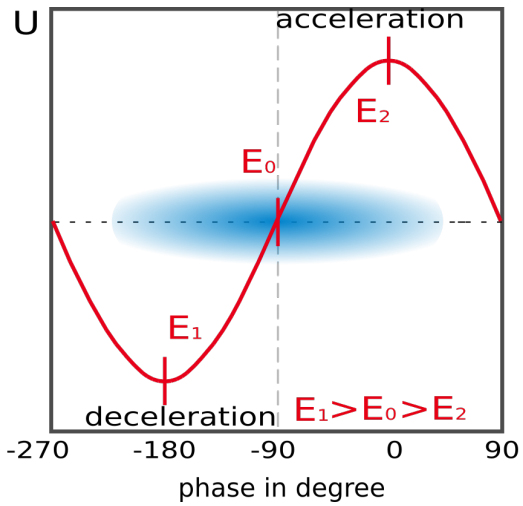

Figure 3.6: Working principle of the rf cavity: a particle bunch with a central energy spread enters the rf cavity. Protons at the central energy E_0 are injected at the synchronous phase of -90 degree and pass the cavity not being influenced. Slower protons with the energy E_2 enter the rf cavity at a later time and are accelerated, as they experience a positive electric field. On the contrary, faster protons with the energy E_1 are decelerated. The injection phase corresponds to a certain time-of-flight.

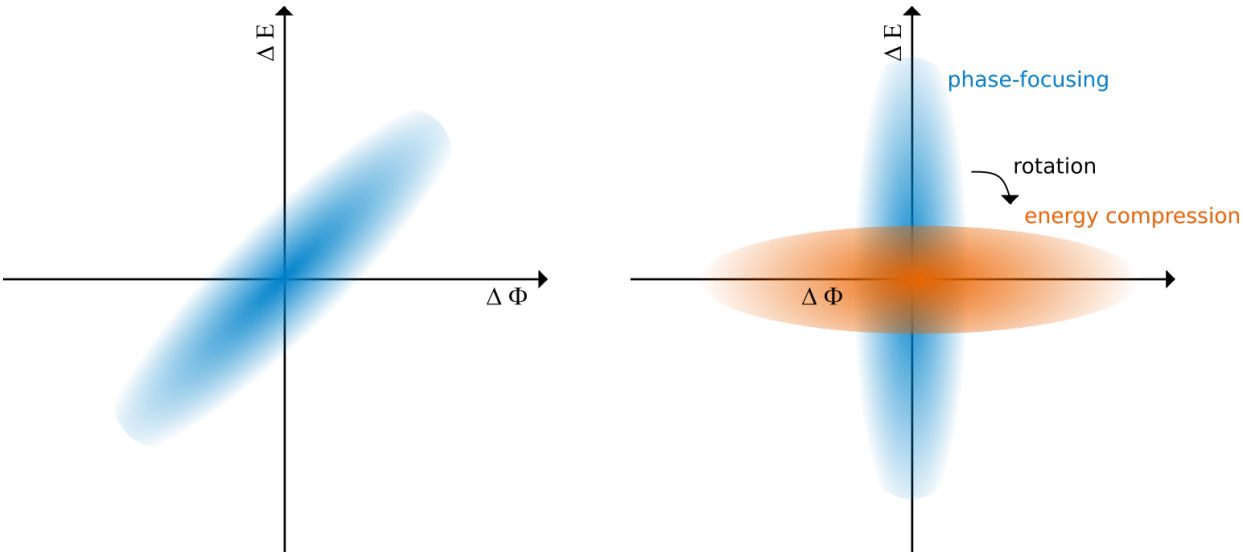

Figure 3.7: Rotation in longitudinal phase space: The particle bunch has an energy spread and a phase deviation, when it enters the cavity (left). Inside the rf cavity, the particle bunch is rotated in phase space leading to an energy-compression or phase focusing. Adapted from [Weih, 2016].

As the cavity typically consists of several accelerating gaps, the rf phase has to be correctly synchronized to the injection time. Therefore, a positively charged particle which should experience maximal acceleration is considered. When a particle enters the gap at the set phase $\Phi_s = 0°$, it is accelerated in the electric field $\mathbf{E_0}$. At this time, the second gap has the opposite field. In the next time step, the particle drifts through the field-free region and in this time the

second gap changes its direction due to the oscillating alternating field. Then the particle enters the second gap and experiences again the maximum acceleration due to the right setting of the rf phase. This process is repeated in every gap of the cavity. For a successful acceleration of the beam, its bunch length must be smaller than half of the rf cycle, so that the whole distribution experiences accelerating fields. If the bunch length is longer than half of the rf cycle, part of the bunch arrives too early or too late and gets decelerated leading to a drifting apart. For a successful injection of multiple ion bunches, it is necessary that they are a periodic time ΔT apart from each other. This temporal distance ensures that each of them is injected at the optimal phase.

4 Experimental setup and simulations of the laser-driven proton beamline

Based on the knowledge about laser-matter interaction and accelerator physics, this chapter merges these two fields. As already mentioned, the central goal of the LIGHT collaboration is the combination of a laser-driven ion source with conventional accelerator technology in form of a test beamline. In this context, the focus of this chapter is the actual beamline setup.

The origin design was developed and its functionality was demonstrated in the framework of the PhD thesis by S. Busold [Busold, 2014]. This design was changed in this work in order to achieve highest proton peak intensities. Therefore, two solenoids with an improved, compact construction were installed. Significant advances in beam shaping were necessary to provide a beam with reproducible properties for applications.

The present beamline is located at the Z6/Z4 experimental area at GSI Helmholtzzentrum für Schwerionenforschung GmbH (GSI). The Z6 experimental area is connected to the GSI linear accelerator and to the PHELIX facility, so combined experiments can be realized. The complete beamline setup is sketched in figure 4.1.

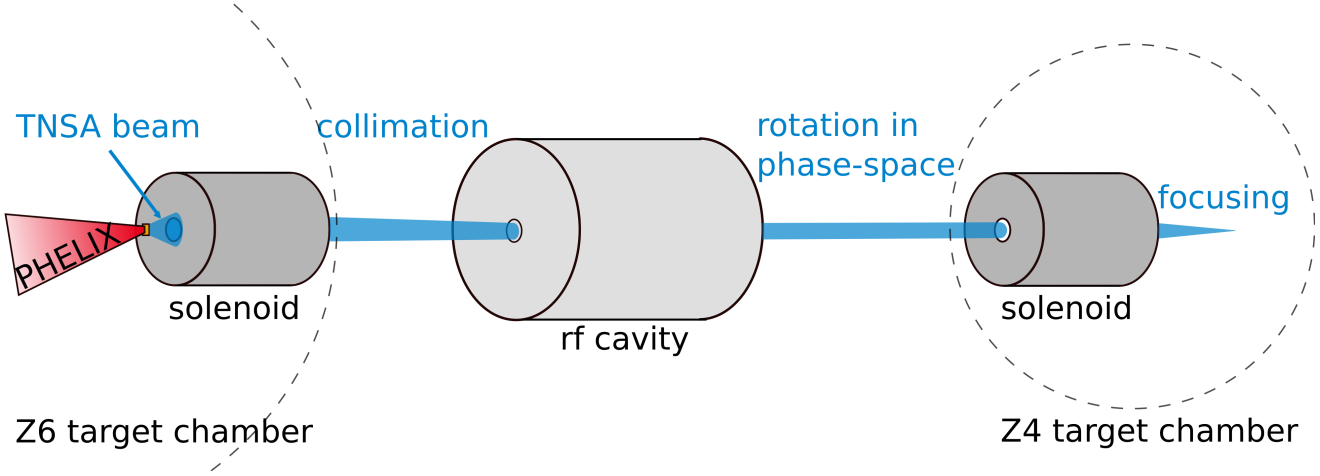

Figure 4.1: Overview of the LIGHT beamline: the PHELIX laser beam hits a thin target foil and drives the TNSA mechanism. Part of the beam enters a solenoid and is collimated over a distance of 6 m. The source and the solenoid are inside the Z6 target chamber. Through a transport line the beam propagates to an rf cavity which is used for rotation in longitudinal phase space. Afterwards, the beam is transported to the Z4 target chamber where a second solenoid is located as a final focusing stage.

The current beamline consists of a laser-driven proton source, two solenoids and an rf cavity and its total length is 6.5 m from the TNSA source. The individual beamline elements are connected by drift pipes as transport lines. These pipes have a 100 mm diameter.

This chapter describes each stage of the beamline setup step by step. It start with the PHELIX and the laser-driven proton source with its properties. Then the beam collimation with the solenoid is explained, followed by the rotation in longitudinal phase space. Finally, the final focusing system is added. These sections are accompanied by corresponding simulations based on the current beamline setup.

4.1 The PHELIX laser system as a driver for laser-accelerated ions

The driver of the TNSA source at the GSI Helmholtzzentrum für Schwerionenforschung GmbH is the PHELIX laser [Bagnoud et al., 2010]. The PHELIX facility is available to national and international users all over the world performing experiments in the fields of plasma, nuclear as well as bio physics. In plasma physics, the experiments include among othe projects laser ion acceleration, laser based neutron sources [Kleinschmidt et al., 2018], warm dense matter investigations [Kraus et al., 2018] or X-ray development [Ecker et al., 2014].

The PHELIX laser system is based on the Chirped Pulse Amplication (CPA) technique [Strickland and Mourou, 1985] and consists of a combination of flash-lamp pumped Nd:glass[1] and titanium:sapphire (Ti:Sa)[2] amplifiers. It has two different optional frontends. Therefore, the laser offers energies up to 1 kJ in a long pulse ($\sim$ ns) or up to 200 J in a short pulse ($\sim$ ps). It operates on a central wavelength of $\lambda = 1053$ nm. In this context, laser-driven ion acceleration experiments are mostly performed with the fs-frontend, as this frontend enables highest intensities on target with a pulse duration around 650 fs. Due to thermal effects in the glass amplifiers, full energy shots can be performed only every 90 minutes.

For LIGHT experiments, the fs frontend is in use and the uncompressed laser beam is transported to the Z6 experimental area. Therefore, a beamline with a subaperture of 12 cm diameter is applied as a transport line and the beam is transported to a local compressor at Z6. The beam is limited by the capability of the compressor gratings, which can handle a laser beam with 12 cm beam diameter and an energy up to 50 J. In front of the compressor, the energy of a laser pulse is measured and has a value of up to 40 J. After the compression, it has a time duration of $\approx$ 650 ps. Another transport line leads from the compressor to to the Z6 target chamber, in which the laser reaches the target interaction point. With a coated glass off-axis parabola

[1] This notation describes the lasing medium: glass is doped with neodymium ions
[2] This notation describes the lasing medium: a crystal of sapphire is doped with titanium ions

(focal length: 300 mm, full deflection angle: 22.5°) the laser pulse is focused on a target with a 3.5 µm (FWHM) focal spot size and an energy of 10-15 J. This results in an intensity higher than 10^{19} W/cm^2. For every shot, the laser energy, the pulse duration and the transverse beam profile are measured. The described experiments use an available PHELIX contrast of 10^{-6} at Z6, as their goal is beam shaping with a reliable laser-driven ion source and not source optimization.

4.2 The laser-driven proton source

The intense short laser pulse by the PHELIX laser irradiates a thin metallic foil and through this interaction energetic proton beams with high beam quality are produced via the TNSA mechanism. Without special target treatment, protons from the top contamination layer are accelerated most efficiently due to their charge-to-mass ratio [Hegelich et al., 2006]. The energy spectrum is the main drawback in working with laser-driven ion beams. In the past years, the TNSA source itself has been intensively studied in several works [Schollmeier, 2008, Nürnberg, 2010, Fuchs et al., 2006, Roth and Schollmeier, 2016] and its properties will be described in the following.

The usual proton energy distribution is exponentially decaying with a cut-off energy, which depends on the maximum electron temperature. The inhomogeneous electron distribution leads to an inhomogeneous accelerating field causing this spectrum. These beams are mathematically described by

$$\frac{dN}{dE} = \frac{N_0}{E}\, exp\left(-\frac{E}{k_B T}\right) \tag{4.1}$$

with the kinetic proton energy E, the proton temperature k_BT, and a constant N_0. The proton spectrum stopps at a certain cut-off energy and the energy region are MeVs.

Moreover, these beams are extremely laminar. Cowan *et al.* reported an transverse emittance of $< 4 \cdot 10^{-3}$ mm mrad and a longitudinal emittance of $< 10^{-4}$ eV s [Cowan et al., 2004] for TNSA beams from metal foils.

The left figure 4.2 shows the measured proton energy spectrum in the previous LIGHT campaigns. The TNSA source of the LIGHT beamline showed an exponentially decaying spectrum up to 28 MeV. The beam contains in the forward direction up to 10^{13} protons with energies above 4 MeV. This equals a conversion efficiency of laser energy to ion beam energy about ~ 10 %.
An exponential function according to equation 4.1 can be fitted to the energy spectrum. The fit parameters are $N_0 = (5.20 \pm 0.38) \times 10^{11}$ and $k_B T = (6.94 \pm 0.46)$ MeV [Busold, 2014]. For every laser shot, the proton spectrum has a similar shape. It varies due to shot-to-shot fluctu-

ations, so the exact fit parameters are dependent on laser and target parameters. The shown measurement will be used for particle tracking simulations in the next section and defines the input spectrum for the solenoid. For beam shaping, the central energy of 8 MeV is of interest, as the used rf cavity is designed for particle energies of 8 MeV/u. The spectrum contains about $\approx 10^{10}$ protons in this energy interval (8 ± 2) MeV.

Typically, the generated proton beams have a divergence of $\sim 30°$ half angle and this parameter decreases parabolically with the beam energy like in the right figure 4.2. The envelope half opening angle is distributed parabolically. In this case, the fit function is found to be $\theta(E) = -0.04E^2 - 0.41E + 26.4$ with E units in MeV.

The source size is determined by the finite diameter of the laser pulse. While protons with high energies are emitted from sources about smaller than 10 µm diameter, for lower energies the source size increases up to 200 µm [Roth and Schollmeier, 2016]. At the source, their duration is in the order of one picosecond.

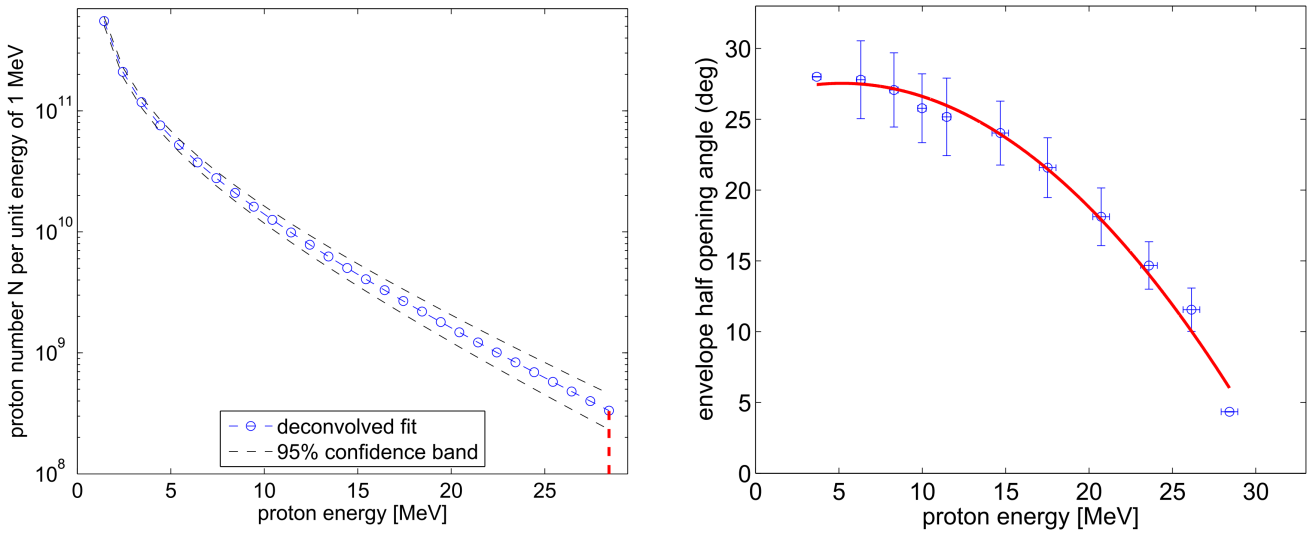

Figure 4.2: TNSA source parameters [Busold, 2014]. Left: the exponentially decaying proton spectrum from source is deconvoluted. Right: the energy-dependent envelope divergence of the TNSA beam is shown.

4.3 Beam collimation with the solenoid

As most applications require a collimated beam with a well-defined energy spread, it is necessary to control the TNSA beam divergence. For this purpose a quadrupole triplett or a pulsed high-field solenoid can be used. An experiment and simulations showed that the use of a quadrupole triplett transports less protons (one order of magnitude less than a solenoid) and exhibits an inhomogeneous beam profile [Semmler, 2018]. For that reason, solenoid is positioned 4 cm behind the source. This solenoid is designed with the goal to

capture a large part of the divergent TNSA beam. It has been designed and produced by the Helmholtzzentrum Dresden-Rossendorf and several prototypes have been tested in past campaigns [Burris-Mog et al., 2011, Busold et al., 2014b]. The currently used compact solenoid has been designed by F. Kroll [Kroll, 2018] and will be presented in the following.

The core of the solenoid is a coil out of 112 windings in four layers based on a copper wire with a cross section of 4.3 x 2.8 mm^2. Each layer is covered by a 1.5 mm of Zylon-epoxy composite. The wire itself is wrapped around a drift tube of 40.5 mm diameter and a length of 150 cm. This drift tube is part of a steel housing with a total length of 252 mm, so the coil enables magnetic fields up to 20 T. The Zylon-epoxy composite and used fiber plastics outgas under vacuum causing debris on laser optics. Moreover, the outgassing reduces the break down voltage according to the Paschen law. Therefore, the solenoid is placed inside a housing and operated at atmospheric pressure. Figure 4.3 presents the design of the described solenoid.

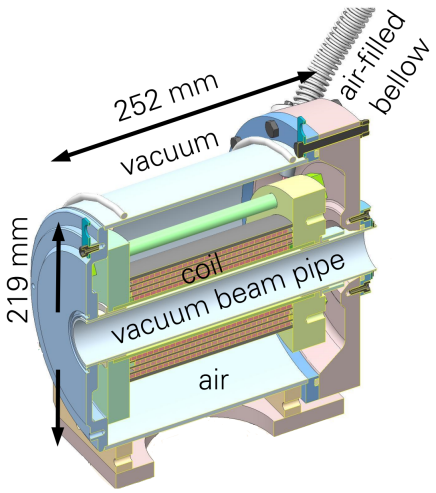

Figure 4.3: Design of the pulsed high-field solenoid [Kroll, 2018]: the ion beam propagates through the drift tube and experiences the magnetic field, which is generated by the coil out of copper windings. While the whole solenoid is placed inside the vacuum chamber, the housing is connected to the atmosphere to enable higher magnetic field strengths.

For the generation of magnetic field strengths, a capacitor-based pulse generator is necessary to drive 100 kA through the magnet. This is delivered by a specially developed pulse generator with a capacity of 180 µF and a coil inductivity of 250 µH. During the full operation of the magnet, its temperature rises approximately by 10 K [Kroll, 2018] per full energy shot, so the next full-energy shot can be performed after several minutes. For lower pulse energies, the temperature increase is smaller and higher repetition rates can be achieved. In this mode, a

repetition rate up to one shot per minute. Its maximum achievable magnetic field B_{max} of the solenoid depends on the voltage of the pulse generator U_{max} [Busold, 2014]:

$$B_{max} = 0.55 U_{max}. \tag{4.2}$$

The maximum achievable magnetic field strength of this solenoid is 15 T.

As already discussed in the previous section the generated TNSA proton beam possesses a large energy range and is divergent. Due to the beam expansion only protons, which enter the drift tube inside the solenoid, experience its magnetic force. Because of the dependancy of the solenoid's focal length (see formula 3.24) on the proton energy, different energies are focused in various distances by setting the magnetic field strength: particles with a chosen energy are focused at a certain distance behind the solenoid. At the same time, particles with a higher energy diverge and slower ions are focused at a shorter distance and diverge afterwards. This behaviour is illustrated in figure 4.4.

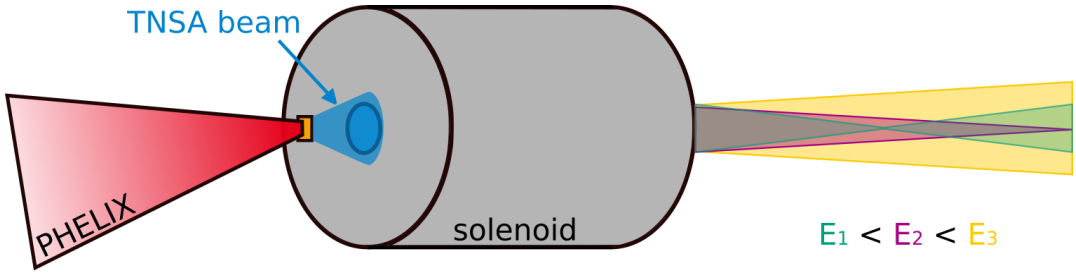

Figure 4.4: Focusing of a beam with different energies using a solenoid: the magnetic field is set in that way that particles with an energy E_2 are focused in a certain distance. Particles possessing a lower energy E_1 are focused on a shorter distance and diverge at this this point as well as particles with a higher energy E_3. Modified from [Kroll, 2018].

4.3.1 Simulated beam propagation with TraceWin

For the understanding of beam shaping, simulations are a useful tool to predict the particle behaviour and compare them with measured experimental results. While the complex laser matter interaction is calculated with computing-intensive *particle-in-cell* (PIC) simulations, particle transport and beam shaping itself can be calculated with particle tracking. In the frame of this work, the code *TraceWin*, developed by the French Alternative Energies and Atomic Energy Commission (CEA) in France [Uriot and Pichoff, 2011], is used for this task.
The *TraceWin* code calculates the beam dynamics in linear accelerator structures using ballistic particle tracking. Hereby, the beam is modeled by its second order momentum or its macropar-

ticle distribution. The different accelerator elements are given by analytical expressions or field maps.
In this case, the described TNSA proton spectrum is adapted to the capability of the *TraceWin* code (lower particle numbers). The proton distribution is determined based on the measured divergence and source size. It is used as the input parameter for the simulation. The space charge effects by the comoving electrons are neglected, as they do not affect the beam after they pass through the first component: the solenoid [Nürnberg, 2010]. From this point, *TraceWin* performs purely ballistic particle tracking.

The magnetic field of the solenoid is imported using a field map. The field map was generated by S. Busold [Busold, 2014] using the *CST particle studio*, where the coil was modeled as a symmetric current around the drift tube. The previous model is now slightly modified to the shorter solenoid design, as the coil was wrapped in a new housing. The coil length is 150 mm and the total field map length is 250 mm. For the beam collimation of the central energy $E_0 = 8\,\mathrm{MeV}$ at 6 m distance, the optimal value for the solenoid current is 7.8 kA. Therefore, the beam envelope along the beamline is calculated. The calculated transverse beam profile and phase space at a distance of 1055 mm from source are shown in figure 4.5. This distance is chosen, as at this position beam diagnostics will be set up later in the next section.

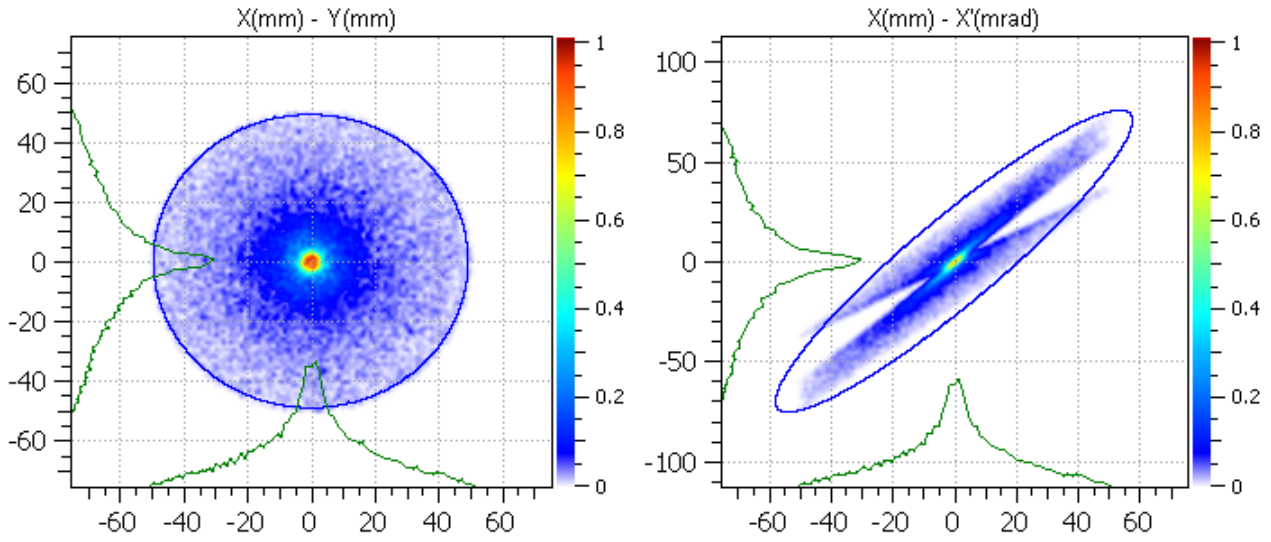

Figure 4.5: Left: the transverse beam profile of the collimated proton beam is shown at at distance of 1055 mm. Right: the phase space of the simulated beam is presented. The inclination angle α of the ellipse is smaller than zero at this point. This indicates that the beam is diverging.

The left figure shows the transverse proton distribution. The focal energy is concentrated in the center of the distribution, while higher and lower energies are in the surroundings. The outside particles possess a larger divergence and will be lost along the beamline, as either they will be blocked by an element aperture or they will hit the inner wall of the drift tube. The analysis of

the simulation predicts an energy spread of $\Delta E = 1\,\text{MeV}$ at FWHM in 1055 mm distance from source. Based on the realistic, measured particle distribution, only 5 % of all particles are collimated and the other particles are lost because of the initial high divergence. For a successful collimation, the half-envelope divergence has to be $<100\,\text{mrad}$.
While the proton bunch has a duration at source of $\approx$ 1 ps, its duration broadens during the propagation. The corresponding proton bunch duration is (4 ± 1) ns at the same position.

The right figure presents the phase space $x - x'$ with the emittance ellipse ϵ_x. As only the central energy is collimated and converges, the ellipse of the whole beam has a Twiss parameter α smaller than zero indicating a diverging beam. The *TraceWin* code predicts an emittance value of 21 mm mrad in 1055 mm distance.

4.4 Drift compression

The next component in the experimental setup is the rf cavity, in which the collimated beam is injected to influence its longitudinal beam dynamics. In conventional accelerators, this device enables a rotation in longitudinal phase space (see section 3.2.1). In the case of the LIGHT beamline, the length of the cavity and the duration of stay within the cavity are short. When the proton bunch passes this device, it experiences a force impact. The value of the force impact depends on the setting of the electric field.
The distance between the solenoid exit and the rf cavity entrance is 1780 mm, so the total distance from source to its entrance has a value of 2070 mm.

The rf cavity was designed for an energy of 8 MeV/u and had been originally operated as part of the local linear accelerator UNILAC in the framework of a PhD thesis [Häuser, 1989]. Later it has become part of the realized laser-driven ion beamline, as it operates at an energy range which is available by the used TNSA source.

The used radio-frequency cavity is a double resonator operating at 108.4 MHz. It consists of two identical coils arranged one after each other in one resonator tank possessing three accelerating gaps. In the operation mode, the electric field between the two coils is twice as strong as the electric field between one coil and an aperture. The phase of the second gap is shifted by 180°.
The cavity aperture is 35 mm, which is the narrowest tube in the whole beamline. Due to the compact design, a total voltage of 1 MV can be applied to the ion bunch based on an rf input power of 100 kW. This high gap voltage causes X-ray radiation which is mainly directed in the beam propagation direction. This background radiation can be observed in the diagnostic measurements. An overview of the cavity parameters is given in table 4.1.

Table 4.1: Technical data of the implemented rf cavity [Häuser, 1989].

technical data	
resonance frequency	108.4 MHz
optimal particle energy	8 MeV/u
shunt impedance	21.8 MΩ/m
rf power	>100 kW
length	550 mm
diameter	500 mm
open aperture	35 mm
gap length of spiral-spiral drift	40 mm
spiral drift tube length	150 mm

In the *TraceWin* simulation, the rf cavity is expressed as an analytical expression. It is constructed in the code by its three gaps and two drift spaces between the gaps according to its geometrical properties. The rf power and rf phase for each gap are set in the simulation. Through setting the parameters, the rotation angle in longitudinal phase space is determined and two scenarios are of interest: energy compression and phase focusing.

For both modes, the proton beam is injected at a synchronous phase $\Phi_s = -90°$. This leads to a rotation in longitudinal phase space around its central energy. The synchronous phase can be translated into a time scale. As the rf cavity is operated at 108.4 MHz, one periodic length is 9.2 ns and has a phase change of 360°. The equation $t = \Phi_s \cdot (9.2\,\text{ns}/360°)$ describes the relationship.

Figure 4.6 shows the simulated input energy spectrum, which enters the rf cavity, and the simulated energy spectrum behind the cavity. The input spectrum has an energy spread of $\Delta E = 5$ MeV at FWHM through the solenoid collimation. At the optimal setting of the simulation, the slower protons than the central energy are accelerated to the energy E_0 and faster protons are decelerated, which is the rotation in phase space. As a result, an energy compression around the central energy with an energy spread of $\Delta E = 0.02$ MeV at FWHM is achievable at an effective rf voltage of 0.52 V. For this case, the proton bunch duration is (3 ± 0.5) ns after the propagation through the cavity. The transversal emittance has a value of 9 mm mrad. Considering the particle numbers, 12% of the collimated beam are tracked behind the cavity.

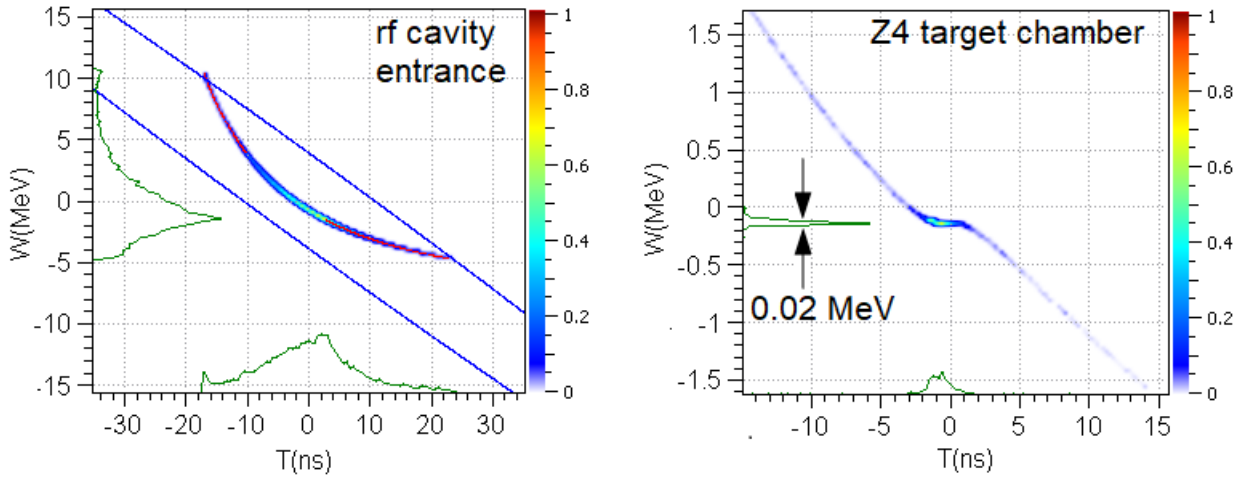

Figure 4.6: Simulations of energy compression. The time is plotted against the energy. The central energy E_0 is 8 MeV and is located at the position zero. Left: the particles enter the rf cavity with the energy spectrum in this figure at a distance of 1600 mm. Right: due to the rotation in phase space, an energy-compression of the beam is achieved. The energy spread is $\Delta E = 0.02$ MeV.

By increasing the rf power, phase focusing is achieved and the temporal focus is generated in a certain distance. The simulation results are shown in figure 4.7. The left figure shows the rotated beam at the cavity exit. The slower particles leave it at an earlier phase and progagate in front of the faster protons. The rf power is chosen in that way, that the faster protons catch up with the slower protons at a certain distance generating a temporal focus.

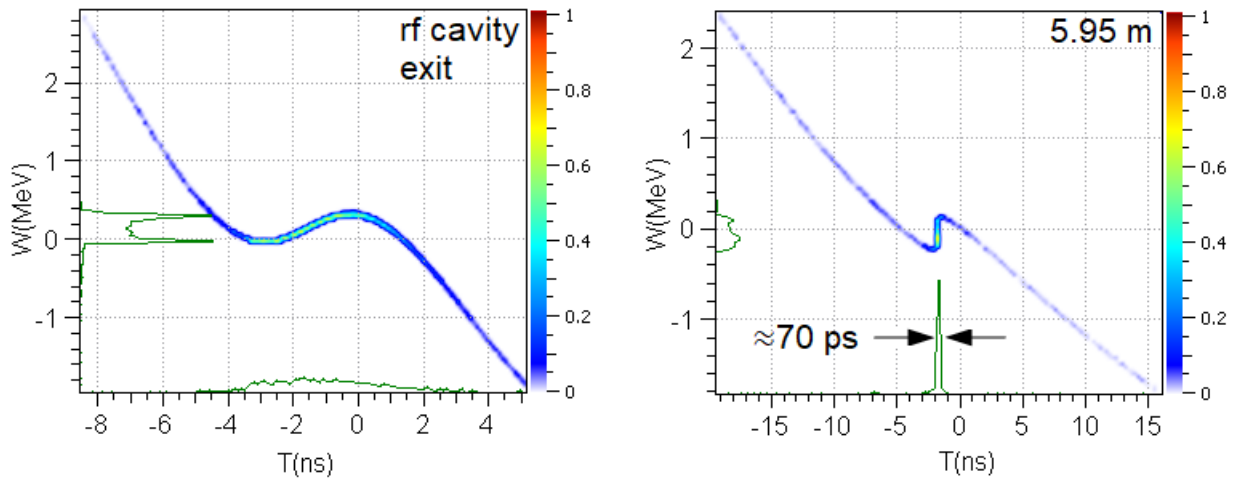

Figure 4.7: Simulations of phase focusing are shown. Left: the proton bunch is rotated in phase space by the rf cavity and presented at the cavity exit. The slower protons are in front of the faster protons. Right: over the transport line the fast protons catch up with the slow protons resulting in a temporal focus of ≈ 70 ps at 5.95 m distance to target.

The shortest proton bunch duration is predicted to be ≈ 70 ps at FWHM at 5.95 m distance. For this setting, the optimal rf power is 0.8 V in the simulation. The proton beam has a predicted energy spread of ΔE =0.2 MeV and an emittance of 19 mm mrad.

For the alignment of this beamline component, it is easier to find first the rf setting for the phase focusing because of a fast data analysis using a time-of-flight detector and then switch to the other option - the energy-compression - by decreasing the rf power by one third.

4.5 Final focusing system

Finally, the beam is transported through a 2.8 m long transport line to the second target chamber. Inside this chamber, a second solenoid is installed for final focusing. The solenoid has the same design as the first one and is positioned 5.95 m from the TNSA target. The setting of the solenoid itself has to be adjusted to the central energy of the beam, so its focal length is adapted to the distance of the diagnostics to enable the achievement of highest proton intensities at this position. The diagnostics for beam analysis can be placed behind the solenoid or in a small diagnostic chamber in front of the Z4 chamber.

In the *TraceWin* simulation, the solenoid is again represented by a field map. Through the increase of the magnetic field strength, the focal length of a specific energy is shortened. This behaviour is verified by the simulation code. Figure 4.8 presents the transverse beam profile and phase-space ellipse.

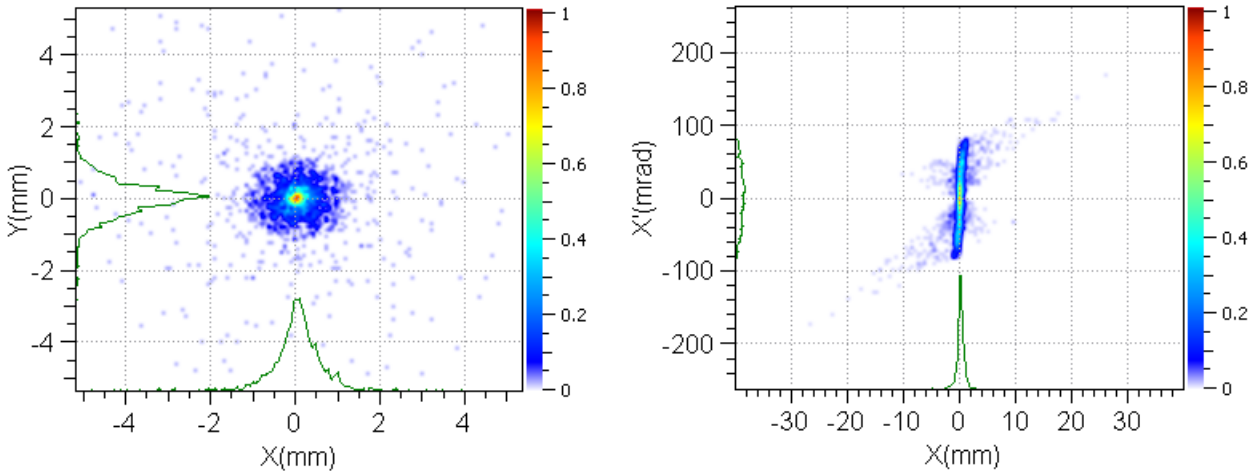

Figure 4.8: Left: the transverse focus is simulated at 5.95 m distance from source and predicts a focal spot size of 0.6 mm x 0.6 mm at FWHM for the desired energy range. The particle density is coloured and normalized. Right: the phase space of the x-direction is shown. The Twiss parameter α is about zero, so that this is the beam waist.

In the left figure, the particle distribution shows a round-shaped focal spot size for a desired energy of $E_0 = 8\,\text{MeV}$. Through variation of the magnetic field strength, the smallest focal spot size in 10 cm distance is found in the simulation for a magnetic field strength of 6.0 T. The code predicts a minimal focal spot size of 0.6 mm x 0.6 mm at FWHM based on the equation 3.24. About 4% of the collimated protons reach finally the interaction point.

At this position, the x-x' phase space of the beam is considered (right figure). The y-y' phase space has the same form because of symmetry reasons and is not illustrated. At the beam waist, which is reached at the focal length of the solenoid, the ellipse in phase space lies vertical (Twiss parameter $\alpha = 0$). Before the beam reaches this position, it is focused and the ellipse is tilted by $\alpha > 0$. After passing this position, the beam diverges ($\alpha < 0$). The simulation predicts an emittance of $(\epsilon_x, \epsilon_y) = (9.86, 9.86)\,\text{mm mrad}$.

The final focusing system can be combined with the described rotation in longitudinal phase space: energy-compressed and phase-focused ion bunches can be transversely focused to achieve high local proton intensities with the desired property.

4.5.1 Transverse space charge effects

In the context of focusing laser-driven proton beams, this subsection addresses the frequently asked question of space charge forces, whether they contribute to larger beam spots in comparison to the predictions in simulations.

Through the TNSA mechanism, an electric field is generated by the electrons on the rear side of the target, atoms are field-ionized and expand into the vacuum. The high-current ion beam can generate space-charge fields through the Coulomb interaction. The space-charge force limits its minimal focal spot size. Therefore, space-charge effects inside the focusing beam at the final focusing stage have to be considered.

At this element of the LIGHT beamline, two important forces have an effect on the ion beam: the focusing force and the space-charge force. As described in this section, the focusing force is exercised by the solenoid, whose focal length is given by equation 3.24. In magnetic transport systems, it is convenient to define the focusing strength κ. The focusing strength of the solenoid $\kappa_{solenoid}$ is specified by:

$$\kappa_{solenoid} = \frac{1}{fl} = \frac{\gamma^2 m_p v^2}{e^2 \int B dz} \tag{4.3}$$

dependent on the distance between the solenoid and the focusing position l.

The space-charge force acts as a defocusing element and is characterized by the generalized perveance K. The value of K indicates with which contribution the space charge effects the beam's motion. It is a dimensionless quantity, which is described by [Humphries, 1990, Reiser, 2008]:

$$K = \frac{qI}{2\pi\epsilon_0 m_p c^3 \gamma^3}. \tag{4.4}$$

In chapter 3, the ion beam trajectory inside an accelerator was generally described with the equation of motion 3.8. In the following, a uniform, round beam is assumed. For this special case, the equation of motion with space charge is given by [Boine-Frankenheim, 2015]:

$$x'' + \left(\kappa_{solenoid}(s) - \frac{K}{a(s)^2}\right) x = 0 \tag{4.5}$$

with the parameter $s = vt$, beam radius a, and the transverse coordinate x. The focusing strength is given by the term in brackets and is dependent on s.

For the consideration of the appearance of space-charge effects, these two terms in the above equation are estimated for the LIGHT beamline. Assuming a pulse duration of 0.5 ns, focal spot parameters of a = 1 mm, a magnetic field strengh of 5.8 T, and a kinetic energy of 8 MeV, the focusing capabilities of the solenoid and of the space-charge forces are calculated:

$$\kappa_{solenoid} = 211.5 \tag{4.6}$$

$$\frac{K}{a^2} = 0.0019. \tag{4.7}$$

The estimation shows that the focusing capability of the solenoid is far larger than the countering space-charge contribution ($\kappa_{sol} \gg K/a^2$). Taking the described beam parameters (focal spot size, pulse duration), an absolute particle number of 10^{13} protons would be necessary to reach the space-charge limit. This means the available particle number (10^8-10^9) is far below the space-charge limit and space-charge effects can be neglected. As a result, the focal spot size is limited by the beam emittance and spherical aberrations of the solenoid.

5 Experimental results on proton beam shaping

This chapter presents and discusses the experimental results for each stage of the beamline. In this context, relevant beam diagnostics are introduced in the appropriate sections.

5.1 The laser-driven proton source

The laser-driven proton source is one of the key elements of the LIGHT beamline. Before the proton beam enters the conventional accelerator elements, it is crucial to characterize the beam parameters and understand the behaviour of the TNSA source. The energy spectrum and the divergence are important parameters, which have to be considered concerning beam shaping. They are obtained by an experimental reconstruction method called radiochromic imaging spectroscopy (RIS). RIS enables to determine the energy distribution and the divergence of the beam. Through the fabrication of microstructured targets, information about the phase space can be collected [Nürnberg, 2010]. Furthermore, this method enables a fast analysis of the transverse beam profile which is especially necessary during the alignment process of the beamline elements. This section introduces the RIS method and the TNSA source is characterized. Afterwards, the emittance of the source is analyzed using a special diagnostic tool called pepperpot.

5.1.1 Radiochromic imaging spectroscopy

RIS has become a valuable diagnostic for proton detection [Nürnberg et al., 2009], as it allows a complete spatial and spectral beam reconstruction from the stack configuration of several calibrated radiochromic films (RCFs). These films are sensitive to all kinds of ionizing radiation, especially to the specific energy deposition of ions dE/dx. Heavy ions can be distinguished by their stopping power, which is proportional to Z^2, thus they are usually stopped in the first layer. Moreover, electron and X-ray exposure contributes to a signal background. On the contrary, protons penetrate through several layers due to their low stopping power leading to a two-dimensional energy-resolved particle distribution. In this process, lower energies are stopped within the front layers, while protons with higher energies are stopped in the back layers of the stack.

Radiochromic films are nearly transparent plastic films consisting out of active and substrate layers. The active layer is an organic polymer which changes its colour due to polymerization [McLaughlin et al., 1996], when it is exposed to irradiation. The strength of the colouring

is proportional to the deposited dose. The variation of different layer thicknesses and stack compositions allows to determine the spectral beam profile. As powerful laser systems usually produce an EMP which interferes with sensitive electronics, this diagnostic offers the advantage that it is not sensitive to electromagnetic noises.

In this thesis, three different types of films (HD-V2, EBT3, EBT3/2) manufactured by *Gafchromic* are in use. Their structures are shown in figure 5.1. The types differ in sensitivity and energy resolution due to their chemical compositions. These parameters are considered in the calculation of the most appropriate stack configuration for the experiment.

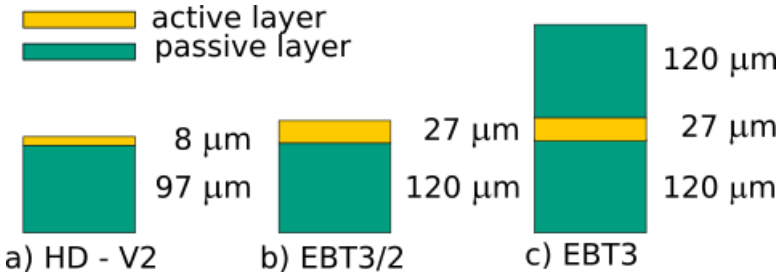

Figure 5.1: RCF types by GafChromic. The EBT3 films have a higher sensitivity compared to HD films. The HD films offer the advantage that they provide a better energy resolution. The missing substrate layer in the EBT/2 films improves the energy resolution of the RCF stack in comparison to a pure EBT3 stack.

The RCF films achieve their final colouring within 24 to 48 hours after irradiation [Niroomand-Rad et al., 1998] and afterwards are scanned with the transmission film scanner Nikon Super Coolscan 9000ED (900 dpi, 16 bit color depth per channel). The recieved data are processed with a specially developed MATLAB software [Brabetz, 2014, Schollmeier, 2008, Nürnberg, 2010]. The degree of colouring is measured in terms of the optical density (OD), e.g. the reduction in light that can be transmitted through the film. The scanner is calibrated with a grey scale wedge to convert the raw data into OD. For the analysis, a relation between OD and the absorbed dose is necessary. The conversion of OD into deposited proton energy requires an RCF calibration using accurately measured proton doses. Therefore, the used films were calibrated at the conventional TANDEM accelerator at Helmholtz-Zentrum Dresden-Rossendorf (HZDR) [Schreiber, 2012]. In the analysis, the electron signal is excluded in the image processing process by measuring the residual signal beyond the highest proton energy.

For the beam reconstruction, the characteristic Bragg curve behaviour of protons is considered. The so called *Bragg energy* of a specific RCF layer defines the initial proton energy, where the deposited energy in the active layer is the largest.
An RCF stack configuration is designed with the listed RCF types. To reduce the large RCF consumption, metal layers out of copper and nickel are placed inbetween the RCF layers. Ad-

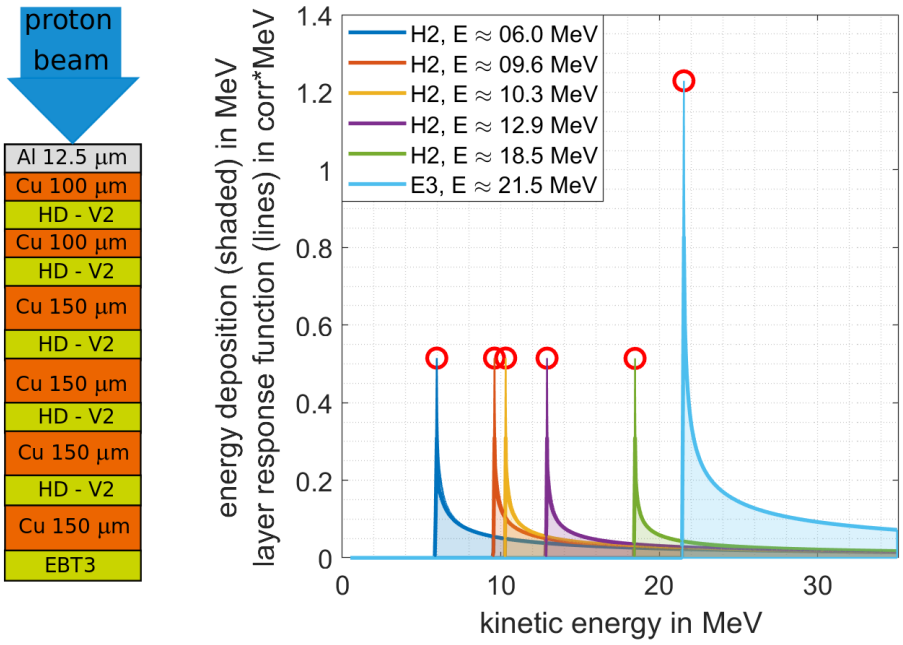

Figure 5.2: Left: the specific stack configuration consists of aluminium foil, copper, HD-V2 and EBT3 films. Right: calculated example of RCF energy deposition and its response (solid line). The protons deposit their energy in the layers before they are stopped (shaded). The Bragg peak energy describes the proton energy, where the deposited energy in the sensitive layer is the largest. It is listed in the legend and indicated with the red circle.

ditionally, an aluminium wrapping of the whole stack prevents parasitic radiation and target debris. The activation of the metal layers can be also used for nuclear activation-based imaging spectroscopy (NAIS) [Günther et al., 2013].
An example of a specific stack configuration is shown in the left figure 5.2. The stack consists of an aluminium foil, alternating copper and HD-V2 films. This specific stack configuration was used for the detection of the TNSA beam in this work.
For this configuration, the RCF stack energy deposition is calculated and shown in the right figure 5.2. Each proton deposits energy in the layers and is finally stopped. As explained, protons with lower energies are stopped in the front layers, while higher energies penetrate to the rear layers. So each film can be attributed an energy deposition distribution based on the RCF type and on SRIM energy loss tables [Ziegler, 2013].

Taking the energy loss calculation and the calibration of the RCF films into account, the RCF software calculates the convolution between the film response with an assumed exponentially decaying TNSA proton spectrum of the form:

$$\frac{dN}{dE} = \frac{N_0}{E}\, exp\left(-\frac{E}{k_B T}\right) \tag{5.1}$$

with the kinetic proton energy E, the proton temperature k_BT, and a constant particle number N_0. Beam parameters, such as initial proton spectrum, particle numbers, and cutoff energy, are extracted from this fitted spectrum. As the distance between target and stack as well as the spatial beam distribution are known, the envelope divergence angle can be determined. Therefore, a point source is assumed, as the target-detector distance is large in comparison to the source extension [Brabetz, 2014]. The envelope divergence angle α is given by

$$\alpha = tan^{-1}\left(\frac{x}{d}\right) \tag{5.2}$$

with the imprint sizes x and the distance d. In the next subsection, these parameters will be characterized for the laser-driven proton source, which is relevant for this work. All experimental data were measured in the beamtime April 2016. Measurements from different beamtimes are explicitly signified.

5.1.2 Characterization of the source

The TNSA source of this work is based on flat foil targets consisting out of 10 µm gold. At the beginning of each experimental campaign, the laser-based particle source is characterized using an RCF stack. The RCF stack is placed 4 cm behind the target and has the described configuration (see figure 5.2). The exposition of the RCF stack to the TNSA beam exhibits the typical TNSA shape of the proton spectrum. Figure 5.3 shows in the top row the obtained coloured RCF films. The proton signal is visible up to the fifth layer which has a Bragg energy of 21.5 MeV. While in previous campaigns the protons had up to 28.4 MeV (see figure 4.2), in this campaign only lower energies could be achieved due to a damaged off-axis parabola coating. This led to less energy on target and hence a lower cut-off energy in the following experiments.

The conversion of the RCF films into an energy deposition was based on an RCF calibration performed by O. Deppert with the Tandem accelerator at Helmholtzzentrum Dresden-Rossendorf. By subtracting the background and using the calibration, the energy deposition in each film is obtained and shown in the lower row of figure 5.3.
The scanned RCF films and the energy deposition show the basic round shape of TNSA beams. The diameter of the beam imprint reduces with higher layer numbers because of the divergence properties. On the last two scanned RCF films, electron background can be recognized.

The integration of the deposited energy in each film enables a quantitative analysis. Figure 5.4 shows the measured energy deposition based on the RCF layers. The proton spectrum is deconvoluted, as the response functions of each film have been calculated. As pointed out, the protons loose energy in each layer while passing the RCF stack. Therefore, each layer has to

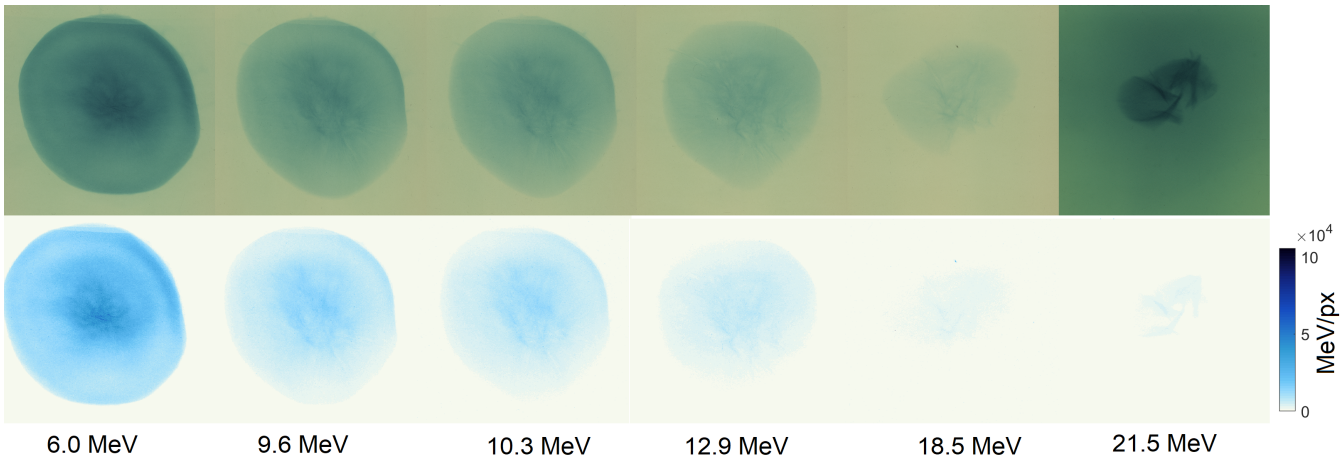

Figure 5.3: The laser-accelerated proton beam hits the RCF film stack at a position of 4 cm behind target. Top: the scanned RCF films show proton signal up to the fifth layer. Bottom: the conversion using the RCF GUI reveals the energy deposition for each film. The certain Bragg energy is attributed to each RCF film and noted below the films.

be deconvoluted with its response function (shown in figure 5.2). An exponentially decaying function of the form shown in equation 5.1 is fitted to the spectrum data.

Figure 5.5 presents the obtained energy spectrum and the fit function. The fit parameters are the maximum number of protons $N_0 = (4.48 \pm 1.10) \cdot 10^{11}$ and the temperature $k_B T = (19.35 \pm 8.64)\,\text{MeV}$. Protons are observed up to the sixth layer of the RCF stack, which has Bragg peak energy of 21.5 MeV, and hence the fitted cut-off energy has a value of $E_{cut} = 21.55\,\text{MeV}$. At the energy interval of interest of $(8 \pm 1)\,\text{MeV}$ $(1.5 \pm 0.3) \times 10^{10}$ protons are available. The laser to proton energy conversion efficiency is $(5.95 \pm 3.32)\,\%$ for energies above 4 MeV.

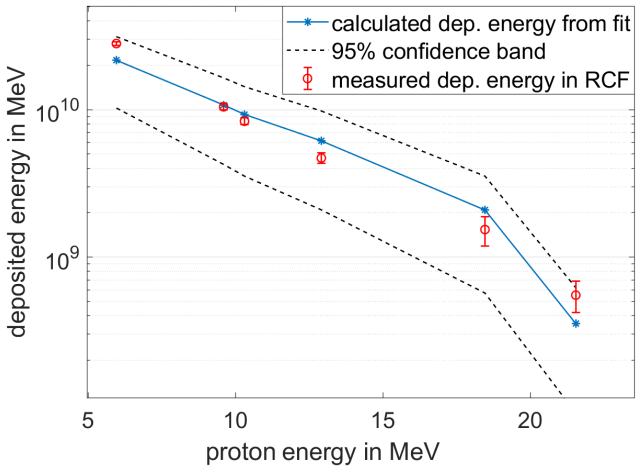

Figure 5.4: Measured and fitted energy deposition of TNSA beam.

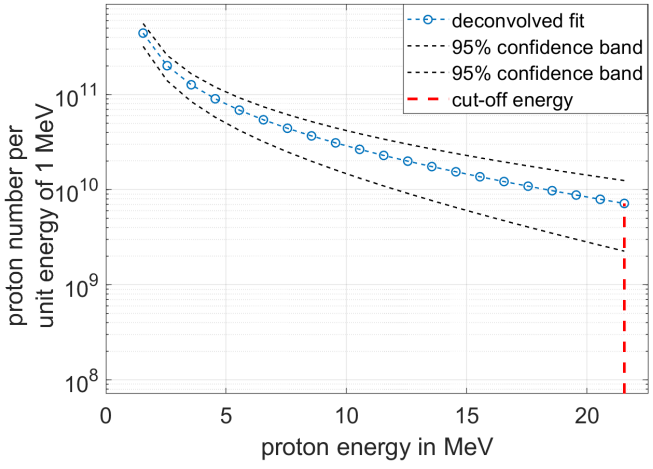

Figure 5.5: Deconvolution of proton spectrum reveals proton numbers.

Using the equation 5.2 and the data from figure 5.3, the envelope divergence of the measured TNSA beam can be determined and is depicted in figure 5.6. The divergence data are approximated with a parabolic curve of the form $\alpha(E) = a + b \cdot E + c \cdot E^2$ and given by $\alpha(E) = 25.27 + 0.71 \cdot E - 0.05 \cdot E^2$. The determined divergence angle reaches up to 27.7°, for the central energy of 8 MeV the value is $(27.5 \pm 0.2)°$.

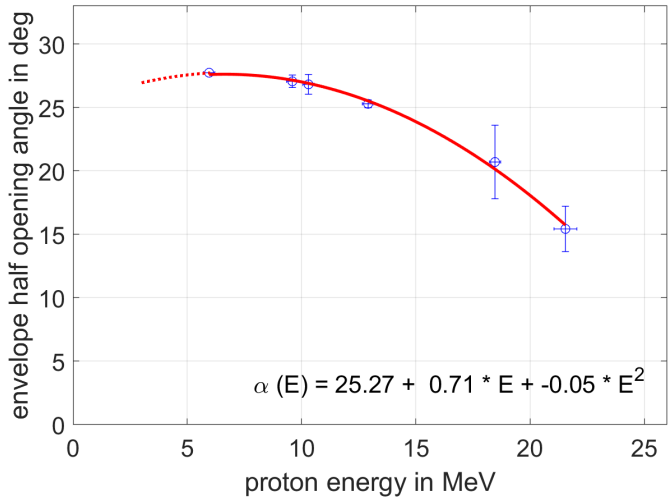

Figure 5.6: Half envelope divergence of the TNSA beam.

5.1.3 Measurement method of emittance: the pepperpot device

From the obtained source analysis, it is not possible to obtain the phase space parameters of the beam, which are necessary to calculate the emittance (explained in section 3.1.2). Therefore, another diagnostic system has to be utilized and will be introduced in the following.

For phase space representation, it is essential to obtain the spatial and angular distribution at the same time [Strehl, 2006, Forck, 2015]. The simplest way is to use a slit, which is moved laterally from shot to shot, followed by a particle detector in a certain distance. One part of the beam passes the slit, while the other protons outside the slit are stopped. The selected *beamlet* changes its transverse profile due to angular distribution during the drift to the detector. This process has to be repeated with different positions for both transverse planes. The phase space is calculated based on the measured, lateral angular distributions. This method is useful for high repetitive systems with low fluctuations between the ion bunches.

For low repetitive systems as PHELIX, it is favorable to use a device for one shot operation. Such a device is a pepperpot, a plate with identical holes. The holes are arranged in a row with the same spacing and several rows are ordered one below the other. The emittance is measured

in a single shot, so that shot-to-shot fluctuations are avoided.

Figure 5.7 shows the principle of the pepperpot measurement: the beam hits the plate and partly passes through the holes. The resulting beamlets drift to the particle detector. Each beamlet has a certain angle towards the target normal. Dependent on the drift distance, the angle for the outer beamlets increases leading to a bigger image on the particle detector. The particle detector records an intensity distribution which is proportional to the particle numbers. In this case, radiochromic films are used as the detection system. Each beamlet is characterized by its individual vertical position x_{slit} on the grid and effects an angle distribution x' within the RCF stack. This vertical position and the corresponding angle distribution are filled in the phase space diagram (see figure 5.7 right). The sum of all beamlets forms the emittance ellipse. The orientation and shape of the ellipse enables to draw conclusions on the emittance, even coupling between the two planes is detectable.

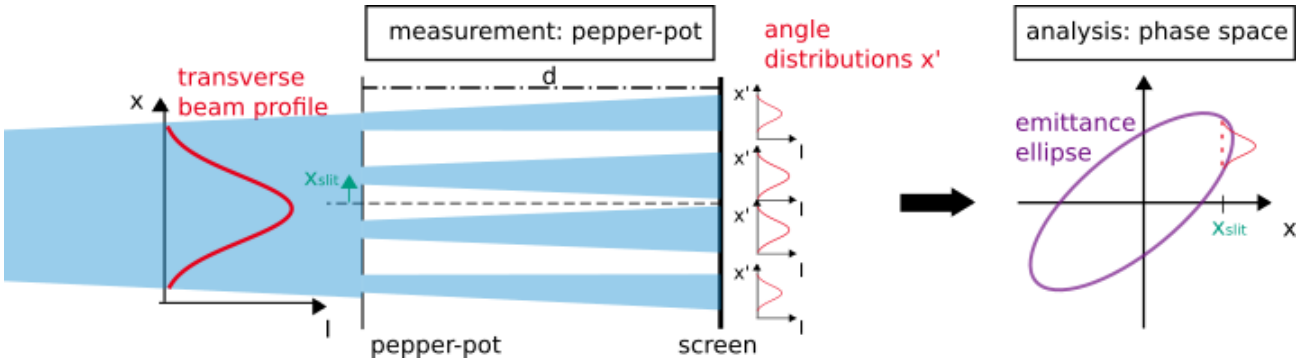

Figure 5.7: Emittance measurement with a pepperpot. The pepperpot is a matrix of pinholes enabling the measurement of the angular distribution at different positions in one shot. The beam emittance can be analyzed for both transverse planes . Adapted from [Weih, 2016, Forck, 2015].

The spatial resolution of the setup is determined by the pinhole spacing. If the pepperpot possesses many holes in a small distance from the source, the phase space parameters are obtained at many positions and the phase space diagram has a high resolution. Nevertheless, the number of holes is limited due to the fact that the single beamlets are not allowed to overlap on the screen. It is favorable that the holes have a small diameter to achieve a higher precision, however, this leads also to a decrease in intensity.

The pepperpot of the LIGHT experiment is a 30 mm thick copper plate, which has 69 holes arranged in nine rows and columns. The hole diameter is 0.3 mm and they are located in 5 mm distance to each other. Figure 5.8 presents a photograph and the hole grid of the pepperpot.

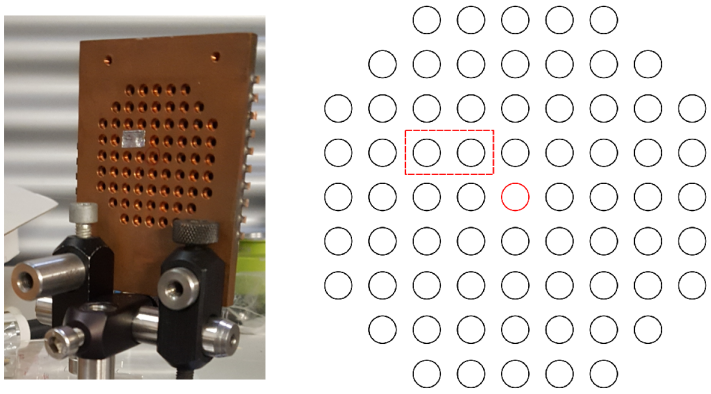

Figure 5.8: Pepperpot device [Leonhardt, 2019]. Left: photograph of the pepperpot. Right: hole grid of the pepperpot. The central hole is marked in red, the holes inside the rectangle are taped and serve as a reference for spatial orientation.

5.1.4 Emittance measurement of the TNSA source

In the framework of the beamtime in April 2016, the emittance was measured with a pepperpot device and analyzed by two supervised master students [Weih, 2016, Leonhardt, 2019]. The pepperpot was located 1055 mm behind the source and its screen, an RCF stack, was positioned 600 mm away from the pepperpot itself. The RCF stack consisted of a 12.5 µm thin aluminium foil followed by three films of the type EBT3. The geometrical parameters of the setup led to a lower resolution limit for the 1σ-emittance of 0.64 mm mrad.

Figure 5.9 shows the image of the first RCF layer, which has a Bragg peak energy at 4 MeV. The signal on the RCF film layers is very low, but after image processing a magnified image of the pepperpot grid can be recognized. The magnification corresponds to the geometrical distances of the setting. This image indicates the point-source like behaviour of the TNSA source, which is expected from beams with a small emittance. So the source measurement can be used as a calibration grid for further measurements like the emittance measurement behind the switched-on solenoid.

The analysis of the RCF films enables the reconstruction of phase space with a fitted 1σ ellipse [Weih, 2016, Leonhardt, 2019]. Figure 5.10 shows the phase space. The value of the source emittance is evaluated as $\epsilon_{rms,x} = (1.0 \pm 0.4)\,\text{mm mrad}$ in x-direction and $\epsilon_{rms,y} = (0.8 \pm 0.4)\,\text{mm mrad}$. Considering the uncertainties, the values are near to the resolution limit and indicate a small source emittance.

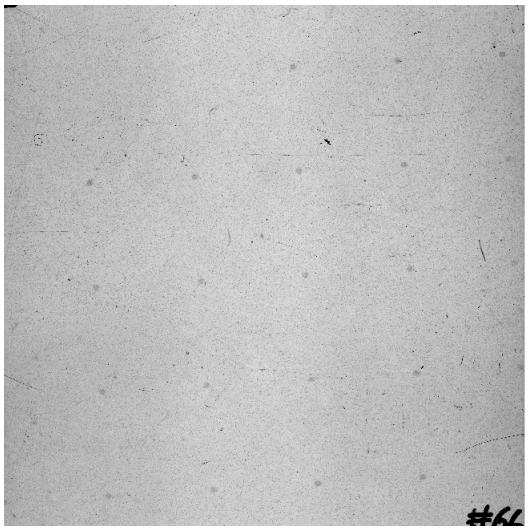

Figure 5.9: RCF image of the source pepperpot measurement at a Bragg peak energy of 4 MeV.

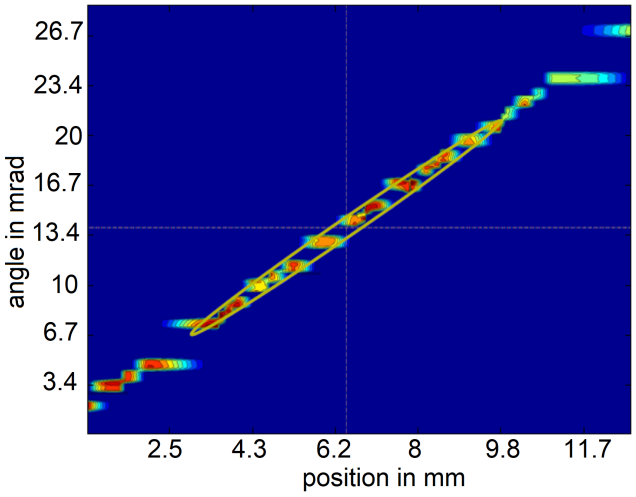

Figure 5.10: Phase space diagram of the TNSA source [Weih, 2016]: the emittance is fitted based on a 1σ-ellipse.

5.2 Collimation and energy selection

Most applications require a collimated beam with a well-defined energy spread. Therefore, it is necessary to control the beam divergence in the LIGHT beamline. This control is realized by a pulsed high-field solenoid, which is positioned 4 cm from the TNSA source. A lower distance between target and solenoid ensures that more particles enter the solenoid. In this case, the distance cannot be reduced, as the free space between the target and solenoid is necessary for the target alignment diagnostic.

The magnetic field strength is set to a certain calculated value according to simulations, so that the beam is collimated at the selected central energy along the beamline. For that reason, the solenoid is operated at a pulser voltage of 12 kV, which corresponds to a current of 7.8 kA. Due to the relation $B^{coil}_{z,max} \approx 0.84\ I^{coil}_{max}$, the magnetic field strength has a value of 6.5 T. This setting is in compliance with the *TraceWin* simulations and previous experiments. The beam collimation of the LIGHT beamline was intensely studied by S. Busold [Busold, 2014] demonstrating the collimation at a central energy of (10 ± 1) MeV. He reported on an energy spread of $(18 \pm 3)\%$ at FWHM around the selected energy $E_0 = 9.6$ MeV and measured a measured bunch duration of 8.6 ns in 3 m distance from the source. Within this energy interval, 34% were transported through the beamline.

The transverse beam position is very sensitive to the solenoid position, which has to be aligned in every experiment. For the measurement of the transverse position as part of the beamline

alignment, the energy spectrum after chromatic focusing is qualitatively analyzed with an RCF stack. The RCF stack can be positioned along the beamline in different ports, so the beam can be thread through the beamline. In this case, it was positioned 3.1 m behind the target and consists of a 12.5 µm aluminium foil followed by three EBT3 films (corresponding Bragg energies: 3.7 MeV, 6.5 MeV, and 8.5 MeV). The collimated proton beam hits the RCF film and causes an energy deposition. Figure 5.11 shows the transverse beam profile after the conversion based on the calibration. It is observed that the beam has rhombic shape and exhibits irregularities.

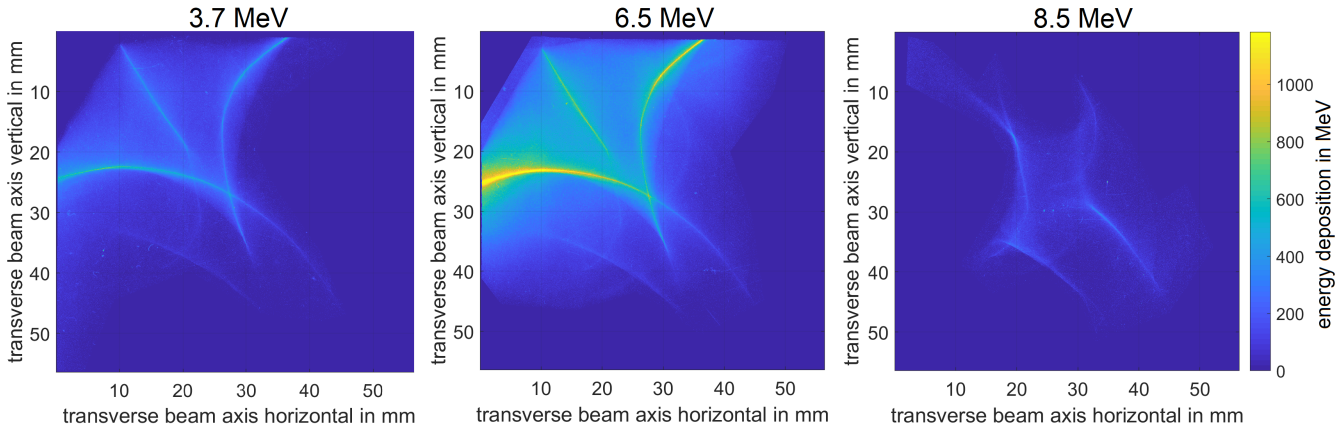

Figure 5.11: Energy deposition of the beam collimation in the RCF layers. The corresponding transverse beam profile is shown for each layer. The black number above the figures is the Bragg energy of the RCF layer. Left figure shows the beam profile at a Bragg energy of 3.7 MeV. The middle figure has a Bragg energy of 6.5 MeV. In this layer is the highest particle intensity. The right figure presents the RCF film at a Bragg energy of 8.5 MeV and proton numbers decrease in this film.

The simulations of the previous chapter predict an Gaussian energy spread around the central energy with a Gaussian shape. Because of that, the spectrum has not an exponentially decaying form any more and the MATLAB software (see section 5.1.1) can not be used for shaped proton beams. In the frame of this thesis, a MATLAB code was written to deconvolute the beam spectrum from the scratch and will be mathematically described in the following.

The RCF stack consists of n active layers. It is assumed that 90% of the stopped protons are inside an energy interval ΔE which contains the Bragg peak energy. An energy bin is assigned to each film with its average Bragg energy $E_{Bragg,k}$ and the index k. First, the deposited energy E_{dep} of the last RCF layer is converted to absolute proton numbers N in this layer:

$$N_n = \frac{E_{dep,n}}{E_{Bragg,n}}. \tag{5.3}$$

The protons deposit energy in all front layers according to the energy loss tables within an energy interval. In the second last layer $(n-1)$ the energy deposition of the protons, which have reached the last layer, can be calculated by:

$$E_{dep,N_n,n-1} = N_n E_{loss,n-1} \left(\frac{dN_n}{dE} \right) \Bigg|_{E_{Bragg,n}-0.5\Delta E}^{E_{Bragg,n}+0.5\Delta E}. \tag{5.4}$$

Through the subtraction of the deposited energy $E_{dep,n-1}$, the stopped proton number in this layer N_{n-1} can be determined:

$$N_{n-1} = \frac{E_{dep,total,n-1} - E_{dep,N_n,n-1}}{E_{Bragg,n-1}}. \tag{5.5}$$

In this way, the absolute proton numbers in the other layers are calculated:

$$N_k = \frac{E_{dep,total,k} - \sum_{i=k}^{n} E_{dep,N_i,i}}{E_{Bragg,i}}. \tag{5.6}$$

Until now, only active layers of the RCF have been considered. However, the protons also lose energy in the inactive substrate layers. Taking these into account, the stopped proton number in inactive layers is estimated by a linear fit between adjacent active layers and subtracted. Through multiple iteration, the RCF image is successfully deconvoluted. Moreover, this developed code is able to determine the proton energy spectrum per pixel and locate high proton intensities in the beam profile.

Applying the deconvolution algorithm to the measured RCF data, the energy spectrum behind the solenoid is obtained, which is shown in figure 5.12.

The maximum of the proton distribution is found in the second RCF film: $(1.12 \pm 0.06) \times 10^9$ protons are measured within an energy interval of (6.5 ± 0.25) MeV. These are 12% of the initial TNSA energy interval. The total particle number in the whole RCF is $(1.22 \pm 0.12) \times 10^9$ protons.

The energy and particle distribution measurement is in agreement with the *TraceWin* simulation, which is coloured blue in the figure. It would be desirable to reach a higher energy resolution for a more precise comparison. The irregularities in the transverse beam profile are not observed in the simulation and their formation will be investigated by the collaboration partner HZDR, where the solenoids are being developed.

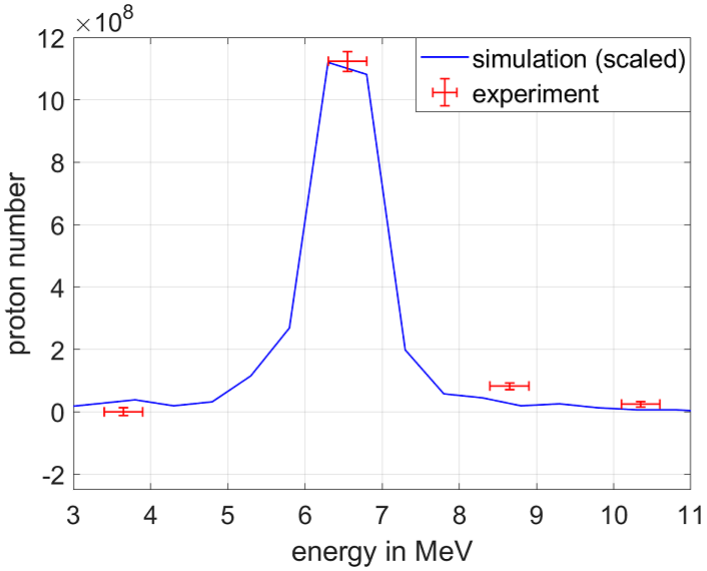

Figure 5.12: The energy spectrum of the collimated beam in 3.1 m distance is shown. For each layer the calculated particle number is listed in the distribution. The highest particle number is found in the second film, so this is the central energy interval for this setting. The comparable *TraceWin* simulation is shown in blue, while the measured data are marked red.

5.2.1 Emittance of the collimated beam

The same setup with the same positions, which is used for the emittance measurement of the source (see section 5.1.4), is applied to the emittance measurement using the turned-on solenoid. The solenoid is operated again at 12 kV and the pepperpot is positioned in a distance of 785 mm behind the solenoid.

The beamlets cause a well-distributed pattern on the RCF layers (see figure 5.13). The analysis of the phase space leads to an emittance of $\epsilon_{rms,x} = (5.5 \pm 1.0)$ mm mrad for the x-direction and $\epsilon_{rms,y} = (4.0 \pm 1.7)$ mm mrad for the y-direction. Figure 5.14 shows the fitted ellipse in the phase space. Due to the chromatic focusing, the emittance values increase, but the beam is still laminar. Compared to the *TraceWin* simulation, which predicted an emittance of $(\epsilon_x, \epsilon_y) = (9.86, 9.86)$ mm mrad, the experimental results are lower. The primary cause of this is that the emittance is analyzed for one selected energy, which is stopped in the RCF film, while the code calculates a total beam emittance.

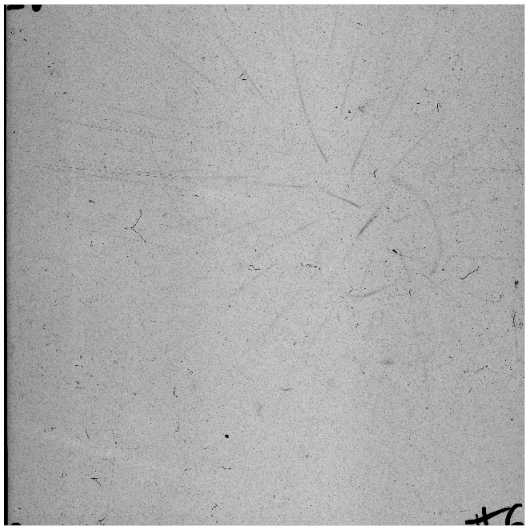

Figure 5.13: RCF image of the pepperpot measurement with a collimated beam at a Bragg peak energy of 8.5 MeV.

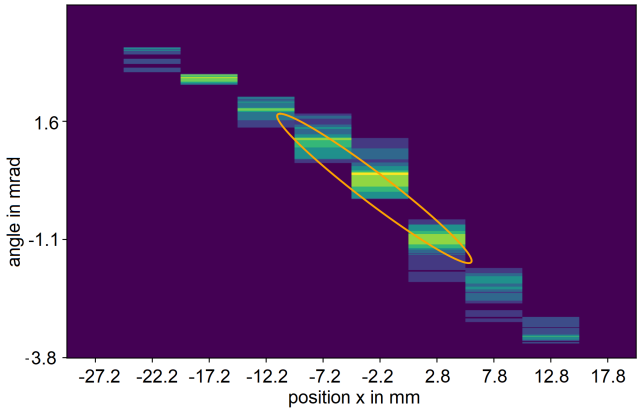

Figure 5.14: Phase space diagram of the collimated beam: The emittance is fitted based on a 1σ ellipse [Leonhardt, 2019].

5.3 Rotation in longitudinal phase space

As the next step, the collimated beam is injected into an rf cavity to enable the rotation in longitudinal phase space. Due to the geometric design of the rf cavity, the central energy of the LIGHT beamline is 8 MeV/u. The central energy, around which the rotation takes place, is set by is chosen by the injection time. If the rf amplitude and the rf phase is chosen right the rotation in longitudinal phase space can lead to an energy compression or phase focusing of the beam. The distance between the source and the rf cavity was chosen based on the *TraceWin* simulation in that way, that a high proton number is injected.

In this context, one central goal of each experimental campaign is to find the optimal setting of the cavity to achieve reproducibly shortest proton bunch durations. The cavity parameter, rf phase, has to be adujsted each beamtime. After the right rf injection phase is found the rf amplitude is optimized for the desired application.

This section starts with the measurement of the energy compression. Afterwards, temporal diagnostic systems are described. Finally, the study of the temporal focus is presented.

5.3.1 Energy compression

The energy compression was intensively studied in the previous work by S. Busold [Busold, 2014]. For the determination of the energy spectrum, he realized a dipole spectrometer, which is based on the dispersion of charged particles in a homogeneous magnetic

field. The spectrometer consisted of an entrance pinhole, three identical permanent magnets and an RCF stack. He observed the energy compression, which possessed a Gaussian-like distribution, and demonstrated a reduction in energy spread from (18 ± 3)% to (2.7 ± 1.7)% (FWHM) around a central energy of $E_0 = (9.7 \pm 0.1)$ MeV.

In this work, the energy compression was measured only qualitatively for verification processes with an RCF stack, which consisted of an aluminium foil and four EBT3 layers (corresponding Bragg energies: 3.7 MeV, 6.5 MeV, 8.5 MeV, and 10.2 MeV). The proton beam was injected into the rf cavity at an relative rf phase close to $\Phi_s = -90°$ and an rf amplitude of 4 V. The obtained energy spectrum is shown in figure 5.15. Inside the central energy interval of (8.65 ± 0.25) MeV an absolute number of $(0.65 \pm 0.35) \times 10^8$ protons is found. For a better resolution, which enables to recognize the Gaussian shape of the beam profile, it is recommendable to use an RCF configuration with a higher resolution, e.g. consisting of EBT3/2 films, or to use the mentioned dipole spectrometer.

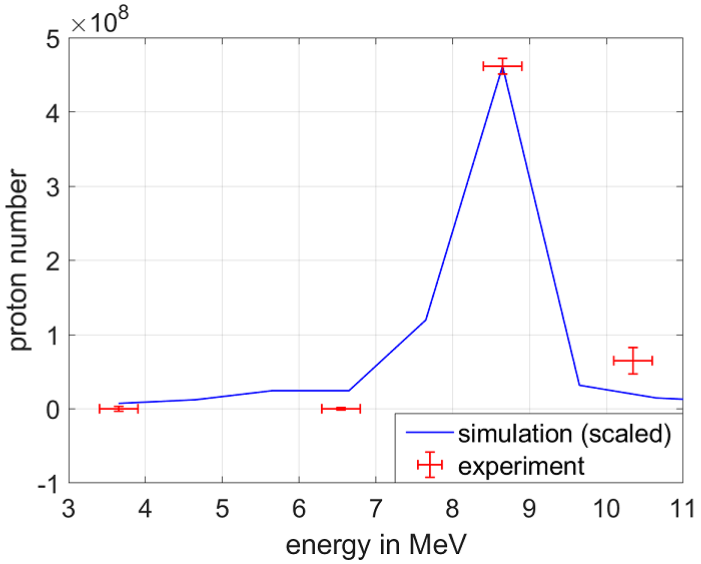

Figure 5.15: Energy compression of the proton beam: the measured proton numbers in each RCF layer are plotted in red. The scaled simulation is shown in blue.

5.3.2 Phase focusing

The phase focusing using the rf cavity was studied by investigating the influence on the proton bunch duration of the rf parameters. A detailed study took place in November 2014 [Busold et al., 2015]. In this context, fast time-of-flight diagnostics are necessary to measure the temporal profile of the ion bunch and enable a fast analysis to be able to set the cavity parameters for the next shot.

Two detection systems for the measurement of the temporal profile were used complementarily: a scintillator combined with a streak camera and a membrane diamond detector. The diagnostics were positioned in the Z4 target chamber. These two diagnostics will be described in the following, starting with the scintillator system.

Scintillators are often used as particle counters to measure fluxes [Forck, 2015, Strehl, 2006]. When a particle hits and penetrates a scintillating material, it collides with the target electrons (electronic energy loss) leading to the creation of fluorescence photons. The fluorescent signal is detected and amplified with an appropriate detector system, e.g. photo multiplier or a streak camera. The ideal scintillator should have a fast fluorescence decay. Moreover, it should be radiation-hard so it will not be destroyed by the particle beam. The light output should be linear to the energy loss and the wavelength of the light should be within the absorption range of the detection system. Typically, plastic scintillators are used as they are cheap and easy to produce. Their decay time is in the range of ns.
For the phase focusing measurement, the plastic scintillator BC-442Q [Ceramics and Crystals, 2016] was utilized. This scintillator has a decay time of 0.7 ns and emits the absorbed energy in form of light with a wavelength of 355 nm.

The produced light in the scintillator was captured with a streak camera [Hamamatsu, 2018a]. The streak camera transforms the temporal profile of the captured light into a spatial image. Figure 5.16 sketches its working principle. Light enters the optical system through a slit. It is converted inside a photocathode into an electron signal. Therefore, in the figure four optical pulses are converted sequentially into electrons. These electrons are accelerated in an applied electric field which is generated by a mesh.

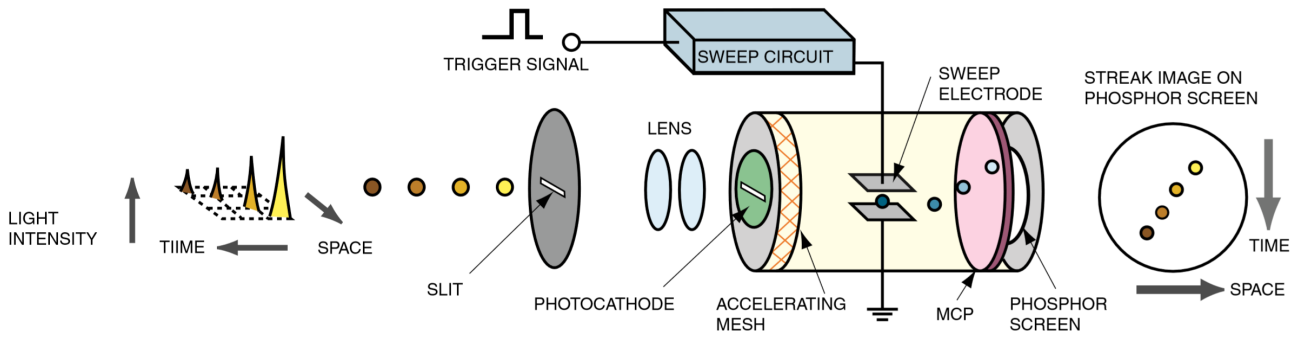

Figure 5.16: Design and operation of a streak camera [Hamamatsu, 2018a]. The incident light enters through a slit the camera system. It is converted into a two-dimensional image with spatial and time resolution.

Then the electrons pass a pair of sweep electrodes and arrive at slightly different times leading to a vertical deflection. The electron signal is multiplied by a multi-channel-plate (MCP). Finally, they hit a phosphor screen, where they are converted back to light and recorded with a camera.

In this experimental setup, the Hamamatsu streak camera C10910 [Hamamatsu, 2018b] images a 9 mm horizontal line-out at the center of the quadratic scintillator at 45°. Its time resolution is limited by the finite entrance width, in this case $\Delta\tau = 200$ ps. The streak time was 50 ns.

The combination of a scintillator with a streak camera enables to measure the temporal profile of ion bunches. This system is mainly limited by the decay time of 0.7 ns of the scintillator. As the *TraceWin* simulations predict a proton bunch duration of $\approx$ 70 ps at FWHM, a diagnostic with a better time resolution is necessary. Therefore, fast diamond detectors have been developed to measure the temporal profile of the ion bunch. The special demands on this detector are given by the LIGHT beam parameters. The detector has to measure proton energies in the MeV range and a good time resolution of $\approx$ 70 ps is required. Moreover, it must withstand high particle numbers of the order of 10^9 ions/bunch (10^7 ions/mm^2). To meet these requirements, a special diamond detector was constructed.

Diamond as a material combines radiation hardness and excellent electronic properties such as high charge carrier drift velocity, a wide band-gap, and a high break-down voltage. These properties make it an ideal tool as a particle detector in harsh environments [Berdermann et al., 2010a, Cayzac et al., 2013]. Hereby, artificially produced chemical vapour deposited (CVD) diamonds enable the definition of quality standards and scientific reproducibility. Two types of diamonds were fabricated: the crystallites of the diamond can have all the same orientation (single crystal, sc) or they are separated from each other via grain boundaries (polycristalline, pc).

Diamond detectors belong to the group of semiconductor detectors. They are mostly based on a parallel-plate geometry: two electrodes are sheathing the diamond. When a voltage is applied, the diamond forms a solid-state ionization chamber. The operating principle is shown in figure 5.17. An ionizing particle (X-rays, ion, electron) penetrates the diamond and generates electron-hole pairs through ionization processes. The charge carriers are thermalized in the order of picoseconds and drift to the electrodes leading to an image charge according to the applied field geometry. The generated compensating current in the external circuit is recorded with a digital oscilloscope.

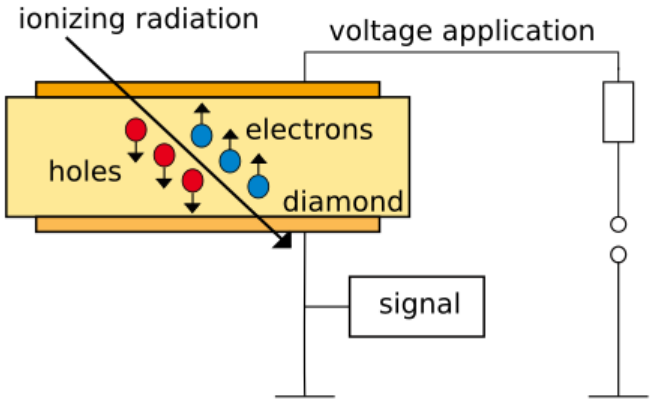

Figure 5.17: Working principle of a diamond detector: the metallized diamond is in parallel plate geometry with an applied electric field. Ionizing radiation hits the diamond detector and generates electron-hole pairs. The generated charge carriers are pulled towards the electrodes and generate a signal which is passed to the oscilloscope.

Diamond possesses the highest charge carrier mobility (holes: 1800 cm^2/Vs, electrons: 2300 cm^2/Vs) among semiconductors (silicon: holes: 480 cm^2/Vs, electrons: 1350 cm^2/Vs) and its electrical resistivity enables the application of fields up to several V/µm leading to high charge carrier velocities [Pomorski, 2008, Canali et al., 1975]. Its low capacity C= $\epsilon_0 \epsilon_R A/d$ depends on its specific dielectric constant ϵ_R, the detection area A, and the thickness of the diamond d. The individual time properties τ = RC depend on the capacity of the diamond sample and the resistance R of the electronic design. In the following, the design of the specifically developed diamond detector is described.

The thickness of the diamond is significant for the charge carrier transport through the diamond. The sample is an etched single crystal (sc) diamond membrane in parallel plate geometry with a capacity C = (1.397 ± 0.032) pF. A chosen detection area of 0.5 cm diameter is metallized with a gold-chrome coating. It has a thickness of (6 ± 1) µm. Figure 5.18 a) shows a photograph of the membrane after the lithography process. Due to the membrane construction, voltages up to ± 50 V can be applied and confirm the high breakdown field of E(BD)> 8 V/µm [Berdermann et al., 2010b]. The left figure 5.18 shows a photograph of the membrane after the lithography process. The transparent diamond is shown. The edge of the scCVD diamond is the oblique line cutting on the right side. In the center of the thin circular membrane the structured monolithic electrodes are connected to the bonding pads. The anode is on the back side (left) and the cathode is on the top side (right). Both electrodes overlap in a circle, which is the active detection area with a 0.5 mm diameter. The dots on the picture are defects or irregularities in its surface. Inside the membrane, less defects and irregularities are present.

The electronic design is constructed on a ROGERS R4350 radiation-resistant ceramic printed circuit board (PCB) with the software EAGLE and adapted to its use in the radio-frequency region [Rogers corporation, 2017, CadSoft, 2016]. The circuit design is based on two major parts: the bias supply and the output signal processing.
On the bias supply side (left side in figure 5.18), two low-pass filters increase the signal-to-noise ratio of the detector and five capacitors with a total capacity of 444 nF are built-in to provide a fast re-supply of charge carriers for the large bunch signal of up to 20 nC. The bias supply is soldered to the rear side of the metallized diamond and it is protected by the aluminium front plate of its housing.
On the signal processing side (right side in figure 5.18), the diamond is connected via bonding wires to the PCB and the signal is transferred through an unbalanced attenuator network, called T attenuator, to the digital oscilloscope. While the oscilloscope works on a 50 Ω basis, the inner resistance of the detector is reduced to enable a better time resolution $\tau = RC$. To match these resistances, the T attenuator is necessary.

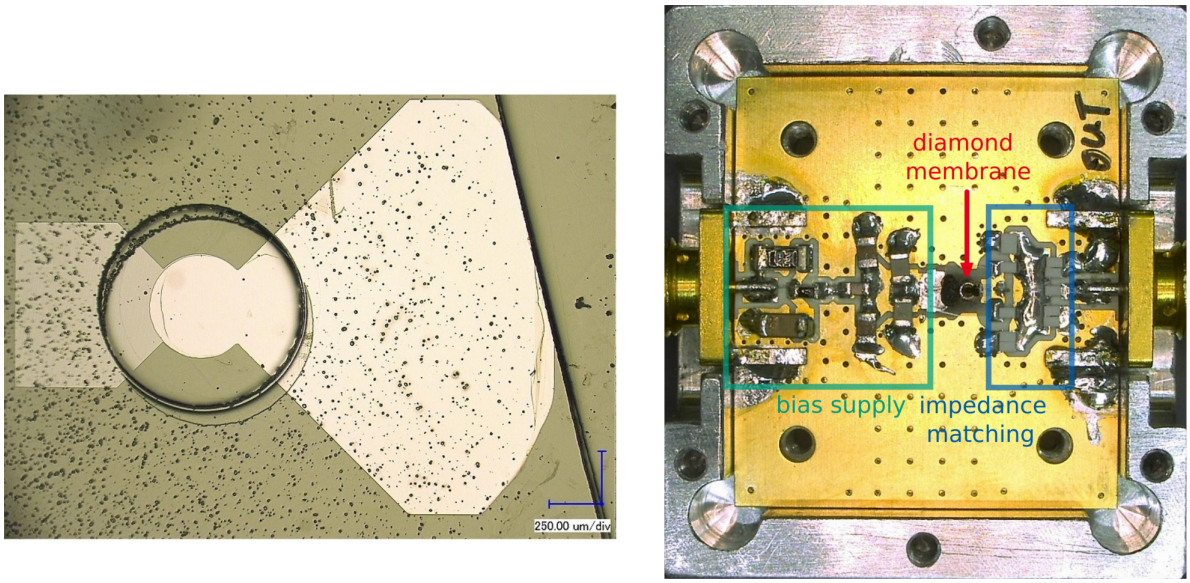

(a) photograph of the membrane (b) photograph of the design

Figure 5.18: Two photographs of the detector [Jahn, 2015]. a) Photograph of the membrane after the litography process (courtesy of Michael Träger). The edge of the scCVD diamond is the oblique line cutting on the right side. In the center of the thin circular membrane the structured monolithic electrodes are connected to the bonding pads. b) Photograph of the diamond detector. The diamond membrane is attached in the center of the PCB. From the left side, charge carriers are provided by the bias supply. On the right, the signal processing attuates the signal intensity.

The T attenuator consists of three non-inductive resistive elements used to match between two different impedances. The designed impedance matching has an output resistance $R_{out} = 49.9\,\Omega$, a shunt resistance $R_{shunt} = 1.25\,\Omega$ and an input resistance $R_{in} = 5\,\Omega$ leading

to an inner resistance of the detector $R_{inner} = 5.3\,\Omega$. The impedance matching to 50 Ω output resistance is necessary to transport the signal to the oscilloscope with a standard 50 Ω entrance. Similarly, this resistive design attenuates the signal amplitude by 14 dB leading to signals below the necessary 5 V, which are extracted to the oscilloscope. Combining the sample parameters and the electronic design, the time constant $\tau = RC$ has a value of 68 ps for a load of 50 Ω. Taking the T attenuator into account, the detector load is 6.25 Ω reducing the time constant to 8.73 ps. As a result, the time constant is significantly reduced and the signal is attenuated.

Due to the impedance matching causing the 14 dB attenuation, it was not possible to characterize this detector with a single particle measurement, which is the typically used method. Hence, a fast signal in the femtosecond regime with sufficient energy was required to demonstrate the time resolution capability of the detector. Therefore, its response was investigated under short pulse laser irradiation ($\lambda = 1053$ nm, $\tau = 350$ fs, $I = 10^8$ W/cm^2, E = 5 mJ) which excited the intrinsic charge carriers [Foulon et al., 1996]. The response of the detector to photons reflects the change in conductivity because of the freed charge carriers in the diamond. When a constant electric field is applied, the measured output signal voltage is proportional to $(n\,\mu_n + p\,\mu_p)\,V_{bias}$ with the bias voltage V_{bias}, the electron and hole densities n and p, and their mobilities μ_n and μ_p [Foulon et al., 1996]. Therefore, increasing the laser energy leads to an increase of the signal amplitude. If the laser energy is too high, a plasma was generated at the surface and destroyed the detector's electrodes.

As diamond has a band gap of 5.48 eV, a laser pulse wavelength of 226 nm would be necessary for the excitation. Due to defect centers between the conduction and valence band, which result from impurities in the diamond, it is possible to excite extrinsically with longer wavelengths, e.g. produced by the PHELIX laser.

The generated photocurrent by the direct laser irradiation and its decay were recorded and analyzed by a fast oscilloscope with a bandwidth of 8 GHz and a 25 GHz sampling rate. Therefore, the diamond detector was connected using short high-frequency compatible SubMiniature version A (SMA) cables to the oscilloscope. A voltage of 30 V was applied across its membrane leading to an electric field gradient of 2.3 V/μm.
Typical signal intensities in the millivolt regime were measured. The detector response time of the membrane is t(FWHM) = (113 ± 11) ps. Another similar detector with the same electronic design, but a 20 μm pcCVD diamond was realized and also tested. It shows a response time of t(FWHM) = (172 ± 5) ps. Both responses are shown in figure 5.19.

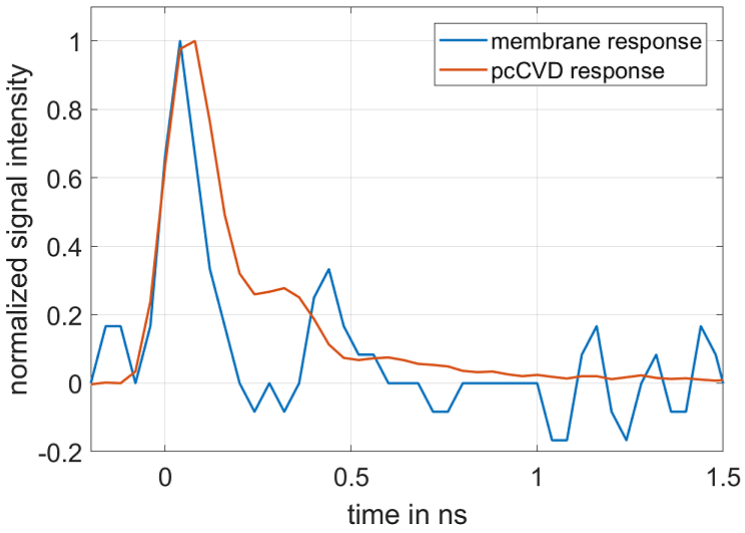

Figure 5.19: Response functions of the pcCVD and the scCVD membrane detector are shown. While the pcCVD response has a FWHM of (172 ± 5) ps, the membrane detector has a response with (113 ± 11) ps at FWHM.

The membrane detector displays an overshoot behaviour resulting in an oscillation. This can be explained by the radio-frequency design, which has incorporated resistors not suitable for radiofrequencies and lead to an inductance of the board. Further details on the pcCVD diamond plate, the scCVD diamond membrane and the detector design can be found in [Jahn, 2015].

Using the diamond membrane detector with the described settings enables to measure ion bunch durations of $t \geq 200\,\text{ps}$. The response times of the described diamond detectors are sufficient to measure the temporal profiles of the ion bunches which are generated and temporally compressed in the LIGHT beamline research project. Therefore, they enabled the adjustment of the rf injection phase and the rf amplitude which is described in the next section.

Measurement of temporally short proton bunches

For a better understanding of the rf cavity adjustment, a detailed study of phase focusing was performed in November 2014 and will be described in the following.

After the transit through the rf cavity, the incoming proton bunch drifted through the beamline and finally hit the scintillator, which was positioned at 6 m distance from the source and read out by the streak camera. A hole of 1.5 mm diameter was cut out in the center of the scintillator, so that one part of the bunch passed through this hole and was measured by the diamond detector located 60 mm behind it. The study was performed with the prototype 13 µm pcCVD diamond detector and consisted of three experimental parts: a reference measurement, the influence of the rf phase and the influence of the rf amplitude on the temporal beam profile.

First, a reference shot was recorded without an applied voltage to the rf cavity. Considering the measured energy spread of the collimated beam of $\Delta E/E_0 = (21 \pm 3)\%$ at a central energy of 7.8 MeV [Busold, 2014], the corresponding time-of-flight has an expected value of (12 ± 2) ns after 6 m distance from the source. Furthermore, the *TraceWin* simulation predicts a pulse length of (8 ± 1) ns and an energy spread of 9%.

Figure 5.20 presents the temporal profile of the reference shot, measured with both diagnostic systems. A clear double peak structure is visible. A possible explanation might be that this structure results from the solenoid aperture or from two quadrupole doublets, which were used behind the rf cavity in the beamline setup within the beamtime in November 2014 [Busold, 2014]. The measurement with the diamond detector shows a proton distribution of (6 ± 2) ns and the streak camera measured a duration of (8 ± 2) ns. The cause of the lower bunch duration in the diamond measurement, is the higher signal threshold due the detector's attenuation. The measured bunch durations are in agreement to the *TraceWin* prediction, but they are lower than the calculation based on the measured energy spread after beam collimation.

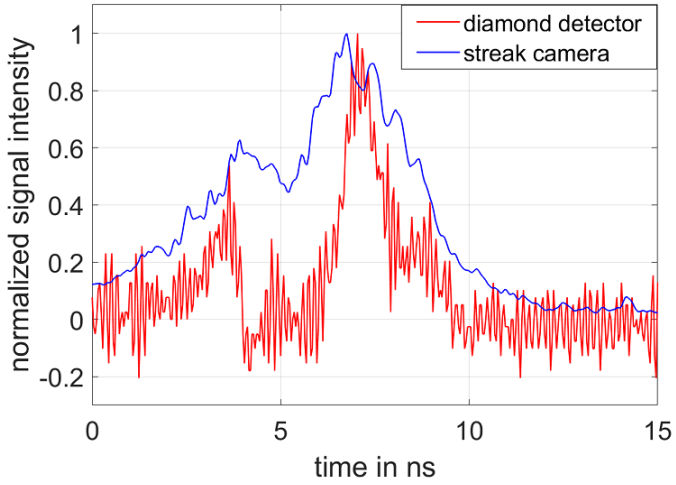

Figure 5.20: Temporal profile of reference measurement (no electric voltage is applied to the rf cavity) [Jahn, 2015]. The diamond detector (red) measured a proton bunch duration of (6 ± 2) ns and the streak camera (blue) recorded a duration of (8 ± 2) ns.

Second, the injection phase ϕ_s of the beam was scanned. The goal was to adjust the relative rf phase so that the time delay between PHELIX and the rf phase resulted in a proton injection around 8 MeV at a synchronous phase $\Phi_s, = -90°$. As there is no exact calibration of the synchronous phase, a relative phase Φ has to be adjusted. This is done by scanning the phase. In doing so, the precision is limited to 0.3 ns, i.e. 12°, due to a jitter in the timing system. The phase is measured on-shot with an uncertainty $\Delta\Phi = 2°$. The normalized rf amplitude $U_{rf,norm}$ was set to 4 V according to the *TraceWin* simulations.

Figure 5.21 presents a typical series of temporal profiles depending on the relative rf phase Φ, which are measured with the diamond membrane detector and the streak camera. shot 46

shows a successful injection of the proton bunch. In the next shot 52, a decrease in the relative phase leads to a double peak structure. This means the bunch pulled apart. Therefore, the phase value of shot 46 is increased in the next shot 53, which has a shorter bunch duration. The shorter the bunch duration, the nearer is the chosen relative phase to the synchronous phase $\Phi_s = -90°$. Both detection systems are consistent in their response behaviour and show comparable temporal profiles, which vary due to their characteristic response functions. The diamond detector shows the typical overshooting behaviour due to the electronic design.

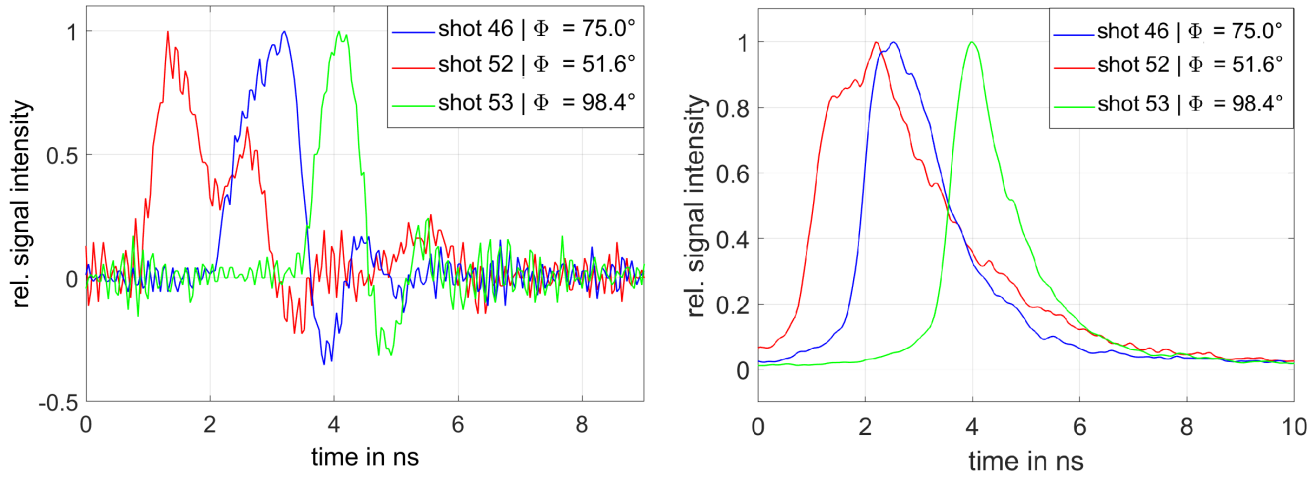

Figure 5.21: Proton bunch duration in dependence on the rf phase [Jahn, 2015]. The temporal profiles at different relative rf phases are shown. Left: measurements with the diamond membrane detector are presented. Right: measurements with the streak camera are shown.

Third, the rf amplitude was varied for the chosen fixed phase (resulting from the phase scan) to find the best temporal focus for the given distance. The goal was to find the optimal normalized rf amplitude $U_{rf,norm}$ for the achievable minimum bunch length. The dependency of the bunch duration on the rf amplitude is shown in the left figure 5.22. The minimal proton bunch duration was measured as (468 ± 40) ps (FWHM) with the diamond detector at $U_{rf,norm} = 4.3$ V. At a lower applied voltage, the temporal focus is at a more distant position. Likewise the temporal focus for higher voltages is achieved earlier than this position. The measured temporal profile of the achieved minimal proton bunch duration is shown in the right figure 5.22. The FWHM of the measured signal is (468 ± 40) ps. Based on the characteristic response function of the pcCVD detector, the signal was deconvoluted with a specially developed algorithm. A detailled description of the algorithm can be found in [Jahn, 2015]. The deconvoluted signal has a bunch duration of (462 ± 121) ps (FWHM). This setup was used for a detailed study of time-compressed proton bunches and for the confirmation of the functionality of the pcCVD diamond detector. In the following beamtimes, the faster membrane diamond detector became the main and only detector, as a second high-field solenoid was positioned inside the Z4 cham-

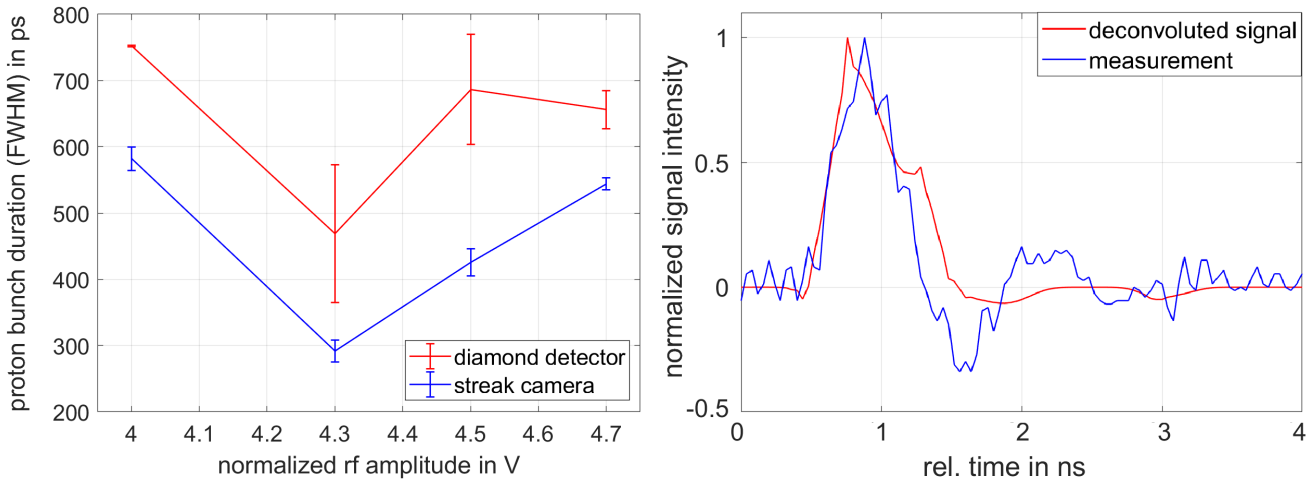

Figure 5.22: RF phase scan [Jahn, 2015, Busold et al., 2015]. Left: the proton bunch duration at FWHM is dependent on the gap voltage. The minimum bunch duration of (468 ± 40) ps (FWHM) was achieved for a gap voltage of $U_{rf,norm}$ = 4.3 V. Right: the temporal profile was measured with the pcCVD diamond detector (blue). Its deconvoluted (red) signal is also illustrated.

ber and the scintillator-camera assembly could not be established due to missing space capacity. The membrane diamond detector was positioned ≈ 6.4 m from the source.

One of the goals of this thesis is the demonstration of the reproducibility of the temporal focus. Proton bunch durations below 600 ps were reproduced in four experimental beamtimes with slightly varying beamline setups. The left figure 5.23 shows the achieved shortest proton bunch profiles for the beamtimes 2015, 2016, and 2017.

Based on the current existing setup, which is described in chapter 4 and will be used in future, a minimal bunch duration was measured as $\tau = (593 \pm 40)$ ps at FWHM at an rf amplitude of 6.35 V. The signal is deconvoluted based on the response function of the detector resulting in a bunch duration $\tau = (468 \pm 40)$ ps at FWHM. The measured temporal profile and its deconvolution are shown in the right figure 5.23.

Table 5.1 gives an overview of the measured and deconvoluted proton bunch durations in the different beamtimes. The shortest proton bunch duration was recorded in October 2015 as (235 ± 40) ps (FWHM) and it is the closest value to the *TraceWin* simulation prediction of ≈ 70 ps (FWHM). The uncertainties of the measurements are given by the temporal resolution of the oscilloscope, which is $\Delta t = 40$ ps. The uncertainties of the deconvolutions are determined through the deconvolution of the reconvolved signal.

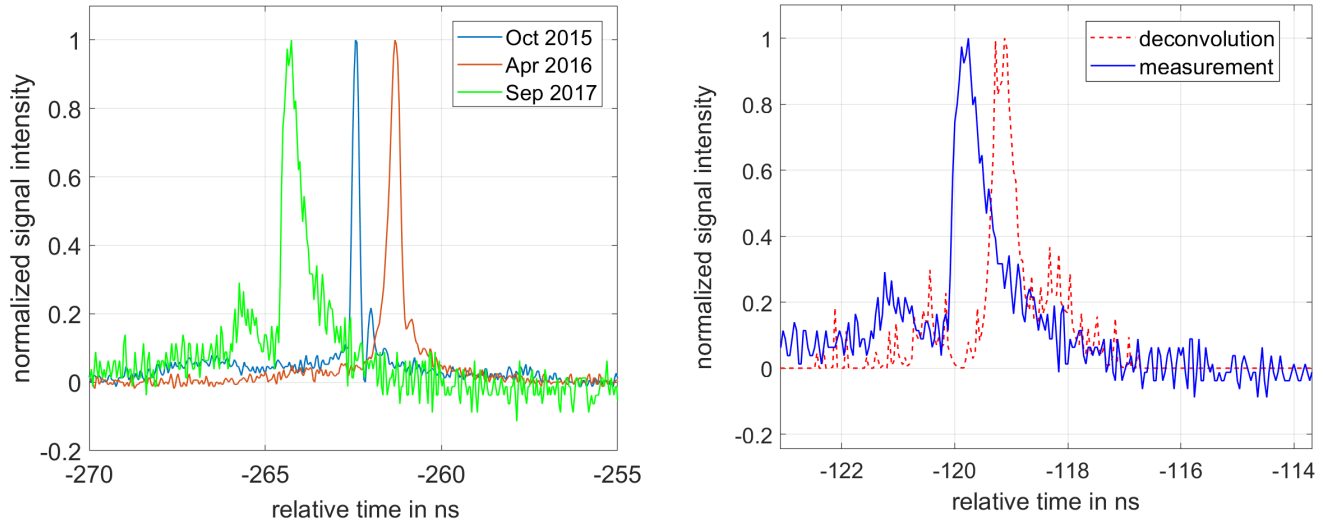

Figure 5.23: Temporal profiles of achieved shortest proton bunch durations. Left: the temporal profiles for the beamtimes in 2015, 2016, and 2017 are shown. Right: temporal profile of shortest proton bunch duration. A fast membrane diamond detector measures a bunch duration of τ = (593 $\pm$ 40) ps at FWHM (blue). The signal is deconvoluted using the detector's response function (red) leading to a bunch duration of τ = (468 $\pm$ 40) ps at FWHM.

Table 5.1: Temporal bunch durations measured in the different beamtimes.

beamtime	measurement (FWHM) in ps	deconvolution (FWHM) in ps
November 2014	468 $\pm$ 40	462 $\pm$ 121
October 2015	235 $\pm$ 40	209 $\pm$ 16
April 2016	375 $\pm$ 40	368 $\pm$ 62
September 2017	593 $\pm$ 40	458 $\pm$ 183

5.4 Final focusing system

In order to achieve the necessary proton intensities for applications, the crucial goal is to transversely focus the beam to a small spot size at the interaction point for applications. The characterization of the final beam parameters of the laser-driven proton beamline with its focusing capabilities enables the planning of advanced experiments.
The final focusing stage is the second solenoid. Through choosing the appropiate setting of its magnetic field strength, a chosen energy interval is focused in a certain distance. The achieved focusing parameters were measured in the beamtime September 2017 and are presented in this section.

As described in previous sections, the laser-driven protons were captured by the first solenoid operated at 6.9 T. The collimated beam was transported to the Z4 target chamber. The rf cavity was not available for this shot due to technical difficulties. Hence, the energy spread, which was generated by the first solenoid, was transported to the second target chamber. The second solenoid was operated at 5.6 T (according the simulation conversion factor) and focused the beam on an RCF stack, which was positioned 10 cm behind the solenoid, as this position is the interaction point for applications. At this position, the distance from the source was 5.95 m. The RCF stack consisted of two EBT3 layers, followed by two HD-V2 layers and closing with two EBT3 layers (corresponding Bragg energies: 3.7 MeV, 6.5 MeV, 7.5 MeV, 8.3 MeV, 9.8 MeV, and 11.3 MeV).

The recieved color-coded RCF film layers are shown in figure 5.24. The transverse beam profile is round-shaped. The beam diameter on the RCF films becomes smaller until the beam reaches the fifth RCF film. Subsequently, the diameter increases again in the following RCF film. This means that the focus is located in the fifth RCF film and it has a circular shape. According to the proton energy deposition in the RCF stack, the minimal focus was achieved in the energy interval of (9.55 ± 0.25) MeV.

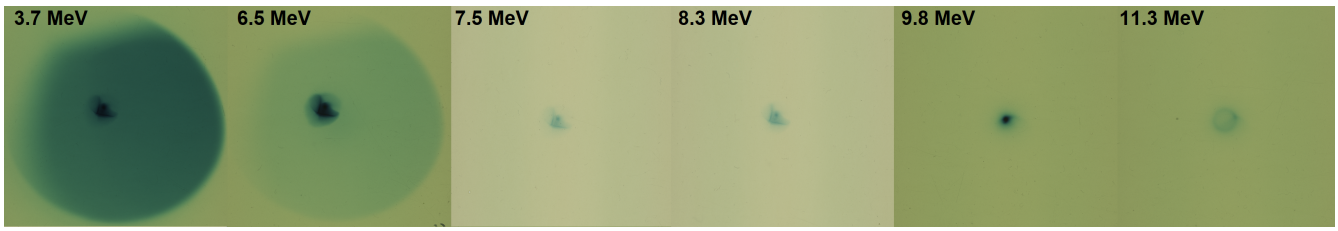

Figure 5.24: The RCF stack was positioned 10 cm behind the second high-field solenoid. The third and fourth RCF layers are type *HD-V2*, the others are type *EBT3*. With the increasing layer number, the beam is collimated up until the fifth RCF layer (Bragg energy: 9.8 MeV), in which the minimal focus is detected. For each RCF layer, the Bragg peak energy is written in black.

On the first two layers, a strong background from γ rays is observed.

For the analysis, the calculated energy deposition and response function of this used specified RCF stack are shown in the left figure 5.25. Based on this information, the measured energy spectrum is determined using the algorithm described in section 5.1.1. The reconstruction of the energy spectrum of the proton beam demonstrates the beam collimation and transport. The recieved energy spectrum is depicted in figure 5.25. The beam is collimated at the central energy of (8.45 ± 0.25) MeV and contains (2.8 ± 0.3)· 10^8 protons at this energy. The total spectrum has (3.7 ± 0.5)· 10^8 protons. The energy spread of the proton bunch is ΔE =0.82 MeV, which corresponds to $\Delta E/E_0$ = 9.7%.

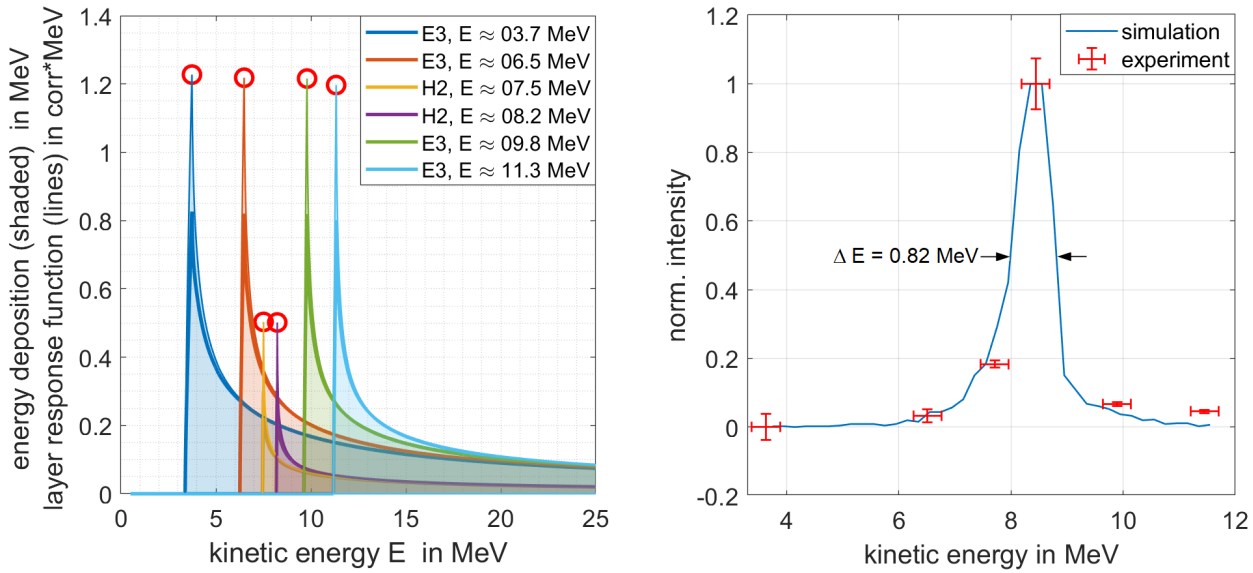

Figure 5.25: Left: Energy deposition and RCF response of protons in the active layers of the designed stack configuration for the measurement of the minimal focus. Right: simulated and measured normalized spectrum of the collimated beam. For each RCF layer, the stopped absolute particle number within this layer is shown (red). For comparison, the *TraceWin* simulation results are displayed (blue).

Figure 5.26 presents the measured transverse beam profile, which was reconstructed from the fifth RCF film. The beam is transversely focused at the energy of (9.45 ± 0.25) MeV. The focal size is determined as 1.1 mm x 1.2 mm at FWHM. The focus consists of 2.5 x 10^7 protons within the energy interval of (9.55 ± 0.25) MeV. The low proton number in this energy interval is reasoned by the settings of the solenoids: while the first solenoid collimated the beam at a central energy of (8.45 ± 0.25) MeV, the second solenoid focused an energy interval of (9.55 ± 0.25) MeV. Through lowering the magnetic field strength of the second solenoid, it is possible to focus the beam at the same energy as the collimating one. An adaptation of the solenoid to the central energy was not possible due to beamtime limitations.

The *TraceWin* transport simulations verify the dependency between the the magnetic field of the solenoid and the focal spot size as well as the focal spot distance. The focal spot size is predicted to be 0.6 mm x 0.6 mm at FWHM and the simulated beam profile has been shown in figure 4.8 (compare section 4.5).

The discrepancy between the simulation and measurement has two main reasons. First, the structure of the RCF stack consists of active and inactive layers. If the real minimal focus is located in an inactive layer, it it not resolved, as the RCF diagnostic only measures the energy deposition in the active layers. Therefore, it would be useful to arrange the RCF stack in such a way that the central energy is displayed, or to use an RCF stack of only active layers which are currently not available by the producer. Second, the focal spot size is only limited by the beam emittance and not effected by space-charge effects. In this experimental campaign, the emittance of the beam was not sufficient (overlapping beamlets) due to the solenoid alignment and has to be improved in the future (see subsection 5.2). This contributes to a larger beam spot compared to the simulation. Moreover, the simulation is based on the paraxial approximation (see equation 3.24) for a ideal magnetic field. For a more realistic prediction, spherical aberrations have to be taken into account, which occur due to a more realistic magnetic field distribution [Kroll, 2018].

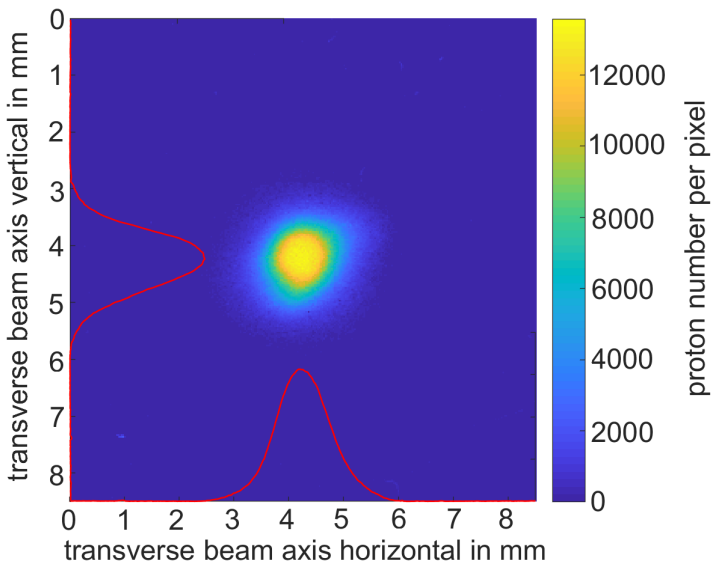

Figure 5.26: Transverse proton beam profile: the smallest focus of the proton beam was measured on the fifth RCF film with the energy interval of (9.55 ± 0.25) MeV. The focal spot size is 1.1 mm x 1.2 mm at FWHM.

In future, the second solenoid and the rf cavity will be operated at the same time. This will enable the achievement of highest proton intensities. Depending on the demand, energy- or time-compressed proton bunches will be generated through the setting of the rf cavity. Assuming the measured proton bunch duration of (458 ± 40) ps, a beam current of 7.8 x 10^8 protons/ns ≈ 124 mA can be generated. This equals 5.8 x 10^{19} protons/(s·cm^2) or a beam intensity of 7.42 x 10^7 W/cm^2.

6 First application studies with the LIGHT beamline: proton imaging

The previous chapter has presented the achievable final beam parameters at the interaction point for applications. This chapter deals with the first performed application: proton imaging of a solid object. It starts with a short description on proton matter interaction based on the works by [Endres, 2018, Lang, 2014, Cookson, 1974]. An important parameter for proton imaging is the beam homogeneity, which is characterized. Finally, the design of the imaging sample will be described and the proton imaging study will be shown.

6.1 Proton matter interaction

If a proton passes a material with a certain thickness, three interaction processes with the material can occur: the interaction of the proton with the shell electrons (energy loss), the strong nuclear interaction with the nucleus (nuclear scattering), and the Coulomb interaction with the nucleus. Figure 6.1 shows these three types. These interactions never appear alone, but always in combination.

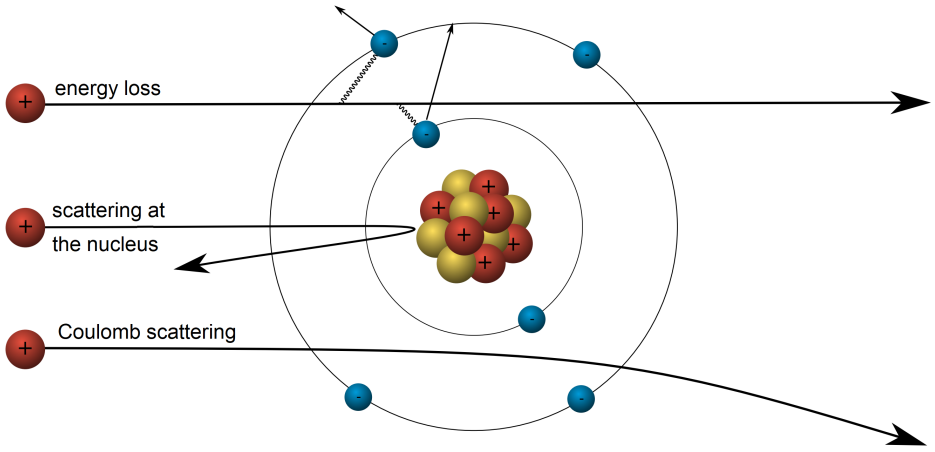

Figure 6.1: Three processes determine the interaction of a proton with a single atom [Endres, 2018]. The proton is inelastically scattered with the shell electrons (energy loss). Second, the proton is scattered at the nucleus due to the strong nuclear force (scattering at the nucleus). Third, it is deflected in the field of the positive nucleus (Coulomb interaction).

Based on these interaction processes, it it possible to perform proton radiography to reveal the interior of an object: the protons pass through the object and are detected by an imaging

diagnostic to retrieve an image. Compared to the well-established X-ray technique, protons penetrate materials more efficiently and therefore they are useful tools for e.g. medical applications [Prall et al., 2016] or investigations of high density materials with a high resolution [Varentsov et al., 2015]. Therefore,one of the interaction processes can be used for contrast generation of the image. The other effects influence the image quality in a negative way. In the following, the three interactions will be described.

The energy loss describes the process of slowing down and stopping of particles in matter. The protons are scattered inelastically by the shell electrons and excite these to higher energy levels or separate them from the atom. The energy loss value can be calculated with the Bethe-Bloch formula [Bethe, 1930]:

$$-\left(\frac{dE}{dx}\right) = \frac{Z^2 e^4 n_e}{4\pi\epsilon_0^2 v^2 m_e}\left(ln\left(\frac{2m_e v^2}{E_B}\right) - ln(1-\beta) - \beta^2\right) \tag{6.1}$$

with particle energy E, velocity v, atomic number Z, electron mass m_e, electron density of stopping material n_e, and mean ionisation energy E_B. The stopping power range can be determined by integrating this formula. As a result, the energy loss is especially dependent on density and thickness of the material.
For the use in imaging applications, the proton energy has to be measured, before and after the particle interacts with the material. The imaging contrast is generated by the energy measurement. This will be relevant for the imaging study using the LIGHT beamline.

The interaction between a proton and a nucleus is a special case of Rutherford scattering, which describes in general the elastic scattering of charged particles on a charge center by the Coloumb interaction. The differential cross section $d\sigma/d\Omega$ is dependent on the scattering angle θ in a center-of-mass system:

$$\frac{d\sigma}{d\Omega} = \left(\frac{1}{4\pi\epsilon_0}\frac{Z_1 Z_2 e^2}{4E_0}\right)^2 \frac{1}{sin^4\left(\frac{\theta}{2}\right)} \tag{6.2}$$

with the particle energy E_0, the number of charges in the nucleus Z_1 and of the projectile Z_2. The Rutherford scattering is described as the sum of collisions between the proton and the nuclei in the material. This process has a low cross section so it can be mostly neglected for projectile energies above a few 100 eV/u.
Therefore, imaging studies require high-energetic protons to penetrate the dense or high Z materials. The imaging contrast is generated by the measured scattering angle. At GSI, the proton microscope Proton Radiography for FAIR (PRIOR) was realized to probe a dense plasma on a

nanosecond time scale operating with 4.5 GeV protons [Varentsov et al., 2015]. PRIOR can magnify samples up to a factor of 4.2 and penetrate materials up to 20 g/cm^2.

The third appearing process is the Multiple Coulomb Scattering of the incident protons. During the propagation through the material, the proton interacts with multiple nuclei and hence is scattered multiple times. The total scattering angle θ_0 is dependent on the material density and thickness. The dependency is empirically described by [Highland, 1975, Lynch and Dahl, 1991]

$$\theta_0 = \frac{13.6MeV}{\beta cp} Z \sqrt{x\rho/X_0}(1 + 0.038\ ln(x/X_0)) \tag{6.3}$$

with the incident proton velocity βc, its momentum p, its charge number Z, the material thickness x, the material mass density ρ and the characteristic radiation length X_0.

In this context, laser-based ion beams are a powerful technique for probing of fast-transient phenomena or also studying the properties of dense macroscopic objects [Roth et al., 2002]. Based on the exponentially decaying energy spectrum, the different proton energies enable to probe the phenomenon at different times, as the proton emission is instantaneous ($\sim$ 1 ps). This allows e.g. the probing of laser-driven shock waves [Mackinnon et al., 2006, Koenig et al., 2005] or electromagnetic field perturbations [Mackinnon et al., 2004].

The LIGHT beamline provides a collimated, energy-compressed beam with high proton numbers, which are excellent properties for time-resolved imaging of a solid object. Compared to other imaging experiments directly behind a laser-driven source, the bunch duration is of several nanoseconds and a well-characterized collimated beam is available. Slow protons are stopped inside the object, while faster protons propagate through the object and hit the detector. In this case, the contrast of the image can be generated by the energy loss of the protons, as most of them penetrate the object. Moreover, the protons leak out at different angles and positions due to their Coulomb scattering. A larger distance between object and detector leads to larger scattering angles, which are observed.
A necessary condition for imaging is a homogeneous beam profile. Therefore, the beam homogeneity is improved by changes in the beamline and characterized in the next section.

6.2 Improving the beam homogeneity

For the performance of imaging applications, a uniform proton beam with a defined, narrow energy-spread is necessary. At first, two parameters are defined to describe the homogeneity of the beam: the uniformity factor and the fill factor. Both parameters are typical, routinely used

methods to characterize laser beams and are now adapted on a particle beam in this work.

The first parameter is based on the mean value of the deposited energy: the beam uniformity U_η is defined as the normalized root mean square deviation of deposited energy density from its average value [DIN EN ISO 13694-2010, 2000]:

$$U_\eta = \frac{1}{E_\eta}\sqrt{\frac{1}{A_\eta}\int\int [E(x,y)-E_\eta]^2 dx\ dy} \tag{6.4}$$

with the local deposited energy density $E(x,y)$, the deposited average energy density E_η and the effective irridiation area A_η. In case of $U_\eta = 0$, the beam is completely uniform.

The fill factor (FF) as the second parameter is sensitive to small areas with high intensities ("hot spots") [Instruments, 2012, Eisenbarth, 2017]. In the beginning, a certain threshold level is subtracted from each local deposited energy density. In this thesis, the threshold is chosen as one percent of the arithmetic average. The FF is defined as the ratio between the beam volume and the volume of the enclosing cylinder with the height of the measured maximum. Figure 6.2 illustrates a beam profile in two dimensions and the corresponding areas for the FF calculation.

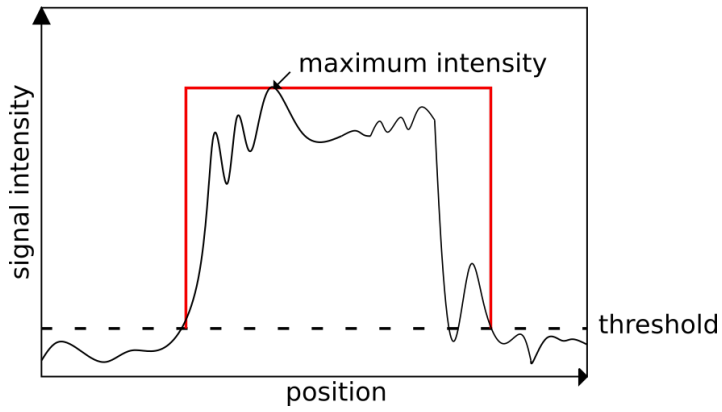

Figure 6.2: A two-dimensional representation of the relevant areas for the calculation of the FF: the FF is the ratio between the rectangular (red) and the area above the threshold (black). Adapted from [Eisenbarth, 2017].

The FF is calculated by dividing the area under the fit function by the area of the rectangle. The range of the FF is between 0 and 1. For a perfect top-hat with no peaks, its value is 1. An intense peak in the distribution increases the integral so that the ratio lowers.

For the LIGHT proton beam analysis, an RCF stack is placed 10 cm behind the second solenoid. The rf cavity is operated at an rf power of 4.1 V and a synchronous phase $\Phi_s = -90°$ to pro-

vide energy-compressed proton beams. The beam uniformity values are based on the third RCF layer with a stopping energy of 8.5 MeV, as this value is the central energy which is transported through the beamline.
Figure 6.3 a) shows the energy deposition in the relevant RCF film. The measured profile features a star-shaped, very intense and high-energetic spot. The round solenoid aperture is also observed on the film. Outside the aperture, no coloring of the film can be seen. The proton bunch includes 1.7 x 10^9 ± 9% protons and covers a circular area with a diameter of 4 cm, limited by the described solenoid aperture.
The analysis leads to a beam uniformity $U_\eta = 0.50$ and a FF = 0.23. Especially, the low value of the FF indicates the high intensity of the focal spot. This spot appears on the RCF stack behind the first solenoid with the previous design in every experiment and is transported as part of the profile to the second target chamber. S. Busold [Busold, 2014] has already observed this spot in his preceding work.

In the next step, a 1.25 µm thin mylar foil is used for beam straggling to reduce the filametation because of its neglegible energy-loss. The mylar foil is positioned in front of the rf cavity in the beam path. Figure 6.3 b) presents the transverse beam profile of the energy deposition in the third RCF film (the RCF stack has the same configuration). The energy deposition fills the solenoid aperture and has a higher average value per pixel compared to figure 6.3 a). Therefore, the average energy distribution is homogenized and is expressed by the beam uniformity value, which improved to the value of $U_\eta = 0.25$. The "hot spot" appears circular shaped and is very intense. Hence, the fill factor is getting worse and has a value of FF = 0.15 using the same analysing settings.

In the following experiment in September 2017, the first solenoid housing is replaced by the newest solenoid design which is shorter and more compact. This design has been described in section 4.3. This replace leads to a significant decrease in intensity of the star-shaped spot, which is still visible. The subfigure 6.3 c) presents the beam profile of the energy deposition. The average energy deposition is lower due to the damaged parabola coating, which led to lower laser intensities on the TNSA source and therefore reduced the proton numbers especially at higher proton energies (see section 5.1). For this reason, the analysis of the RCF film shows a uniformity of $U_\eta = 0.54$ and FF = 0.27. Compared to the previous experimental campaign without the new solenoid housing, the energy is more unevenly distributed, but the intensity of the "hot spot" is reduced.

In order to increase the beam homogeneity, the mylar straggling foil is positioned again in the beam path in front of the rf cavity. Figure 6.3 d) depicts the corresponding energy deposition. The "hot spot" is not visible and a clear edge of the solenoid aperture is observed. The

intensity of the measured energy deposition increases from left to right. The elimination of the described round-shaped "hot spot" effects the analysis: the beam uninformity improves to $U_\eta = 0.23$. Due to the increasing horizontal signal intensity, the fill factor has still a value of FF = 0.20. The bunch consists of 4 x 10^8 ± 30% protons.

For the understanding of the influence of both solenoid designs on the beam homogeneity, detailed investigations are necessary and are planned by the collaboration partner HZDR.

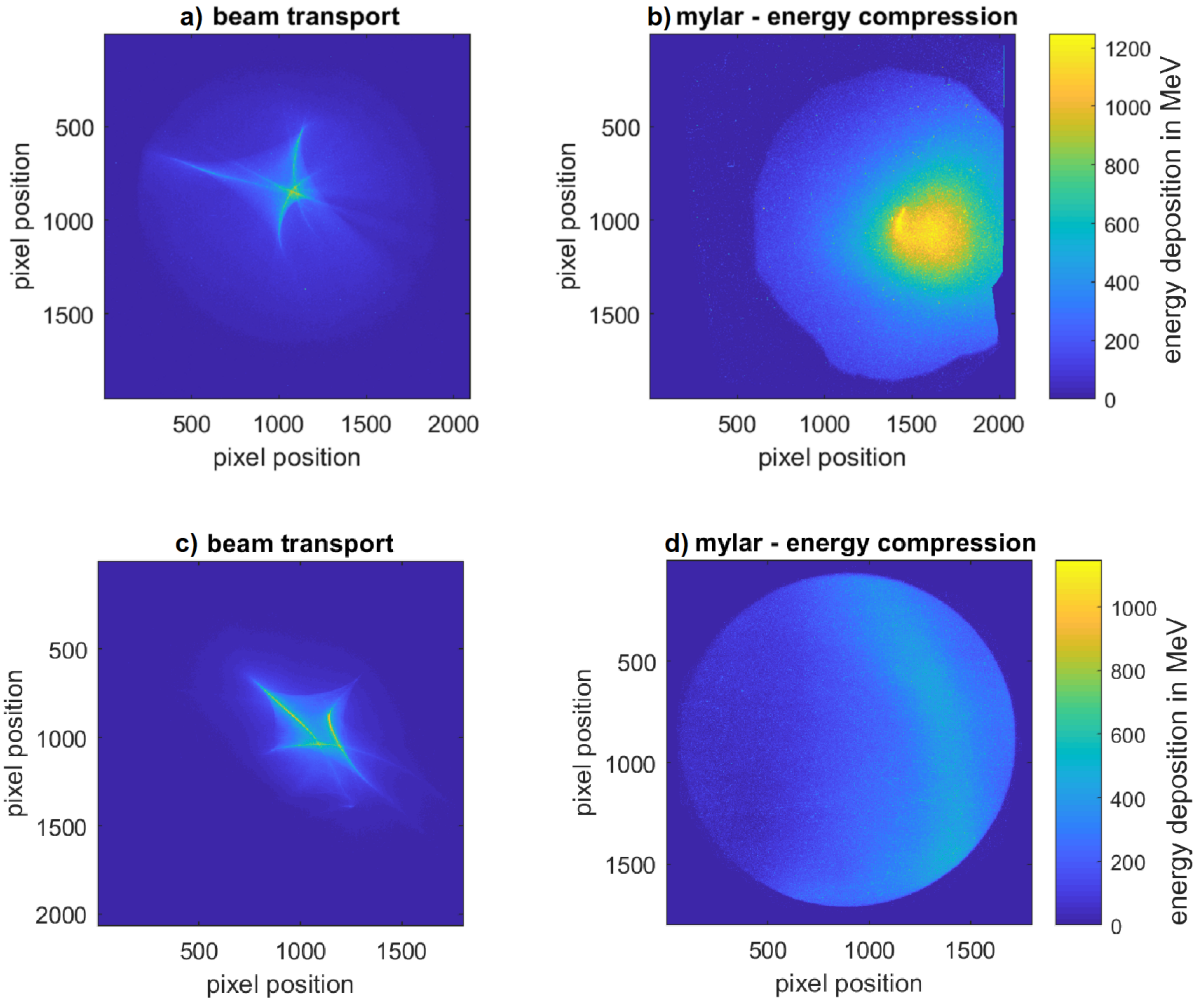

Figure 6.3: Comparison of beam profiles at the Bragg peak energy of 8.5 MeV between 2016 and 2017 at 6 m distance: a) beam profile in 2016, b) beam profile behind a mylar straggling foil in 2016, c) beam profile in 2017, d) beam profile behind a mylar straggling foil in 2017. For the beamtime in 2016, the solenoid design from [Busold, 2014] has been used. In 2017, the housing of the solenoid is replaced and the improved design (see section 4.3) is utilized.

6.3 Proton imaging of a solid object

For the proton imaging studies, a solid sample is placed inside the second target chamber. The energy-compressed proton beam, homogenized with the mylar straggling foil (see beam profile in figure 6.3 d)), is used for imaging. The proton beam passes the second pulsed high-field solenoid which has an aperture of 40 mm diameter and hits the sample.

The imaging sample is presented in figure 6.4. The figure shows that the letters of the name of the LIGHT collaboration form its design. Each letter has a different thickness. Therefore, six nickel foils are aligned in a stack configuration. In each foil a certain number of letters was cut out of the layer by a laser. The thicknesses increase from left to right in 20 µm steps and the i-dot is empty as a reference.

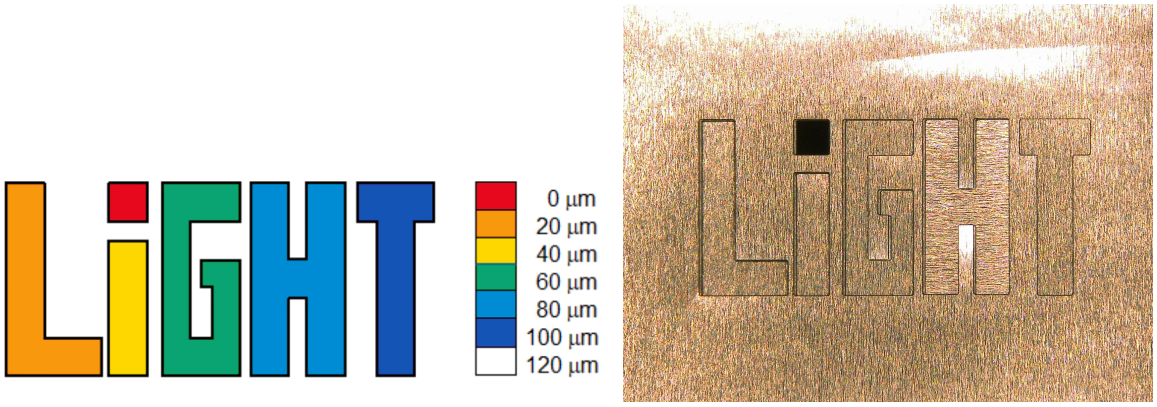

(a) design of the imaging target (b) microscopic photograph

Figure 6.4: Design of the imaging target: figure (a) presents the target design. The differently thick layers are coloured. Figure (b) presents a microscopic photograph.

The protons are detected with an RCF stack consisting of six layers of the modified type EBT3/2. The stack is positioned 6 mm behind the imaging object. Each modified EBT3/2 film consists of a 28 µm active layer and one 125 µm matte-surface polyester foil (compare figure 5.1) leading to an energy deposition shown in figure 6.5.
The analysis of the reference "i-dot", which is part of the imaging target, shows that a central energy interval of (9.1 ± 0.3) MeV is transported using the beamline settings through the beamline. Based on this value of 9.1 MeV, the energy loss for each target thickness is calculated with the *SRIM* energy loss tables. The black lines in the figure indicate, in which layer the proton beam is predicted to be stopped (dependent on the letter thickness). Figure 6.5 predicts that the reference energy ("i-dot") will be stopped in the sixth film. The part of the beam, which has to pass 20 µm nickel, will reach due to its energy loss the fifth letter. The biggest energy loss is expected behind the letters "G" and "H". In this case, both stopping energies are predicted to be located in the same RCF film.

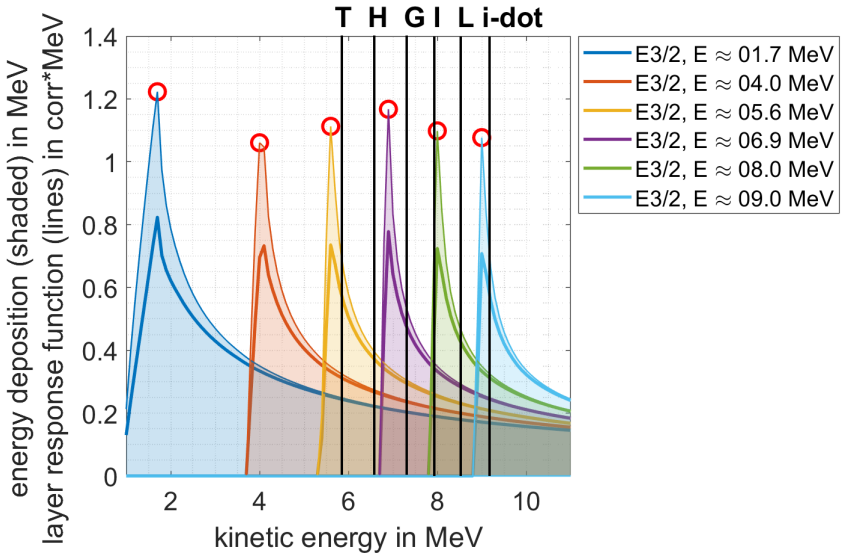

Figure 6.5: Energy deposition and RCF response of protons in active layers: for each RCF layer the energy, at which the protons are stopped at their Bragg peak, is calculated. The black lines mark the *SRIM* calculated transmission energies for each letter.

The colouring of the RCF is converted into absorbed energy dose based on the film calibration. Figure 6.6 shows the deposited energy in each RCF layer behind the imaging sample. The protons deposit approximately 90% of their energy in their stopping layer, so that they do not colour the next layers, which lie behind the stopping layer, at this position. The energy loss dependency on the object thickness is shown in the stack and matches with the predictions: At the reference position (i-dot), the beam passes without energy loss and is stopped within the sixth RCF layer. After passing the first two letters (L and i), this part of the beam ends in the fifth RCF film. Behind the last three thicker letters, the beamlets are stopped as expected in the front layers (G in the fourth layer; H,T in the third layer).

The deposited dose in the RCF stack is converted into an energy-dependent particle distribution for each pixel based on *SRIM* calculated energy loss values. Afterwards, the energy of the maximum for each fitted distribution is determined and this pixel is colour-coded indicating the transmitted beam energy, shown in figure 6.7. The colour-coding reproduces the imaging object. At the reference position, the central energy interval of (9.1 ± 0.3) MeV is measured. The stopping power is increasing from left to right corresponding to the rising thickness. Due to straggling effects within the imaging object, the edges of the last two letters are not resolved properly.

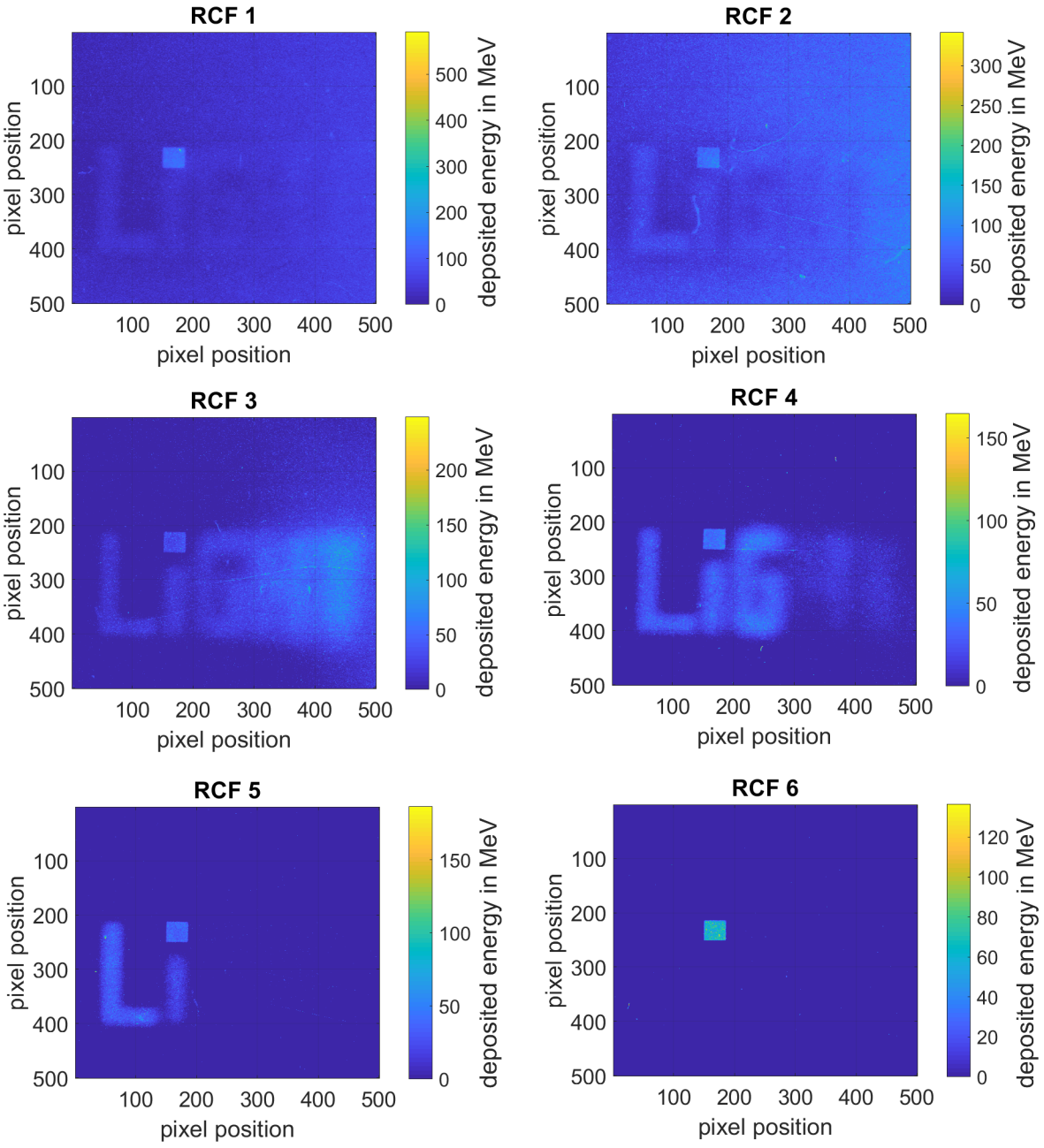

Figure 6.6: The energy deposition inside each RCF film behind the imaging target is shown.

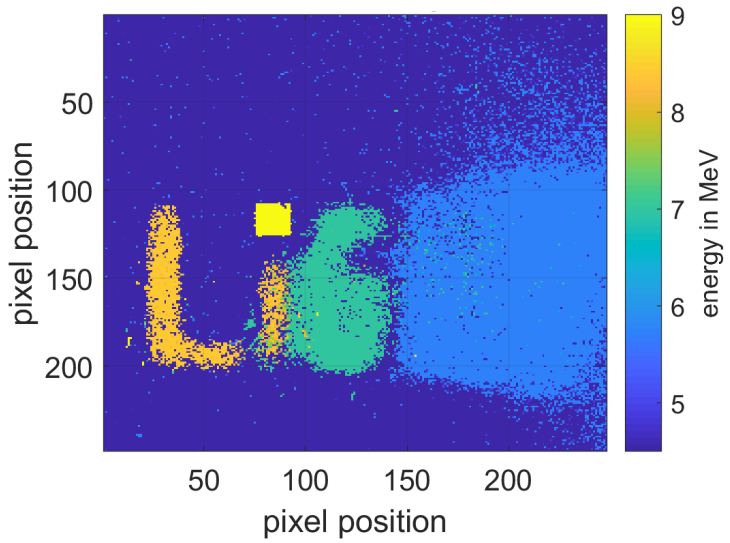

Figure 6.7: Colour coding of the imaging results. The colour indicates the energy of the transmitted proton beam at each pixel. The unaffected beam passes the i-dot with an energy interval of (9.1 ± 0.3) MeV. The energy loss increases from left to right resulting in a lower transmitted proton energy.

The proton transmission through the imaging sample was modeled with the MC simulation code *SRIM* [Ziegler, 2013]. *SRIM* calculates the final spatial and energy distribution of ions propagating materials with a defined thickness. The analysed and calculated transmitted energy values are listed in table 6.1. The comparison indicates an agreement between the measurement and the simulation. The energy resolution of the measurement is limited due to the thickness of the RCF film layers. The thicker the thickness of the imaging sample, the worser is the the energy resolution and a discrepancy between the measured and calculated values is observed. As a result, the last two letters cannot be distinguished, as the proton beam is stopped for both thicknesses in the same RCF layer (third layer, compare figure 6.5). The measured energy values for these two letters are not comparable to the calculated results.

Table 6.1: The corresponding transmitted proton energy of (9.1 ± 0.3) MeV proton beam is calculated with *SRIM* for each letter thickness and compared to the measured values.

letter	thickness in µm	simulated energy in MeV	measured energy in MeV
i-dot	0	9.1	9.1 ± 0.3
L	20	8.5 ± 0.3	8.4 ± 0.3
I	40	7.9 ± 0.3	8.1 ± 0.3
G	60	7.3 ± 0.3	7.0 ± 0.3
H	80	6.6 ± 0.3	5.8 ± 0.3
T	100	5.9 ± 0.3	5.1 ± 0.3
outside	120	5.1 ± 0.3	2.9 ± 0.3

7 Summary and conclusions

This work was performed within the laser and plasma physics group at the institute of nuclear physics of the Technische Universität Darmstadt and was supported by the LIGHT collaboration. The goal of this thesis was the optimization of the laser-driven ion beamline for protons and demonstrate its final focusing capability to achieve highest proton intensities at the interaction point for applications. Additionally, the beam homogeneity was improved and an proton imaging study was performed.

The PHELIX laser ($\lambda = 1053\,\text{nm}$, $\tau = 650\,\text{fs}$, $\text{E} \approx 15\,\text{J}$) was focused on a 10 µm thin gold target with a focal spot size of 3.5 x 3.5 mm^2 driving the TNSA mechanism. The source characterization with an RCF stack showed an exponentially decaying spectrum with a cut-off energy of $\approx 21.5\,\text{MeV}$. The fit parameters were the maximum number of protons $N_0 = (4.48 \pm 1.10) \cdot 10^{11}$ and the temperature $k_B T = (19.35 \pm 8.64)\,\text{MeV}$. Analysing the spectrum, the half envelope divergence angle had a value up to $\approx 28°$ directly behind the target. The goal was to transport and shape the proton beam at a central energy $E_0 = 8\,\text{MeV}$ along the beamline. In this context, $(1.5 \pm 0.3) \times 10^{10}$ protons were available in an energy interval of $(8 \pm 2)\,\text{MeV}$ at the source.
The emittance was measured with a pepperpot device, which was positioned 1055 mm from the TNSA source. On the RCF film behind it, a magnification of the grid was observed indicating low emittance values. The analysis of the space space led to an emittance of $(\epsilon_x, \epsilon_y) = (1.0 \pm 0.4, 0.8 \pm 0.4)\,\text{mm mrad}$.

The beam was collimated with a pulsed high-field solenoid, which was positioned 4 cm from the source and operated at 6.5 T. While in the forerunning work on this topic an energy spread of $(18 \pm 3)\%$ at FWHM around the selected energy $E_0 = 9.6\,\text{MeV}$ was intensively investigated [Busold, 2014], in this thesis, the energy spectrum was measured with an RCF stack for control reasons of the beamline alignment. In the presented measurement, an energy interval around the central energy of 6.5 MeV was collimated and selected. Within this energy interval of $(6.5 \pm 0.25)\,\text{MeV}$, $(1.22 \pm 0.12) \times 10^9$ protons were detected. Irregularities were observed in the transverse beam profile, which were not predicted by the *TraceWin* simulations. To understand this discrepancy, further investigations on this observation are planned by the collaboration partner HZDR.
The emittance measurement was repeated with the turned-on solenoid to determine the emittance after beam collimation. The analysis of the phase space led to an emittance of $(\epsilon_x, \epsilon_y) = (5.5 \pm 1.0, 4.0 \pm 1.7)\,\text{mm mrad}$. It was observed that the solenoid's alignment has

a significant impact on the measured beamlet distribution behind the pepperpot and further investigations are necessary.

By the use of an rf cavity, the beam was rotated in longitudinal phase space around its central energy. As the rf cavity is designed for 8 MeV/u, the central proton energy is chosen in this energy region. For the ideal phase rotation, a beam injection at a synchronous phase $\Phi_s = -90°$ is necessary, which is found by scanning the relative rf phase. Then the setting of the rf amplitude determines the influence on the beam dynamics.
The energy compression was measured with a dipole spectrometer and showed an energy spread of (2.7 ± 1.7)% (FWHM) around a central energy of $E_0 = (9.7 \pm 0.1)$ MeV [Busold, 2014].
For the measurement of the temporal focus, diamond detectors were specially developed to fulfill the temporal requirements. In this context, the fastest time-of-flight detector is a membrane detector, which has a $5-7\,\mu$m thin diamond membrane with a 0.5 µm diameter. The combination of a small detector electrode and an impedance matched signal outlet leads to time response properties with a signal pulse resolution of $\tau = (113 \pm 11)$ ps (FWHM). Using this type of semiconductor detector, ion bunch durations above 200 ps can be measured. As a complementary system, the plastic scintillator BC-442Q with a decay time of 0.7 ns was combined with a streak camera. Both diagnostics were consistent in their behaviour, but the resolution of the scintillator system was limited by its decay time. The diagnostics were setup in 6 m distance from the source.
By finding the ideal relative rf phase and rf amplitude, temporal focuses below 600 ps (FWHM) were achieved in four beamtimes. Hence, the reproducibility of subnanosecond proton bunch durations was demonstrated. The proton bunch duration, which was measured in the beamtime in September 2017 with the current setup, was determined as $\tau = (593 \pm 40)$ ps at FWHM. Based on the response function of the diamond detector, the temporal profile was deconvoluted resulting in $\tau = (468 \pm 40)$ ps at FWHM.

One central goal of this work was the demonstration of the final transverse focusing at the interaction point for applications. Many applications demand high particle intensities. Therefore, the last beamline element is a second pulsed high-field solenoid for transverse focusing. In this measurement, the first solenoid was used for the beam collimation, the rf cavity was not operated because of technical problems and the second solenoid was operated at 5.8 T. The beam was focused down to a round-shaped focal spot size of 1.1 mm x 1.2 mm at FWHM containing (3.5 ± 0.22) x 10^8 protons. In future, the phase rotation and final focusing will be demonstrated simulatenously. This will enable proton intensities up to 5.8 x 10^{19} protons/(s×cm^2).

Finally, the LIGHT beamline was applied for proton imaging of a solid object. For this application, energy-compressed proton bunches were produced at the interaction point in the Z4

target chamber. As a reference, the transverse beam uniformity was characterized and optimized using a 1.25 µm mylar straggling foil to reduce the irregularities in the beam profile. This resulted in a beam uniformity $U_\eta = 0.23$ and a fill factor FF = 0.20. The solid object was positioned as a secondary target at the end of the beamline and an imaging study was performed. The imaging contrast was generated by an energy measurement using an RCF stack in 6 mm distance from the object. The object itself consisted of several nickel layers with different thicknesses between 0 µm and 120 µm. The central energy of the reference beam was measured as (9.1 ± 0.25) MeV and the energy loss behind the different layers corresponded to the *SRIM* calculated values, e.g. the transferred energy behind 20 µm has a calculated value of (8.5 ± 0.3) MeV by *SRIM* and a measured value of (8.4 ± 0.3) MeV.

In this thesis, it could be shown that the laser-driven proton beamline provides reproducibly proton bunches with subnanosecond durations and highest peak intensities. With further research and development in the following years, this laser-driven ion beamline will be utilized for applications. For the planning of future experiments, an overview of the achieved proton beam parameters, which were obtained in the forerunning work [Busold, 2014] and this work, is provided in table 7.1.

Table 7.1: Overview of achieved beam parameters.

element	distance	experimental achievements
TNSA source	0 m	exponentially decaying spectrum with $E_{cut} = 21.5$ MeV, $N_0 = (4.48 \pm 1.10) \cdot 10^{11}$, $k_B T = (19.35 \pm 8.64)$ MeV, divergence up to 27.7°
beam collimation	3 m	energy spread of $\Delta E = (18 \pm 3)\%$ (FWHM), at a central energy $E_0 = (9.7 \pm 0.1)$ MeV
energy compression	3 m	energy spread of $\Delta E = (2.7 \pm 1.7)\%$ (FWHM), at a central energy $E_0 = (9.7 \pm 0.1)$ MeV
temporal focus	6 m	$\tau = (593 \pm 40)$ ps (FWHM)
final transverse focusing	6 m	1.1 mm x 1.2 mm at FWHM, $(3.5 \pm 0.22) \times 10^8$ protons in an energy interval $E_0 = (9.55 \pm 0.25)$ MeV

8 Perspectives

This work presents the significant progress of beam shaping of laser-accelerated protons using the LIGHT beamline and the final beam parameters at the interaction point for applications. Continuous improvement and further investigations are still necessary for the success of the LIGHT project. The LIGHT collaboration will concentrate its research on the following topics in the near future which will be introduced in this chapter:

- target optimization: electromagnetic lensing
- application studies
- new permanent beamline for LIGHT
- injection into the heavy ion synchrotron SIS18

While the first three listed topics are scheduled for the near future, the last topic is actually intensively discussed and further beam parameter measurements are necessary for decision-making.

8.1 Target optimization: electromagnetic lensing

The proton source is defined by the laser and target parameters. In this thesis, thin target foils have been used as a target for the TNSA mechanism. This section will concentrate on the beam pre-collimation with a micro Helmholtz cavity as a new target design [Santos et al., 2018].
The TNSA source typically has a broad energy spectrum and a large angular divergence. These parameters can be modified by changing the target design. M. Ehret *et al.* showed successful pre-collimation of 12 MeV protons over several cm with the PHELIX laser [Ehret, 2018]. A lensing target is being developed for the pre-collimation of the proton beam in front of the solenoid, which is adapted to the PHELIX parameters at Z6 [Ehret, 2018].

The advanced target consists of a thin disc followed by two coils. The left figure 8.1 shows the target configuration for the micro Helmholtz cavity. The disc is a 10 µm thin copper foil from which the protons are accelerated. The two omega-shaped coils are conductively connected to the disc and possess a diameter of 500 µm. The EM-fields are generated by the electromagnetic pulse (EMP) and propagate following the target geometry originating from the laser interaction. The protons are deflected by the existing EM fields resulting in an efficient pre-tailoring of the beam. The distances between the disc and the coils are adapted to a charged beam with an energy interval of (8 ± 2) MeV.

To perform simulations studies on the optimal target design, the simulation code **PA**rticle **F**ield **I**nteractio**N** (PAFIN) has been developed. This code is a multicore code for proton deflectometry and relativistic electron transport using electric and magnetic fields [Ehret, 2016]. With the performed simulations, the distances and radii of both coils are optimized aiming to increase the proton yield arriving in the solenoid. As a result, the first coil is positioned 0.75 mm behind the disc with a radius of 250 µm and the second at 0.5 mm behind the first coil with a radius of 360 µm. Without an EM pulse, the proton energy interval of (8 ± 2) MeV protons are captured with an emittance of $(\epsilon_x, \epsilon_y) = (895,\ 880)$ mm mrad. In the worst case, the EMP contains 100 nC, while for the best case 300 nC are included. The 100 nC EMP does not effect the particle beam. With a 300 nC pulse, 10 % more protons with an emittance of $(\epsilon_x, \epsilon_y) = (914, 462)$ mm mrad are captured with the current LIGHT setup. The middle figure 8.1 shows the simulated particle numbers on the RCF film in front of the solenoid entrance. The beam is concentrated in the center and more particles will be able to enter the solenoid. The PAFIN calculation of the beam divergence shows an initial divergence up to 2 rad behind the thin foil, which is the first part of the target. The beam divergence is significantly reduced to 0.6 rad after passing the two coils of the target design. Due to the divergence reduction, more particles are collimated by the solenoid and are transported along the beamline.

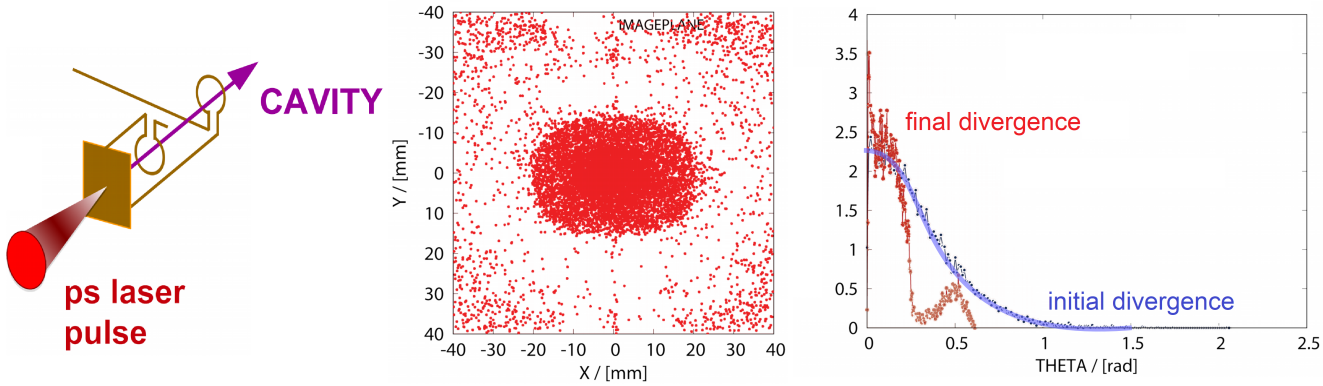

Figure 8.1: Micro Helmholtz cavity target design [Ehret, 2018]. Left: Helmholtz cavity target design. Middle: transverse beam profile of the target calculated with PAFIN at the entrance of the solenoid. Right: calculated initial divergence (behind the thin foil, *red*) and final divergence (behind the two coils, *blue*).

8.2 Going towards application studies

8.2.1 Stopping power measurements in a plasma

In the application field, the LIGHT collaboration will concentrate its research on stopping power measurements inside a dense plasma. The investigation of the interaction between ions and a dense plasma is essential e.g. to understand the key process in inertial confinement fusion (ICF) and heating schemes using ion beams as main drivers for ion-driven fast ignition or heavy ion fusion [Bychenkov et al., 2001, Roth, 2009, Cayzac et al., 2017]. The interaction of ions with a plasma is a central research topic of the working group laser and plasma physics at Technische Universität Darmstadt. Therefore, it is necessary to generate a plasma with well-defined density, extension, and temperature. This can be done with the two local laser systems PHELIX (shortly described in section 4.1) and nhelix (**n**anosecond **h**igh **e**nergy **l**aser for **i**on beam e**x**periments). The nhelix laser is a Nd:glass system consisting of an oscillator and several amplification rods operating at 1064 nm. After frequency doubling, it delivers laser pulses with an energy up to 40 J and a pulse length of 6-20 ns [Zobus, 2016].

In the past years, two main approaches were used to generate a carbon plasma via laser irradiation, which offers the advantage of high electron densities and high temperatures. The first approach produces X-rays via a converter target that is used for homogeneous heating of the carbon target [Schumacher, 2011, Hessling, 2010]. The resulting plasma has an achievable electron density from 10^{21} cm^{-3} to 10^{22} cm^{-3} and a temperature of 30 eV to 40 eV. For this purpose, a laser system is necessary which delivers several hundreds of Joules in a nanosecond.
The second approach is the direct laser irradiation of a thin carbon foil using a high energy laser system. Hereby, a lower electron density from 10^{20} cm^{-3} to 10 ^{21} cm^{-3} and higher temperatures of 150 eV to 200 eV are reached [Frank, 2012]. Subsequently, the ion beam interacts with the produced plasma in both scenarios. For the LIGHT beamline, the second approach is of interest and will be considered in the following paragraph, as the first approach is beyond the capability of the nhelix laser.

In previous experiments at GSI [Cayzac et al., 2017, Ortner et al., 2015, Frank et al., 2013], a carbon foil was heated from both sides with the PHELIX and nhelix laser systems. Their frequency doubling results in an increase of the critical density affecting a higher transfer of laser energy into radiation. This leads to a global heating of the target and reduces the impact of inhomogeneities in the laser profile on the laser matter interaction. As a result, the carbon is fully ionized after 6-7 ns with free electron densities of $n_e \approx 5 \times 10^{20}$ cm^{-3} and electron temperatures of $T_e \approx$150 eV [Frank et al., 2013, Cayzac et al., 2015], corresponding to an ideal, non-degenerated target. The plasma parameters were simulated with the RALEF2D (Radiation

Arbitrary Lagrangian-Eulerian Fluid dynamics) code [Basko et al., 2017] by An. Tauschwitz for times 0-15 ns after target heating. The goal is to obtain a reproducible, homogeneous and fully ionized plasma.

While the plasma expands on the nanosecond scale, the UNILAC delivers ion bunches with a pulse width between 3-4 ns in a bunch period of 9.2 ns (operation frequency 108 MHz) and with 10^5 particles leading to a time-averaging effect as the density profile of the plasma changes during this interaction process. As shown in this work, the LIGHT beamline is able to deliver proton bunches with bunch durations below 500 ps (FWHM). The use of bunch lengths below 1 ns will significantly reduce the time-averaging effect. As the energy loss is proportional to the atomic number Z^2, protons are due to their low stopping power not suitable for this experiment. Therefore, higher mid-Z ions are favorable and are currently investigated [Ding, 2018]. For a 50 cm distance between plasma and detector, the energy loss in 100 $\mu g/cm^2$ cold carbon of 8 MeV protons is $\Delta E = 6$ keV resulting in a time difference of 5 ps compared to the reference beam. This cannot be resolved by any detector. In case of 42 MeV carbon ions, the energy loss is $\Delta E = 0.8$ MeV leading to a time delay of 1.56 ns (calculated with SRIM [Ziegler, 2013]). Therefore, mid-Z ion bunch acceleration and their longitudinal phase rotation have to be optimized. The higher particle numbers of a laser-accelerated ion beam in contrast to conventional beams will increase the signal intensity. Together with the short ion bunch durations, this will lead to smaller error bars.

In the past, a 100 $\mu g/cm^2$ carbon foil was heated with the frequency-doubled beams (532/527 nm) with an energy of 30 J and a pulse length of 7 ns (FWHM). As the PHELIX is necessary to drive the TNSA source, only the nhelix laser can be used and has to be splitted for two-sided heating. Simulations predict that the available laser energy of 20 J per side are not sufficient for a full ionization. For a full ionization, an energy of 25 J per side and a focal spot size of 1 mm diameter is necessary. The focal spot size cannot be further reduced, otherwise twodimensional effects have to be considered for the plasma expansion. Therefore, the nhelix system will need an upgrade to higher energies in future.

The stopping power setup will be positioned inside the second target chamber of the LIGHT beamline. Figure 8.2 shows the setup scheme. Using the second solenoid, laser-accelerated ion bunches will be focussed on a pinhole. In front of the pinhole or in front of the solenoid, a diamond detector is positioned to detect the arrival time. The pinhole defines the spatial beam parameters. Behind the pinhole the beam passes the laser-irradiated carbon foil and finally hits a second diamond detector.

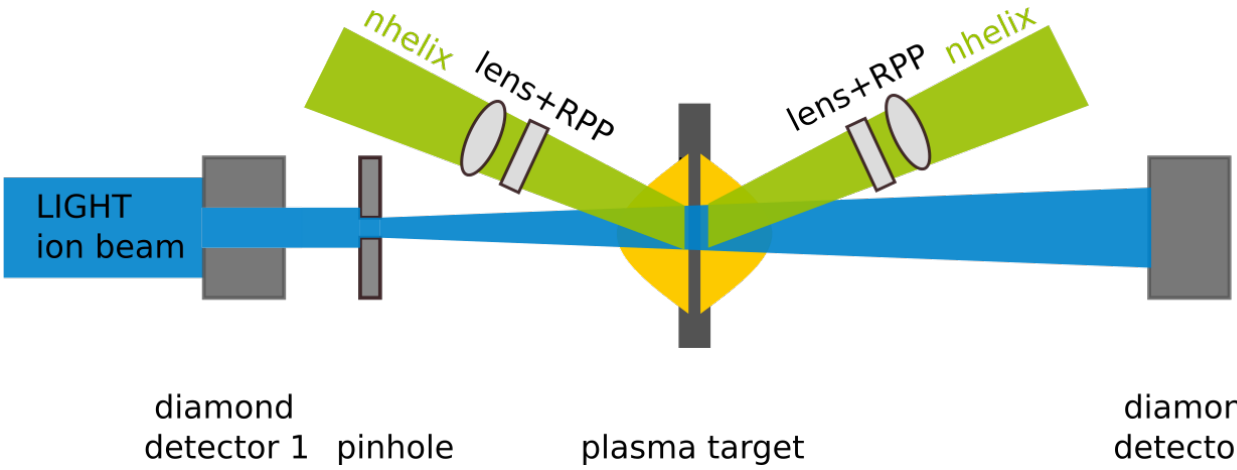

Figure 8.2: Schematics of the setup: the LIGHT ion beam impinges the first diamond detector and passes it through a hole. Afterwards, it is collimated through a 1 mm pinhole and hits the secondary target, the carbon foil. At the same time, the nhelix laser beam is splitted in two. The two half-beams are homogenized via a Random Phase Plate (RPP) and focused on the thin carbon foil (carbon 100 $\mu g/cm^2$) simultaneously from two sides leading to a plasma generation. The ion beam passes the carbon plasma and hits the second diamond detector.

If a projectile ion with the entrance energy E_p passes the target (cold foil or plasma), it leaves the target with an energy reduced by ΔE. The energy loss reduces the velocity of the projectile $v'_p < v_p$ and leads to a longer time of flight over the distance L: $t'_L = v'_p/L > t_L = v_p/L$. The energy loss is calculated by the time difference between an unstopped and a slowed down ion bunch. The time diference is given by $\Delta t = t_L - t'_L$ leading to the energy loss formula:

$$\Delta E = \left(1 - \frac{1}{1 - \frac{v_p}{L}\Delta t}\right) E_p \tag{8.1}$$

based on projectile mass m_p and velocity $v_p = \sqrt{2E_p/m_p}$. While the first diamond detector records the arrival time of the uninfluenced beam ($t = 0$), the second detector measures the arrival time after the interaction. It is recommendable to perform three shots for each carbon foil: as the first shot, the beam passes the cold carbon foil (reference for cold matter). A second shot is done to probe the carbon plasma. Finally, a reference shot without the carbon foil is needed after the carbon foil is destroyed by laser irradiation. The reference shot enables to determine the initial proton energy E_p. From the difference in arrival time, the energy loss is calculated by the given formula 8.1.

8.2.2 Other application studies by the LIGHT collaborators

Besides this experiment and the present imaging study, shaped laser-driven ion beams open up a field for numerous applications, e.g. medical and material science. The LIGHT collaboration

partner HZDR has set up a pulsed beamline for tests consisting of a pulsed high-field solenoid and a dipole. They demonstrated the capture, deflection and spectral shaping of proton beams up to 31 MeV [Kroll, 2018] showing that the dose delivery system can be used as a compact and more efficient light-weight proton gantry [Masood et al., 2017]. Additionally, the radiobiological effectiveness of laser-accelerated protons was measured in in-vitro cell samples [Kraft et al., 2010, Zeil et al., 2013].

The GSI material science unit will use the short proton bunches to study online beam-induced effects such as pressure waves and ion-induced luminescence [Tomut and Simon, 2018]. The study of response to pressure waves of differently microstructured materials using Laser Doppler Vibrometry will deliver information about thermal stress in carbon. In addition, the feasibility of diamonds as a beam diagnostic device and its most efficient centers for ion-induced luminescence will be investigated.

8.3 New permanent beamline for LIGHT

In future, a new 8 m long, permanent beamline with an own rf supply will be realized in the framework of **A**ccelerator **T**echnology **H**elmholtz i**N**fr**A** structure (ATHENA), which is a strategic accelerator program by the Helmholtz Association in Germany.
As part of this program, the actual test stand for ion acceleration and transport will be upgraded to a new beamline setup. Figure 8.3 shows an overview of the designed beamline.

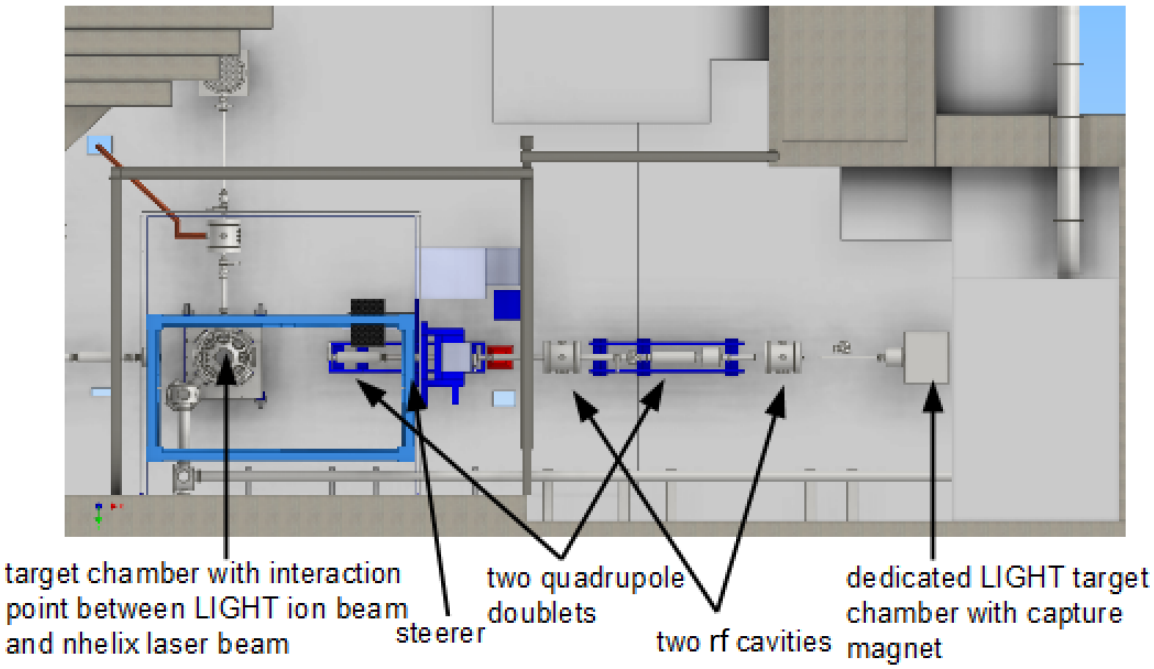

Figure 8.3: Overview of the new permanent beamline from right to left (courtesy of D. Schumacher): target chamber with PHELIX-driven ion source and solenoid, two rf cavities, two quadrupole doublets, steerer and Z6 target chamber.

An own rf supply will enable independent experiments from the UNILAC infrastructure. A dedicated target chamber will be positioned next to the PHELIX compressor at Z6. Inside this chamber, laser-based ions will first be accelerated by the laser and then collimated by a solenoid. As this chamber will only be used by the LIGHT collaboration, the solenoid will be permanently on its position and does not need to be aligned in each experimental campaign, as the alignment process is very time-consuming (3-5 beamtime days). Beam shaping will be performed with two rf cavities, two quadrupole doublets and a steerer. The longer drift distance and the accelerator elements open up more possibilities to control the beam. Afterwards, the beam will enter the Z6 target chamber, the interaction point between the LIGHT ion beam and nhelix.

8.4 Injection into heavy ion synchrotron SIS18

In conventional accelerators, particles have to pass several components from their source until they reach the experiment. Typical particle sources deliver particles with a low energy. These particles are accelerated in a pre-accelerator, e.g. a linac, to a sufficient velocity enabling the injection into the circular main accelerator. Finally, they are ejected with the desired energy and transported to the experimental area [Wille, 1996].

The core of the existing GSI accelerator facility is the linear accelerator **UNI**versal **L**inear **AC**celerator (UNILAC). The UNILAC provides ion species (from protons to uranium) and charge states over a wide range. Ions are generated using up to three sources and accelerated to $\approx 1.4\,\mathrm{MeV/u}$ by a high current injector. Typically, average charge states are used which are produced using a gas stripper before the ions enter the UNILAC structure. The beam energy is increased up to 11.4 MeV/u. This beam is used for low-energy experiments in the experimental hall or is injected via a 150 m long transfer channel in the heavy ion synchrotron (*German:* ***S****chwer-****I****onen-****S****ynchrotron*, SIS18). Inside the SIS18, the particle bunches are accumulated, accelerated up to the requested energy, and afterwards transported to the experimental hall or to the experimental storage ring, whereas the transport is via the **FR**agment **S**eparator (FRS) or directly. After the transport, the ions are used for diverse experiments in nuclear physics, plasma physics, bio physics or material science. Figure 8.4 presents an overview of the existing accelerator system. More details can be found in [Appel, 2011, Singh, 2014].

The SIS18 itself is a circular accelerator with a circumference of 216.72 m, which consists of twelve nearly identical segments, shown in figure 8.5 [Franczak, 1987]. Each segment consists of two dipoles, three quadrupoles, and a sextupole. The dipoles keep the beam on the circular trajectory, the quadrupole triplett focuses it transversely, and the sextupole compensates field errors. Two rf cavities with 16 kV and a 0.8-5.6 MHz frequency bandwidth accelerate the beam. Several diagnostics instruments are placed between the segments. The maximum magnetic rigidity is 18 Tm enabling a maximum proton energy of 4.5 GeV/u.

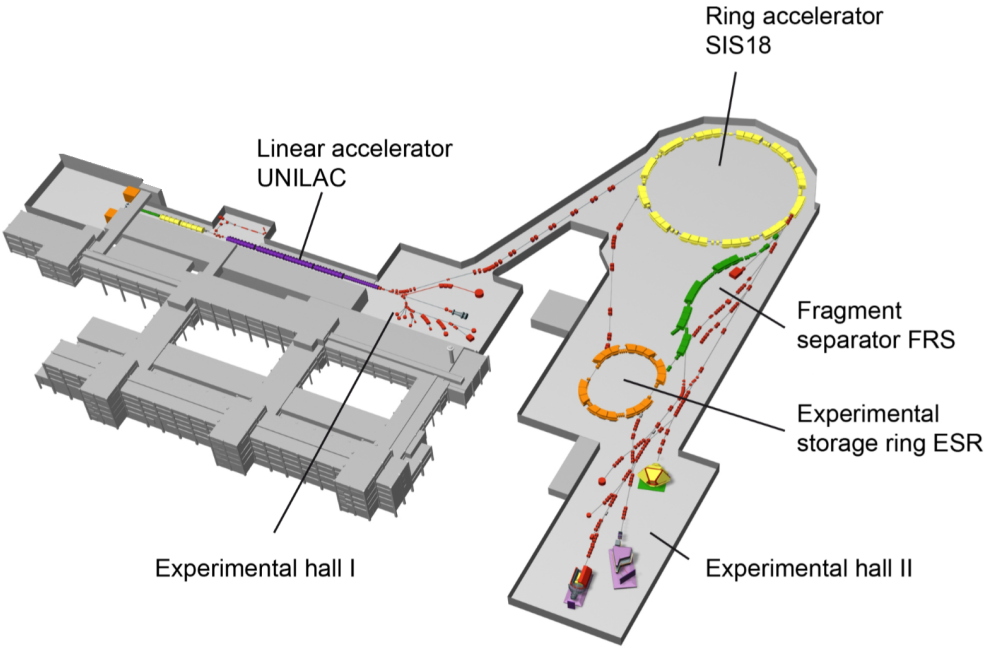

Figure 8.4: Scheme of the accelerator facility at GSI [Singh, 2014]: the linear accelerator UNILAC accelerates the beam (purple), which can be used for experiments in the the experimental hall I. Alternatively, the beam is transported through a transport channel (red) to the synchrotron SIS18 (yellow), in which the particles are accelerated to higher energies. From this point, the particles can be transported to the experimental storage ring (orange), indirectly through the fragment separator (FRS, green) or directly to the experimental hall II.

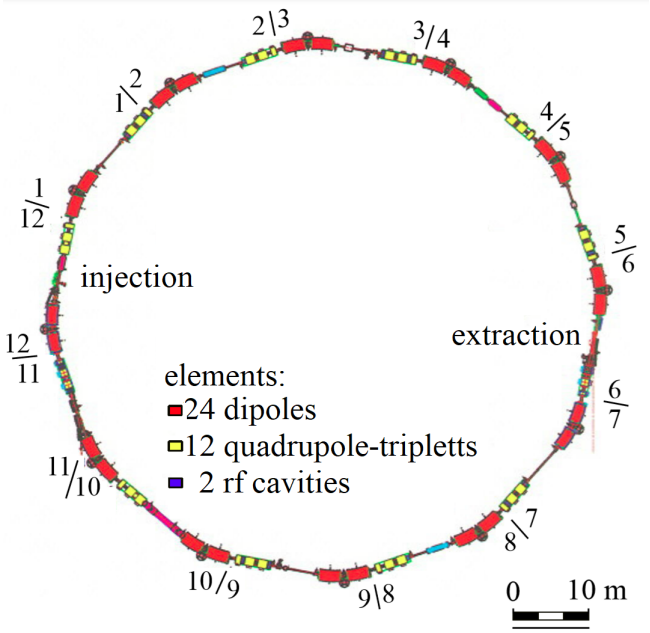

Figure 8.5: Overview of the synchrotron SIS18 with a circumference of 216.72 m [Appel, 2011]: each of the twelve segments consists of two dipoles (red), a quadrupole-triplett (yellow) and a sextupole (not in this figure). Two rf cavities (blue) accelerate the beam.

For the optimal injection process into the SIS18, the phase space has to be adapted: the injected beam ellipsoid has to be fitted to the characteristic machine ellipsoid. This means the transverse phase ellipses with the Twiss parameters (α_x,β_x, γ_x) and (α_y,β_y, γ_y) have to match the characteristic ellipses of the synchrotron at the transfer point [Hinterberger, 2008, Wille, 1996, Appel, 2011]. For a successful injection, the beam has to fulfill the minimum acceptance A_{inj} which is calculated by

$$A_{inj} \geqq \frac{a^2}{\beta} > \frac{d^2}{\beta} \tag{8.2}$$

with the aperture d and the amplitude function β of the accelerator. Here, the incident angle is not taken into account, which can lead to an increase of the acceptance value.

The injection process of the SIS18 transfer channel requires a full momentum spread of $\Delta p/p = 10^{-3}$, an emittance of $\left(\epsilon_x, \epsilon_y\right) = (15, 15)$ mm mrad, and a minimal energy of 8 MeV/u. So far these parameters were not measured at the injection point with the LIGHT beamline, but they are within its capability. Moreover, a minimum number of 10^6 protons is necessary to detect the injected proton bunch with a fluorescent target, which will be monitored by a camera system. In the performed LIGHT experiment, a 1 mm pinhole was positioned at the interaction point and the particle number has been ten times higher than the requirement $\left(> 10^7\right)$.

This proof of principle experiment is intensively discussed as a possible application of the LIGHT project. It would demonstrate the world-wide first injection of a laser-driven ion beam in an existing conventional accelerator. Therefore, a comprehensive analysis and improvement of the final beam parameters and a precise setup of the magnets between the LIGHT beamline and the transfer channel are necessary. While the PHELIX laser delivers an intense laser pulse every 60 minutes, advanced laser systems with higher repetition rates are currently developed and will become available in the future. Such a high repetition rate system might be able to run the LIGHT beamline as an alternative injector for FAIR and replace the standard ion source in case of emergencies.

Bibliography

[Appel, 2011] Appel, S. (2011). *Simulation und Messung longitudinaler Raumladungseffekte in intensiven Ionenstrahlen im SIS18 Synchrotron*. PhD thesis, Technische Universität Darmstadt.

[Bagnoud et al., 2010] Bagnoud, V., Aurand, B., Blazevic, A., Borneis, S., Bruske, C., Ecker, B., Eisenbarth, U., Fils, J., Frank, A., Gaul, E., Goette, S., Haefner, C., Hahn, T., Harres, K., Heuck, H.-M., Hochhaus, D., Hoffmann, D., Javorkova, D., Kluge, H.-J., Kuehl, T., Kunzer, S., Kreutz, M., Merz-Mantwill, T., Neumayer, P., Onkels, E., Reemts, D., Rosmej, O., Roth, M., Stoehlker, T., Tauschwitz, A., Zielbauer, B., Zimmer, D., and Witte, K. (2010). Commissioning and early experiments of the phelix facility. *Applied Physics B: Lasers and Optics*, 100:137–150.

[Basko et al., 2017] Basko, M. M., Maruhn, J., and Tauschwitz, A. (2017). RALEF-2D: A 2D hydrodynamic code with heat conduction and radiation transport. *Main Report*.

[Bauer and Mulser, 2007] Bauer, D. and Mulser, P. (2007). Vacuum heating versus skin layer absorption of intense femtosecond laser pulses. *Physics of Plasmas*, 14(2):023301.

[Beg et al., 1997] Beg, F., Bell, A. R., Dangor, A. E., Danson, C., Fews, A. P., Glinsky, M., Hammel, B., Lee, P., Norreys, P. A., and Tatarakis, M. (1997). A study of picosecond laser-solid interactions up to 10^{19} W cm^{-2}. *Physics of Plasmas*, 4.

[Berdermann et al., 2010a] Berdermann, E., Pomorski, M., de Boer, W., Ciobanu, M., Dunst, S., Grah, C., Kiš, M., Koenig, W., Lange, W., Lohmann, W., Lovrinčić, R., Moritz, P., Morse, J., Mueller, S., Pucci, A., Schreck, M., Rahman, S., and Träger, M. (2010a). Diamond detectors for hadron physics research. *Diamond and Related Materials*, 19(5):358 – 367. Proceedings of Diamond 2009, The 20th European Conference on Diamond, Diamond-Like Materials, Carbon Nanotubes and Nitrides, Part 1.

[Berdermann et al., 2010b] Berdermann, E., Pomorski, M., de Boer, W., Ciobanu, M., Dunst, S., Grah, C., Kiš, M., Koenig, W., Lange, W., Lohmann, W., Lovrinčić, R., Moritz, P., Morse, J., Mueller, S., Pucci, A., Schreck, M., Rahman, S., and Träger, M. (2010b). Diamond detectors for hadron physics research. *Diamond and Related Materials*, 19(5):358 – 367. Proceedings of Diamond 2009, The 20th European Conference on Diamond, Diamond-Like Materials, Carbon Nanotubes and Nitrides, Part 1.

[Bethe, 1930] Bethe, H. (1930). Zur Theorie des Durchgangs schneller Korpuskularstrahlen durch Materie. *Annalen der Physik*, 5:325.

[Boine-Frankenheim, 2015] Boine-Frankenheim, O. (2015). *Lecture notes on accelerator physics*. Technische Universität Darmstadt.

[Brabetz, 2014] Brabetz, C. (2014). *Development of specially shaped laser beams for the optimized acceleration of particles*. PhD thesis, Johann Wolfgang Goethe-Universitaet.

[Brunel, 1987] Brunel, F. (1987). Not-so-resontant, resonant absorption. *Phys. Rev. Lett. 59, 52-55*.

[Burris-Mog et al., 2011] Burris-Mog, T., Harres, K., Nürnberg, F., Busold, S., Bussmann, M., Deppert, O., Hoffmeister, G., Joost, M., Sobiella, M., Tauschwitz, A., Zielbauer, B., Bagnoud, V., Herrmannsdoerfer, T., Roth, M., and Cowan, T. E. (2011). Laser accelerated protons captured and transported by a pulse power solenoid. *Phys. Rev. ST Accel. Beams*, 14:121301.

[Busch, 1926] Busch, H. (1926). Berechnung der Bahn von Kathodenstrahlen im axialsymmetrischen elektromagnetischen Felde. *Annalen der Physik*, 386(25):974–993.

[Busold, 2014] Busold, S. (2014). *Construction and characterization of a laser-driven proton beamline at GSI*. PhD thesis, Technische Universität Darmstadt.

[Busold et al., 2014a] Busold, S., Almomani, A., Bagnoud, V., Barth, W., Bedacht, S., Blažević, A., Boine-Frankenheim, O., Brabetz, C., Burris-Mog, T., Cowan, T., Deppert, O., Droba, M., Eickhoff, H., Eisenbarth, U., Harres, K., Hoffmeister, G., Hofmann, I., Jaeckel, O., Jaeger, R., Joost, M., Kraft, S., Kroll, F., Kaluza, M., Kester, O., Lecz, Z., Merz, T., Nürnberg, F., Al-Omari, H., Orzhekhovskaya, A., Paulus, G., Polz, J., Ratzinger, U., Roth, M., Schaumann, G., Schmidt, P., Schramm, U., Schreiber, G., Schumacher, D., Stoehlker, T., Tauschwitz, A., Vinzenz, W., Wagner, F., Yaramyshev, S., and Zielbauer, B. (2014a). Shaping laser accelerated ions for future applications – the LIGHT collaboration. *Nuclear Instruments and Methods in Physics Research Section A: Accelerators, Spectrometers, Detectors and Associated Equipment*, 740:94 – 98. Proceedings of the first European Advanced Accelerator Concepts Workshop 2013.

[Busold et al., 2015] Busold, S., Schumacher, D., Brabetz, C., Jahn, D., Kroll, F., Deppert, O., Schramm, U., Cowan, T., Blazevic, A., Bagnoud, V., and Roth, M. (2015). Towards highest peak intensities for ultra-short mev-range ion bunches. *Scientific reports*, 5:12459.

[Busold et al., 2014b] Busold, S., Schumacher, D., Deppert, O., Brabetz, C., Kroll, F., Blazevic, A., Bagnoud, V., and Roth, M. (2014b). Commissioning of a compact laser-based proton beam line for high intensity bunches around 10 MeV. *Phys. Rev. ST Accel. Beams*, 17:031302.

[Bychenkov et al., 2001] Bychenkov, V. Y., Rozmus, W., Maksimchuk, A., Umstadter, D., and Capjack, C. E. (2001). Fast ignitor concept with light ions. *Plasma Physics Reports*, 27(12):1017–1020.

[CadSoft, 2016] CadSoft (2016). Eagle - pcg design software.

[Canali et al., 1975] Canali, C., Jacoboni, C., Nava, F., Ottaviani, G., and Alberigi-Quaranta, A. (1975). Electron drift velocity in silicon. *Phys. Rev. B*, 12:2265–2284.

[Cayzac et al., 2015] Cayzac, W., Bagnoud, V., Basko, M., Blazevic, A., Frank, A., O. Gericke, D., Hallo, L., Malka, G., Ortner, A., Tauschwitz, A., Vorberger, J., and Roth, M. (2015). Predictions for the energy loss of light ions in laser-generated plasmas at low and medium velocities. 92.

[Cayzac et al., 2017] Cayzac, W., Frank, A., Ortner, A., Bagnoud, V., Basko, M., Bedacht, S., Bläser, C., Blazevic, A., Busold, S., Deppert, O., Ding, J., Ehret, M., Fiala, P., Frydrych, S., O. Gericke, D., Hallo, L., Helfrich, J., Jahn, D., Kjartansson, E., and Roth, M. (2017). Experimental discrimination of ion stopping models near the Bragg peak in highly ionized matter. 8:15693.

[Cayzac et al., 2013] Cayzac, W., Frank, A., Schumacher, D., Roth, M., Blazevic, A., Wamers, F., Berdermann, M. T. E., Voss, B., and Heśling, T. (2013). A spectrometer on chemical vapour deposition-diamond basis for the measurement of the charge-state distribution of heavy ions in a laser-generated plasma. 84:043301.

[Ceramics and Crystals, 2016] Ceramics, S.-G. and Crystals (2016). *BC-422Q Ultra-fast timing plastic scintillator Data Sheet*.

[Cirrone et al., 2013] Cirrone, A. P. G., Carpinelli, M., Cuttone, G., Gammino, S., Jia, S. B., Korn, G., Maggiore, M., Manti, L., Margarone, D., Prokupek, J., Renis, M., Romano, F., Schillaci, F., Tomasello, B., Torrisi, L., Tramontana, A., and Velyhan, A. (2013). Elimed, future hadrontherapy applications of laser-accelerated beams. *Nuclear Instruments and Methods in Physics Research Section A: Accelerators, Spectrometers, Detectors and Associated Equipment*, 730:174 – 177. Proceedings of the 9th International Conference on Radiation Effects on Semiconductor Materials Detectors and Devices.

[Clark et al., 2000a] Clark, E. L., Krushelnick, K., Davies, J. R., Zepf, M., Tatarakis, M., Beg, F., Machacek, A., Norreys, P. A., Santala, M., Watts, I., and Dangor, A. E. (2000a). Measurements of energetic proton transport through magnetized plasma from intense laser interactions with solids. *Physical review letters*, 84:670–3.

[Clark et al., 2000b] Clark, E. L., Krushelnick, K., Davies, J. R., Zepf, M., Tatarakis, M., Beg, F. N., Machacek, A., Norreys, P. A., Santala, M. I. K., Watts, I., and Dangor, A. E. (2000b). Measurements of energetic proton transport through magnetized plasma from intense laser interactions with solids. *Phys. Rev. Lett.*, 84:670–673.

[Cookson, 1974] Cookson, J. (1974). Radiography with protons. *Naturwissenschaften*, 61:184–191.

[Cowan et al., 2004] Cowan, T. E., Fuchs, J., Ruhl, H., Kemp, A., Audebert, P., Roth, M., Stephens, R., Barton, I., Blazevic, A., Brambrink, E., Cobble, J., Fernández, J., Gauthier, J.-C., Geissel, M., Hegelich, M., Kaae, J., Karsch, S., Le Sage, G. P., Letzring, S., Manclossi, M., Meyroneinc, S., Newkirk, A., Pépin, H., and Renard-LeGalloudec, N. (2004). Ultralow emittance, multi-MeV proton beams from a laser virtual-cathode plasma accelerator. *Phys. Rev. Lett.*, 92:204801.

[Daido et al., 2012] Daido, H., Nishiuchi, M., and Pirozhkov, A. S. (2012). Review of laser-driven ion sources and their applications. *Reports on Progress in Physics*, 75(5):056401.

[DIN EN ISO 13694-2010, 2000] DIN EN ISO 13694-2010 (2000). Optics and optical instruments - lasers and laser-related equipment - test methods for laser beam power (energy) density distribution.

[Ding, 2018] Ding, J. (2018). *Generation, Handling and Transport of Laser-Driven Heavy Ion Beams*. PhD thesis, Technische Universität Darmstadt.

[Ecker et al., 2014] Ecker, B., Aurand, B., Hochhaus, D. C., Neumayer, P., Zielbauer, B., Cassou, K., Daboussi, S., Guilbaud, O., Kazamias, S., Le, T. T. T., E. Oliva Gonzalo, E., Li, L., Zhao, H., Jin, Q., Ros, D., Zeitoun, P., and Kuehl, T. (2014). X-ray laser developments at phelix. *Springer Proceedings in Physics*, 147:97–104.

[Ehret, 2016] Ehret, M. (2016). TNSA-proton beam guidance with strong magnetic fields generated by coil targets. Master's thesis, Technische Universität Darmstadt.

[Ehret, 2018] Ehret, M. (2018). ps laser driven transient discharges in coil targets with application to TNSA beam micro lensing. *poster*.

[Eisenbarth, 2017] Eisenbarth, U. (2017). *private conversation*.

[Endres, 2018] Endres, M. (2018). *Das Protonenmikroskop PRIOR und die Entwicklung eines Leichtgasbeschleunigers für Experimente an FAIR*. PhD thesis, Technische Universität Darmstadt.

[Esarey et al., 1995] Esarey, E., Sprangle, P., and Krall, J. (1995). Laser acceleration of electrons in vacuum. *Phys. Rev. E*, 52:5443–5453.

[Forck, 2015] Forck, P. (2015). *Lecture Notes on Beam Instrumentation and Diagnostics*. Joint university accelerator school.

[Foulon et al., 1996] Foulon, F., Bergonzo, P., Jany, C., Gicquel, A., and Pochet, T. (1996). CVD diamond detectors for radiation pulse characterization. *Nuclear Instruments and Methods in Physics Research A 380*.

[Franczak, 1987] Franczak, B. (1987). SIS18 Parameterliste.

[Frank, 2012] Frank, A. (2012). *Energy loss and charge tranfer of heavy ions in laser generated plasma*. PhD thesis, Technische Universität Darmstadt.

[Frank et al., 2013] Frank, A., Blazevic, A., Bagnoud, V., Basko, M., Börner, M., Cayzac, W., Kraus, D., Heßling, T., Hoffmann, D., Ortner, A., Otten, A., Pelka, A., D. Pepler, D. S., Tauschwitz, A., and Roth, M. (2013). Energy loss and charge transfer of argon in a laser-generated carbon plasma. 110.

[Fuchs et al., 2006] Fuchs, J., Antici, P., D'Humières, E., Lefebvre, E., Borghesi, M., Brambrink, E., Cecchetti, C. A., Kaluza, M., Malka, V., Manclossi, M., Meyroneinc, S., Mora, P., Schreiber, J., Toncian, T., Pépin, H., and Audebert, P. (2006). Laser-driven proton scaling laws and new paths towards energy increase. *Nature Physics*, 2.

[Gibbon, 2005] Gibbon, P. (2005). *Short Pulse Laser Interactions with Matter*. Imperial College Press.

[Gizzi et al., 2018] Gizzi, L., Baffigi, F., Brandi, F., Bussolino, G., Cristoforetti, G., Fazzi, A., Fulgentini, L., Giove, D., Koester, P., Labate, L., Maero, G., Palla, D., Romé, M., and Tomassini, P. (2018). Light Ion Accelerating Line (L3IA): Test experiment at ILIL-PW. *Nuclear Instruments and Methods in Physics Research Section A: Accelerators, Spectrometers, Detectors and Associated Equipment*.

[Günther et al., 2013] Günther, M. M., Britz, A., Clarke, R. J., Harres, K., Hoffmeister, G., Nürnberg, F., Otten, A., Pelka, A., Roth, M., and Vogt, K. (2013). Nais: Nuclear activation-based imaging spectroscopy. *Review of Scientific Instruments*, 84:073305.

[Haffa et al., 2018] Haffa, D., Yang, R., Bin, J., Lehrack, S., Brack, F.-E., Ding, I., Englbrecht, F., Gao, Y., Gebhard, J., Gilljohann, M., Götzfried, J., Hartmann, J., Herr, S., Hilz, P., D. Kraft, S., Kreuzer, C., Kroll, F., Lindner, F., Metzkes, J., and Schreiber, J. (2018). I-BEAT: New ultrasonic method for single bunch measurement of ion energy distribution.

[Hamamatsu, 2018a] Hamamatsu (Accessed: 8th November 2018a). *Guide to streak cameras*.

[Hamamatsu, 2018b] Hamamatsu (Accessed: 8th November 2018b). *Universal Streak Camera C10910 Series, Manual*.

[Hargrove et al., 1964] Hargrove, L. E., Fork, R., and A. Pollack, M. (1964). Locking of He-Ne laser modes induced by synchronous intracavity modulation. *Applied Physics Letters*, 5:4 – 5.

[Hatchett et al., 2000] Hatchett, S., Brown, C. G., Cowan, T., Henry, E. A., Johnson, J. S., Key, M. H., Koch, J., Langdon, B. A., Lasinski, B. F., W. Lee, R., Mackinnon, A., Pennington, D., Perry, M., Phillips, T., Roth, M., Sangster, T., Singh, M. S., Snavely, R. A., Stoyer, M., and Yasuike, K. (2000). Electron, photon, and ion beams from the relativistic interaction of petawatt laser pulses with solid targets. *Physics of Plasmas*, 7:2076–2082.

[HEDgeHOB collaboration, 2005] HEDgeHOB collaboration (2005). Studies on high energy density matter with intense heavy ion and laser beams at FAIR. *Technical proposal for design, construction, commissioning and operation for FAIR*.

[Hegelich et al., 2006] Hegelich, B., Albright, B., Cobble, J., Flippo, K., Letzring, S., Paffett, M., Ruhl, H., Schreiber, J., K. Schulze, R., and Fernandez, J. (2006). Laser acceleration of quasi-monoenergetic mev ion beams. 439:441–4.

[Hessling, 2010] Hessling, T. (2010). *Charakterisierung lasererzeugter Hohlraumstrahlung für die experimentelle Untersuchung der Wechselwirkung von Schwerionen mit Plasmen*. PhD thesis, Technische Universität Darmstadt.

[Hidding et al., 2011] Hidding, B., Königstein, T., Oswald, W., Rosenzweig, J. B., Nakajima, K., and Pretzler, G. (2011). Laser–plasma-accelerators: A novel, versatile tool for space radiation studies. *Nuclear Instruments and Methods in Physics Research Section A: Accelerators, Spectrometers, Detectors and Associated Equipment*, 636(1):31 – 40.

[Highland, 1975] Highland, V. L. (1975). Some practical remarks on multiple scattering. *Nuclear Instruments and Methods*, 129(2):497 – 499.

[Hillert, 2015] Hillert, W. (2015). *Lecture notes on transverse linear beam dynamics*. CAS The CERN Accelerator School.

[Hinterberger, 2008] Hinterberger, F. (2008). *Physik der Teilchenbeschleuniger und Ionenoptik*. Springer Verlag.

[Hoffmeister, 2014] Hoffmeister, G. (2014). *Influencing laser-accelerated ions by femtosecond-laser desorption*. PhD thesis, Technische Universität Darmstadt.

[Hofmann et al., 2011] Hofmann, I., Meyer-ter Vehn, J., Yan, X., Orzhekhovskaya, A., and Yaramyshev, S. (2011). Collection and focusing of laser accelerated ion beams for therapy applications. *Phys. Rev. ST Accel. Beams*, 14:031304.

[Holzer, 2016] Holzer, B. (2016). *Lecture notes on introduction to transverse beam dynamics*. CAS The CERN Accelerator School.

[Humphries, 1990] Humphries, S. (1990). *Charged particle beams*. John Wiley and Sons.

[Häuser, 1989] Häuser, J. (1989). *Eigenschaften von Spiralresonatoren*. PhD thesis, Johann Wolfgang von Goethe-Universität Frankfurt.

[I. K. Santala et al., 2000] I. K. Santala, M., Zepf, M., Watts, I., Beg, F., Clark, E., Tatarakis, M., Krushelnick, K., Dangor, A., Mccanny, T., Spencer, I., Singhal, R., Ledingham, K., C. Wilks, S., Machacek, A., S. Wark, J., Allott, R., J. Clarke, R., and Norreys, P. (2000). Effect of the plasma density scale length on the direction of fast electrons in relativistic laser-solid interactions. *Physical Review Letters*, 84.

[Instruments, 2012] Instruments, N. (2012). Part II – Photovoltaic Cell I-V characterization theory and LabVIEW analysis code. *Whitepapers*.

[J. McClung and Hellwarth, 1962] J. McClung, F. and Hellwarth, R. (1962). Giant optical pulsations from ruby. *Applied Optics*, 1.

[Jahn, 2015] Jahn, D. (2015). Development of fast diamond detectors for temporal profile measurements of short, intense ion bunches. Master's thesis, Technische Universität Darmstadt.

[Kar et al., 2015] Kar, S., Green, A., Ahmed, H., Alejo, A., Robinson, A., Cerchez, M., Clarke, R., Doria, D., Dorkings, S., Fernandez, J., Mirfayzi, S., Mckenna, P., Naughton, K., Neely, D., Norreys, P., Peth, C., Powell, H., Ruiz, J. A., Swain, J., and Borghesi, M. (2015). Beamed neutron emission driven by laser accelerated light ions. *New Journal of Physics*.

[Keppler et al., 2016] Keppler, S., Sävert, A., Körner, J., Hornung, M., Liebetrau, H., Hein, J., and Kaluza, M. C. (2016). The generation of amplified spontaneous emission in high-power CPA laser systems. *Laser & Photonics Reviews*, 10(2):264–277.

[Kiefer, 2014] Kiefer, T. (2014). *Investigation of the laser-based Target Normal Sheath Acceleration (TNSA) process for high-energy ions — an analytical and numerical study*. PhD thesis, Friedrich-Schiller-Universität Jena.

[Kleinschmidt et al., 2018] Kleinschmidt, A., Bagnoud, V., Deppert, O., A. Favalli, S. F., Hornung, J., Jahn, D., Schaumann, G., Tebartz, A., Wagner, F., Wurden, G., and B. Zielbauer, M. R. (2018). Intense, directed neutron beams from a laser-driven neutron source at phelix. *Physics of Plasmas*, 25:053101.

[Koenig et al., 2005] Koenig, M., Benuzzi-Mounaix, A., Ravasio, A., Vinci, T., Ozaki, N., Lepape, S., Batani, D., Huser, G., Hall, T., Hicks, D., MacKinnon, A., Patel, P., Park, H. S., Boehly, T., Borghesi, M., Kar, S., and Romagnani, L. (2005). Progress in the study of warm dense matter. *Plasma Physics and Controlled Fusion*, 47(12B):B441.

[Kraft et al., 2010] Kraft, S., Richter, C., Zeil, K., Baumann, M., Beyreuther, E., Bock, S., Bussmann, M., Cowan, T., Dammene, Y., Enghardt, W., Helbig, U., Karsch, L., Kluge, T., Laschinsky, L., Lessmann, E., Metzkes, J., Naumburger, D., Sauerbrey, R., Schürer, M., and Pawelke, J. (2010). Dose-dependent biological damage of tumour cells by laser-accelerated proton beams: Focus on laser- and beam-driven plasma accelerators. *New Journal of Physics*, 12:85003.

[Kraus et al., 2018] Kraus, D., Hartley, N., Frydrych, S., Schuster, A. K., Rohatsch, K., Rödel, M., Cowan, T., Brown, S., Cunningham, E., Driel, T. V., Fletcher, L., Galtier, E., Gamboa, E. J.,

Garcia, A. L., Gericke, D. O., Granados, E., Heimann, P. A., Lee, H. J., MacDonald, M., and Vorberger, J. (2018). High-pressure chemistry of hydrocarbons relevant to planetary interiors and inertial confinement fusion. *Physics of Plasmas*, 25.

[Kroll, 2018] Kroll, F. (2018). *The study and development of pulsed high-field magnets for application in laser-plasma physics*. PhD thesis, Technische Universität Dresden.

[Kruer, 1988] Kruer, W. L. (1988). The physics of plasma interactions. *Addison Wesley*.

[Kumar, 2009] Kumar, V. (2009). Understanding the focusing of charged particle beams in a solenoid magnetic field. 77:737.

[Lang, 2014] Lang, P. (2014). *Aufbau und Test des Protonenmikroskops PRIOR*. PhD thesis, Technische Universität Darmstadt.

[Leonhardt, 2019] Leonhardt, R. (2019). Emittanzmessung an der LIGHT-Strahlführung. Master's thesis, Technische Universität Darmstadt.

[Liouville, 1838] Liouville, J. (1838). Note on the theory of the variation of arbitrary constants. *Journal de math*, 3:349.

[Lynch and Dahl, 1991] Lynch, G. R. and Dahl, O. I. (1991). Approximations to multiple Coulomb scattering. *Nuclear Instruments and Methods in Physics Research Section B: Beam Interactions with Materials and Atoms*, 58(1):6 – 10.

[Macchi, 2013] Macchi, A. (2013). *A Superintense Laser-Plasma Interaction Theory Primer*. SpringerBriefs in Physics.

[Mackinnon et al., 2004] Mackinnon, A., Patel, P. K., Town, R. P., Edwards, M. J., Phillips, T., Lerner, S. C., Price, D. W., Hicks, D., Key, M. H., Hatchett, S., Wilks, S. C., Borghesi, M., Romagnani, L., Kar, S., Toncian, T., Pretzler, G., Willi, O., Koenig, M., Martinolli, E., and Boehly, T. (2004). Proton radiography as an electromagnetic field and density perturbation diagnostic (invited). *Review of Scientific Instruments*, 75.

[Mackinnon et al., 2006] Mackinnon, A. J., K.Patel, P., Borghesi, M., Clarke, R. C., Freeman, R. R., Habara, H., Hatchett, S. P., Hey, D., Hicks, D. G., Kar, S., Key, M. H., King, J. A., Lancaster, K., Neely, D., Nikkro, A., Norreys, P. A., Notley, M. M., Phillips, T. W., Romagnani, L., Snavely, R. A., Stephens, R. B., and Town, R. P. J. (2006). Proton radiography of a laser-driven implosion. *Phys. Rev. Lett.*, 97:045001.

[Maiman, 1960] Maiman, T. H. (1960). Stimulated optical radiation in ruby masers. *Nature*, 187:493–494.

[Maksimchuk et al., 2000] Maksimchuk, A., Gu, S., Flippo, K., Umstadter, D., and Bychenkov, V. (2000). Forward ion acceleration in thin films driven by a high-intensity laser. 84:4108.

[Masood et al., 2017] Masood, U., Cowan, T., Enghardt, W., M. Hofmann, K., Karsch, L., Kroll, F., Schramm, U., J. Wilkens, J., and Pawelke, J. (2017). A light-weight compact proton gantry design with a novel dose delivery system for broad-energetic laser-accelerated beams. 62:5531–5555.

[McLaughlin et al., 1996] McLaughlin, W. L., Al-Sheikhly, M., Lewis, D. F., Kovács, A., and Wojnárovits, L. (1996). Radiochromic solid-state polymerization reaction. *Irradiation of Polymers*, pages 152–166.

[Mourou et al., 2011] Mourou, G. A., Korn, G., Sandner, W., and Collier, J. L. (2011). *ELI Extreme Light Infrastructure: Whitebook*. ELI.

[Mulser and Bauer, 2010] Mulser, P. and Bauer, D. (2010). *High Power Laser-Matter Interaction*. Springer Verlag.

[Mulser et al., 2012] Mulser, P., Weng, S. M., and Liseykina, T. (2012). Analysis of the Brunel model and resulting hot electron spectra. *Phys. Plasmas 19, 043301*.

[Nemoto et al., 2012] Nemoto, K., Maksimchuk, A., Banerjee, S., Flippo, K., Mourou, G., Umstadter, D., and Bychenkov, Y. (2012). Laser-triggered ion acceleration and table top isotope production. *Appl. Phys. Lett.*, 78:595–597.

[Niroomand-Rad et al., 1998] Niroomand-Rad, A., Blackwell, C. R., Coursey, B. M., Gall, K. P., Galvin, J. M., McLaughlin, W. L., Meigooni, A. S., Nath, R., Rodgers, J. E., and Soares, C. G. (1998). Radiochromic film dosimetry: Recommendations of aapm radiation therapy committee task group 55. *Medical Physics*, 11:2093–2115.

[Nishiuchi et al., 2019] Nishiuchi, M., Daito, I., Ikegami, M., Daido, H., Mori, M., Orimo, S., Ogura, K., Sagisaka, A., Yogo, A., Pirozhkov, A. S., Sugiyama, H., Kiriyama, H., Okada, H., Kanazawa, S., Kondo, S., Shimomura, T., Tanoue, M., Nakai, Y., Sasao, H., Wakai, D., Sakaki, H., Bolton, P., Choi, I. W., Sung, J. H., Lee, J., Oishi, Y., Fujii, T., Nemoto, K., Souda, H., Noda, A., Iseki, Y., and Yoshiyuki, T. (2019). Focusing and spectral enhancement of a repetition-rated, laser-driven, divergent multi-mev proton beam using permanent quadrupole magnets.

[Nürnberg, 2010] Nürnberg, F. (2010). *Laser-accelerated proton beams as a new particle source*. PhD thesis, Technische Universität Darmstadt.

[Nürnberg et al., 2009] Nürnberg, F., Schollmeier, M., Brambrink, E., Blazevic, A., Carroll, D. C., Flippo, K., Gautier, D. C., Geissel, M., Harres, K., Hegelich, B. M., Lundh, O., Markey, K., McKenna, P., Neely, D., Schreiber, J., and Roth, M. (2009). Radiochromic film imaging spectroscopy of laser-accelerated proton beams. *Review of Scientific Instruments*, 80(3):033301.

[Ortner et al., 2015] Ortner, A., Frank, A., Blazevic, A., and Roth, M. (2015). Role of charge transfer in heavy-ion-beam-plasma interactions at intermediate energies. 91:023104.

[Patel et al., 2003] Patel, P. K., Mackinnon, A. J., Key, M. H., Cowan, T. E., Foord, M. E., Allen, M., Price, D. F., Ruhl, H., Springer, P. T., and Stephens, R. (2003). Isochoric heating of solid-density matter with an ultrafast proton beam. *Phys. Rev. Lett.*, 91:125004.

[Pelka et al., 2010] Pelka, A., Gregori, G., Gericke, D. O., Vorberger, J., Glenzer, S. H., Günther, M. M., Harres, K., Heathcote, R., Kritcher, A. L., Kugland, N. L., Li, B., Makita, M., Mithen, J., Neely, D., Niemann, C., Otten, A., Riley, D., Schaumann, G., Schollmeier, M., Tauschwitz, A., and Roth, M. (2010). Ultrafast melting of carbon induced by intense proton beams. *Phys. Rev. Lett.*, 105:265701.

[Pomorski, 2008] Pomorski, M. (2008). *Electronic properties of single crystal cvd diamond and its suitability for particle detection in hadron physics experiments*. PhD thesis, Johann-Wolfgang-Goethe Universität Frankfurt.

[Prall et al., 2016] Prall, M., Durante, M., Berger, T., Przybyla, B., Graeff, C., Lang, P. M., Latessa, C., Shestov, L., Simoniello, P., Danly, C., Mariam, F., Merrill, F., Nedrow, P., Wilde, C., and Varentsov, D. (2016). High-energy proton imaging for biomedical applications. *Scientific Reports*, 6.

[Reiser, 2008] Reiser, M. (2008). *Theory and Design of Charged Particle Beams*, volume 48.

[Rogers corporation, 2017] Rogers corporation (2017). *RO4000 Laminates - Data Sheet*.

[Roth, 2009] Roth, M. (2009). Review on the current status and prospects of fast ignition in fusion targets driven by intense, laser generated proton beams. *Plasma Physics and Controlled Fusion*, 51(1):014004.

[Roth et al., 2005] Roth, M., Blazevic, A., Brambrink, E., Geissel, M., Cowan, T., Fuchs, J., Kemp, A., Ruhl, H., Audebert, P., Cobble, J., Fernandez, J., Hegelich, M., Letzring, S., Ledingham, K., McKenna, P., Clarke, R., Neely, D., Karsch, S., Habs, D., and Schreiber, J. (2005). Laser accelerated, high quality ion beams. *Hyperfine Interactions*, 162:45–53. 10.1007/s10751-005-9202-4.

[Roth et al., 2002] Roth, M., Blazevic, A., Geissel, M., Schlegel, T., Cowan, T. E., Allen, M., Gauthier, J.-C., Fuchs, P. A. J., ter Vehn, J. M., Hegelich, M., Karsch, S., and Pukhov, A. (2002). Energetic ions generated by laser pulses: A detailed study on target properties. *Phys. Rev. ST Accel. Beams*, 5:061301.

[Roth et al., 2016] Roth, M., Jung, D., Falk, K., Guler, N., Deppert, O., Devlin, M., Favalli, A., Fernandez, J., Gautier, D., Geissel, M., Haight, R., Hamilton, C., Hegelich, B., Johnson, R., Kleinschmidt, A., Merrill, F., Schaumann, G., Schoenberg, K., Schollmeier, M., and Wurden, G. (2016). A bright neutron source driven by relativistic transparency of solids. *Journal of Physics: Conference Series*, 688:012094.

[Roth and Schollmeier, 2016] Roth, M. and Schollmeier, M. (2016). Ion acceleration—target normal sheath acceleration.

[Sakaki et al., 2019] Sakaki, H., Hori, T., Nishiuchi, M., Bolton, P., Daido, H., Kawanishi, S., and Sutherland, K. (2019). Designing integrated laser-driven ion accelerator systems for hadron therapy at PMRC (photo medical research center).

[Santos et al., 2018] Santos, J. J., Bailly-Grandvaux, M., Ehret, M., Arefiev, A. V., Batani, D., Beg, F. N., Calisti, A., Ferri, S., Florido, R., Forestier-Colleoni, P., Fujioka, S., Gigosos, M. A., Giuffrida, L., Gremillet, L., Honrubia, J. J., Kojima, S., Korneev, P., Law, K. F. F., Marques, J.-R., Morace, A., Mosse, C., Peyrusse, O., Rose, S., Roth, M., Sakata, S., Schaumann, G., Suzuki-Vidal, F., Tikhonchuk, V. T., Toncian, T., Woolsey, N., and Zhang, Z. (2018). Laser-driven strong magnetostatic fields with applications to charged beam transport and magnetized high energy-density physics. *Physics of Plasmas*, 25:056705.

[Schollmeier, 2008] Schollmeier, M. (2008). *Optimization and control of laser-accelerated proton beams*. PhD thesis, Technische Universität Darmstadt.

[Schreiber, 2012] Schreiber, A. (2012). RGB-Farb-Kalibrierung von radiochromatischen Filmen. Bachelor's thesis, Technische Universität Darmstadt.

[Schumacher, 2011] Schumacher, D. (2011). *Untersuchung laserinduzierter Hohlraumstrahlung für den Energieverlust von Schwerionen in indirekt geheizten Kohlenstoffplasmen*. PhD thesis, Technische Universität Darmstadt.

[Semmler, 2018] Semmler, I. (2018). Untersuchung der Transporteigenschaften von Quadrupolen und deren Anwendung auf lasererzeugte Ionenstrahlen. Master's thesis, Technische Universität Darmstadt.

[Seryi, 2015] Seryi, A. (2015). *Unifying Physics of Accelerators, Lasers and Plasma*.

[Singh, 2014] Singh, R. (2014). *Tune measurement at GSI SIS-18: methods and applications*. PhD thesis, Technische Universität Darmstadt.

[Snavely et al., 2000] Snavely, R. A., Key, M. H., Hatchett, S. P., Cowan, T. E., Roth, M., Phillips, T. W., Stoyer, M. A., Henry, E. A., Sangster, T. C., Singh, M. S., Wilks, S. C., MacKinnon, A., Offenberger, A., Pennington, D. M., Yasuike, K., Langdon, A. B., Lasinski, B. F., Johnson, J., Perry, M. D., and Campbell, E. M. (2000). Intense high-energy proton beams from petawatt-laser irradiation of solids. *Phys. Rev. Lett.*, 85(14):2945–2948.

[Strehl, 2006] Strehl, P. (2006). *Beam Instrumentation and Diagnostics*. Springer Verlag.

[Strickland and Mourou, 1985] Strickland, D. and Mourou, G. (1985). Compression of amplified chirped optical pulses. *Optics Communications*, 55:219–221.

[Tomut and Simon, 2018] Tomut, M. and Simon, P. (2018). *private conversation*.

[Uriot and Pichoff, 2011] Uriot, D. and Pichoff, N. (2011). Tracewin documentation.

[Varentsov et al., 2015] Varentsov, D., Antonov, O., Bakhmutova, A., Barnes, C., Bogdanov, A., Danly, C. R., Efimov, S., Endres, M., Fertman, A., Golubev, A., Hoffmann, D., Ionita, B., Kantsyrev, A., Krasik, Y., Lang, P. M., Lomonosov, I., Mariam, F., Markov, N., Merrill, F., and Zubareva, A. (2015). Commissioning of the prior proton microscope. *Review of Scientific Instruments*, 87.

[Vay et al., 2012] Vay, J.-L., Grote, D., Cohen, R. H., and Friedman, A. (2012). Novel methods in the particle-in-cell accelerator code-framework warp. *Computational Science and Discovery*, 5:014019.

[Wagner et al., 2016] Wagner, F., Deppert, O., Brabetz, C., Fiala, P., Kleinschmidt, A., Poth, P., Schanz, V., Tebartz, A., Zielbauer, B., Roth, M., Stöhlker, T., and Bagnoud, V. (2016). Maximum proton energy above 85 MeV from the relativistic interaction of laser pulses with micrometer thick CH 2 targets. 116.

[Weih, 2016] Weih, S. (2016). Emittance measurements of laser-driven protons at the light project. Master's thesis, Technische Universität Darmstadt.

[Wharton et al., 1998] Wharton, K., Hatchett, S., Wilks, S. C., Key, M. H., Moody, J., Yanovsky, V., Offenberger, A., Hammel, B., Perry, M., and Joshi, C. (1998). Experimental measurements of hot electrons generated by ultraintense (>1019 w/cm2) laser-plasma interactions on solid-density targets. *Physical Review Letters - PHYS REV LETT*, 81:822–825.

[Wille, 1996] Wille, K. (1996). *Physik der Teilchenbeschleuniger und Synchrotronstrahlungsquellen*. Teubner Studienbücher.

[Zeil et al., 2013] Zeil, K., Baumann, M., Beyreuther, E., Burris-Mog, T., Cowan, T. E., Enghardt, W., Karsch, L., Kraft, S. D., Laschinsky, L., Metzkes, J., Naumburger, D., Oppelt, M., Richter, C., Sauerbrey, R., Schürer, M., Schramm, U., and Pawelke, J. (2013). Dose-controlled irradiation of cancer cells with laser-accelerated proton pulses. *Applied Physics B*, 110(4):437–444.

[Ziegler, 2013] Ziegler, J. F. (2013). The stopping and range of ions in matter (SRIM), http://www.srim.org.

[Zobus, 2016] Zobus, Y. (2016). Umbau des Hochenergielasersystems nhelix mit anschließender Strahlcharakterisierung. Bachelor's thesis, Technische Universität Darmstadt.

List of figures

List of tables

9 Acknowledgements

Every PhD thesis requires extraordinary costs to be finished. Besides the increased time requirements, several sweets and diamonds had to die to satisfy the participating persons and achieve the scientific results. The detailed statement of costs is listed in table 9.1. Finally, I want to thank all persons, who contributed to this work.

Table 9.1: Statement of costs for this PhD thesis

designation	**amount**
consumed *Milchschnitte* during experiments	480
consumed *Twixx* during experiments	196
destroyed diamonds (directly or indirectly)	6
flat bicycle tires	4
number of chocolate raisins during writing	11.907 ± 630
RCF scanning time	(8 ± 1) weeks
estimated cleanup efforts at Z6	(42 ± 8) hours
waiting for the next experimental campaign	562 days

First, I want to thank my supervisor Prof. Dr. Markus Roth, who gave me the possibility to write this diversified PhD thesis and who included me in his research group. He supported my research and the LIGHT project with interesting ideas. Moreover, he opened me the oppertunity to see interesting facilities like the National Ignition Facility.
Also I want to thank my second supervisor, Prof. Dr. Boine-Frankenheim, for his theoretical support and helpful advice. I appreciate your interest and suggestions in the discussions about the injection.

Many thanks belong the LIGHT experimental team and their patience during the beamline alignment. Especially, I want to thank Christian Brabetz, Simon Busold and Dennis Schumacher for their support and sharing their great experience. I appreciate the work of my master students, Simon Weih and René Leonhardt. The experiments would not be that successful and funny without Florian Kroll and Florian-Emmanuel Brack from Helmholtzzentrum Dresden-Rossendorf, who brought their truck, transporting the solenoids and a pulse generator, with them.

I have to give credit to the GSI detector lab. Michael Trägers dedication and great knowledge about diamond detectors enabled the successful temporal measurements and further development of our prototype. I want to thank to Mladen Kis for the critical discussions and Michal Pomorski for etching the most stable existing diamond membrane.
From the IKP target lab, I am thankful for the help from Gabriel Schaumann and Torsten Abel, who supported me in the production of the easy metal foil targets. I thank Michael Ehret for his contribution to the LIGHT project with his micro Helmholtz cavity targets.

I am thankful to the commitment and fruitful discussions of the growing LIGHT collaboration pushing this research project forward.

All experiments of this work would not be possible without the well-working PHELIX laser. The PHELIX team Stefan Götte, Bernhard Zielbauer, Udo Eisenbarth, Christian Brabetz, Dirk Reemts, Sabine Kunzer, Vincent Bagnoud and Diana Lang were very supportive by the realization of the experimental campaigns. Furthermore, the HF department at GSI provided the necessary rf infrastructure and knowledge. The GSI mechanics supported this work and the beamline with their manufactoring skills and helped me to steal my new bike back, after the key of my bike lock broke. Especially, I want to thank Davide Racano for telling me to care about my bike, while driving to GSI.

Special thanks belong to my proofreaders Annika Kleinschmidt, Simone Aumüller, Martin Metternich and Abel Blazevic. Especially, I will not forget the (new or re-)structuring comments (I admit it that they improved this thesis a lot).
Furthermore, I am grateful for the friendly atmosphere and discussions within the laser- and plasma group. I appreciated the baking-waffles afternoons and enjoyed the discussions with my office colleagues Annika Kleinschmidt and Victor Schanz. I am thankful for the suggestions in the long discussions in my first year with Oliver Deppert, Gabi Hoffmeister and Jan Helfrich.

I would have never started my studies in physics, if my school teacher Robert Schnabel would not encourage me to solve these kind of problems. I thank him for sharing his enthusiasm.
I am also thankful to have met my university friends Lukas Mader, Moritz Reichert, Christopher Jung, Andreas Herdt, Max Schmitt, Nils Haase, Michael Mathy, Martin Schanz and many others, who motivated me to solve the homeworks, learned with me for exams and shared with me other experiences like baking cinnamon rolls past midnight or go-carting.

Many thanks belong to my team mates from swimming and scuba diving. I enjoyed the sportive activities and trips with them. They provided me the sportive balance to my scientific work.

Finally, this thesis would not be possible without the support from my family, Max and my friends. They encouraged and supported me during this thesis. Especially, they made me laugh, when things were not going well and I had to wait for the never-taking-place beamtime.

10 Publications and conference contributions

In the frame of this work, several publications and contributions to conferences were made. A list of published articles, given talks and awards is shown below.

First author publications (reviewed):

- **D. Jahn**, D. Schumacher, C. Brabetz, F. Kroll, F.-E. Brack, J. Ding, R. Leonhardt, I. Semmler, A. Blazevic, U. Schramm, M. Roth: Focusing of multi-MeV, subnanosecond proton bunches from a laser-driven source, Phys. Rev. Accel. Beams 22, 011301 (2019)
- **D. Jahn**, M. Träger, M. Kis, M. Ciobanu, M. Pomorski, C. Brabetz, D. Schumacher, U. Bonnes, S. Busold, A. Blazevic und M. Roth: Chemical-vapor deposited ultra-fast diamond detectors for temporal measurements of ion bunches, Rev. Sci. Instrum. 89, 093304 (2018)
- **D. Jahn**, D. Schumacher, C. Brabetz, J. Ding, S. Weih, F. Kroll, F.-E. Brack, U. Schramm, A. Blazevic, and M. Roth: First application studies at the laser-driven LIGHT beamline: Improving proton beam homogeneity and imaging of a solid target, Nucl. Instrum. Methods Phys. Res. A 909, 173-176 (2018)

First author publications (non-reviewed):

- **D. Jahn**, D. Schumacher, C. Brabetz, J. Ding, S. Weih, F. Kroll, F.-E. Brack, U. Schramm, T. E. Cowan, V. Bagnoud, A. Blazevic, and M. Roth: Improvement of the homogeneity of the laser-driven proton beam within the LIGHT project, GSI scientific report 2016, GSI Darmstadt (2017)
- **D. Jahn**, D. Schumacher, C. Brabetz, J. Ding, S. Weih, F. Kroll, U. Schramm, T. E. Cowan, V. Bagnoud, A. Blazevic, and M. Roth: Generation of subnanosecond, intense ion bunches with the laser-driven LIGHT beamline, GSI scientific report 2015, GSI Darmstadt (2016)
- **D. Jahn**, S. Busold, D. Schumacher, C. Brabetz, M. Träger, M. Kis, M. Ciobanu, A. Blazevic, and M. Roth: Development of a CVD diamond detector for temporal profile measurements of intense sub-nanosecond ion bunches, GSI scientific report 2014, GSI Darmstadt (2015)

Co-author publications (reviewed):

- A. Kleinschmidt, V. Bagnoud, O. Deppert, A. Favalli, S. Frydrych, J. Hornung, **D. Jahn**, G. Schaumann, A. Tebartz, F. Wagner, G. Wurden, B. Zielbauer, and M. Roth: Intense, directed neutron beams from a laser-driven neutron source at PHELIX, Physics of Plasmas 25, 053101 (2018)

- J. Ding, D. Schumacher, **D. Jahn**, A. Blazevic, M. Roth: Simulation studies on generation, handling and transport of laser-accelerated carbon ions, Nucl. Instrum. Methods Phys. Res. A 909, 168-172 (2018)
- W. Cayzac, A. Frank, A. Ortner, V. Bagnoud, M. M. Basko, S. Bedacht, C. Bläser, A. Blazevic, S. Busold, O. Deppert, J. Ding, M. Ehret, P. Fiala, S. Frydrych, D. O. Gericke, L. Hallo, J. Helfrich, **D. Jahn**, E. Kjartansson, A. Knetsch, D. Kraus, G. Malka, N. Naumann, K. Pepitone, D. Pepler, S. Sander, G. Schaumann, T. Schlegel, N. Schroeter, D. Schumacher, M. Seibert, An. Tauschwitz, J. Vorberger, F. Wagner, S. Weih, Y. Zobus, and M. Roth: Experimental discrimination of ion stopping models near the Bragg peak in highly ionized matter, Nature Communications 8, 15693 (2017)
- S. Busold, D. Schumacher, C. Brabetz, **D. Jahn**, F. Kroll, O. Deppert, U. Schramm, T. Cowan, A. Blazevic, V. Bagnoud, and M. Roth: Towards highest peak intensities for ultra-short MeV-range ion bunches, Scientific Reports 5, 1 (2015)
- C. Brabetz, S. Busold, T. Cowan, O. Deppert, **D. Jahn**, O. Kester, M. Roth, D. Schumacher, and V. Bagnoud: Laser-driven ion acceleration with hollow laser beams, Physics of Plasmas 22, 013105 (2015)

Conference contributions (oral):

- 39th International Workshop on High Energy Density Physics with Intense Ion and Laser Beams, 27 January - 02 February 2019, Hirschegg, Austria
- 8th Conference of the International Committee on Ultrahigh Intensity Lasers (ICUIL), 9-14 September 2018, Lindau, Germany
- Advanced Accelerator Concepts (AAC), 12-17 August 2018, Breckenridge, USA
- LIGHT Collaboration Meeting 2018 at GSI, 19-20 April 2018, Darmstadt, Germany
- DPG Frühjahrstagung 2018, 19-23 March 2018, Würzburg, Germany
- 38th International Workshop on High Energy Density Physics with Intense Ion and Laser Beams, 28 January - 02 February 2018, Hirschegg, Austria
- European Advanced Accelerator Concepts (EAAC), 24-30 September 2017, Elba, Italy
- DPG Frühjahrstagung 2017, 19-21 March 2017, Dresden, Germany
- LIGHT Collaboration Meeting 2016 at GSI, 26-27 September 2016, Darmstadt, Germany
- XLAB Alumni Symposium 2016, 19-21 August 2016, Göttingen, Germany
- DPG Frühjahrstagung 2016, 14-18 March 2016, Darmstadt, Germany
- 36th International Workshop on High Energy Density Physics with Intense Ion and Laser Beams, 31 January - 5 February 2016, Hirschegg, Austria

Awards and grants:

- Best poster award, *8th Conference of the International Committee on Ultrahigh Intensity Lasers (ICUIL)*, Lindau, Germany, 2018
- DAAD grant for the participation on the workshop of *Advanced Accelerator Concepts 2018* (AAC 2018)
- Poster award, *38th International Workshop on High Energy Density Physics with Intense Ion and Laser Beams 2018*, Hirschegg, Austria
- Student grant for the participation on the workshop *European Advanced Accelerator Concepts* (EAAC 2017)
- Poster award, *35th International Workshop on High Energy Density Physics with Intense Ion and Laser Beams 2015*, Hirschegg, Austria

11 Curriculum vitae

Personal

Name	Diana Jahn
Date of birth	21 September 1990
Place of birth	Hanau am Main
Nationality	German

Education

since 04/2016	PhD at Technische Universität Darmstadt title: *Achieving highest proton intensities with a laser-based ion beamline*
01/2014-12/2015	Master of Science (Physics) at Technische Universität Darmstadt title: *Development of fast diamond detectors for temporal profile measurements of short, intense ion bunches*
09/2012-04/2013	exchange year at University of Saskatchewan title of research project: *neutron activation analysis of Cold Lake water*
10/2010-12/2013	Bachelor of Science (Physics) at Technische Universität Darmstadt title: *Investigations of spectral analysis of hot electrons during laser particle acceleration*
07/2010	Abitur at Karl-Rehbein-Schule in Hanau

Work

since 04/2016	supervision of Master students
10/2013-07/2018	student assistant for lecture accompanying tutorials in physics and supervision during the basic internship in physics at Technische Universität Darmstadt
09/2013-12/2015	student trainee for vacuum simulations for APPA at FAIR at GSI Helmholtzzentrum für Schwerionenforschung

Erklärung gemäß §9 Promotionsordnung

Hiermit versichere ich, dass ich die vorliegende Dissertation selbstständig angefertigt und keine anderen als die angegebenen Quellen und Hilfsmittel verwendet habe. Alle wörtlichen und paraphrasierten Zitate wurden angemessen kenntlich gemacht. Die Arbeit hat bisher noch nicht zu Prüfungszwecken gedient.

Darmstadt, den 31. März 2019

_____

(Diana Jahn)